UNIVERSITY OF SOUTHAMPTON

# Effects of Particle Properties and Boundary Conditions on Soil Shear Behaviour: 3-D Numerical Simulations

Qinglai Ni

A dissertation submitted for the

degree of Doctor of Philosophy

Faculty of Engineering and Applied Science

June 2003

UNIVERSITY OF SOUTHAMPTON

ABSTRACT

FACULTY OF ENGINEERING AND APPLIED SCIENCE

DEPARTMENT OF CIVIL & ENVIRONMENTAL ENGINEERING

Doctor of Philosophy

# EFFECTS OF PARTICLE PROPERTIES AND BOUNDARY CONDITIONS ON SOIL SHEAR BEHAVIOUR: 3-D NUMERICAL SIMULATIONS

by Qinglai Ni

The mechanical response of cohesionless granular materials under general engineering stress conditions is examined by simulation of direct shear box and biaxial tests using a three dimensional distinct element method computer code PFC-3D.

When shearing a random assembly of single sized spheres, the effective angle of shearing resistance at constant volume $\phi'_{cv}$ does not increase with interparticle friction angle $\phi_\mu$. The strength and volumetric dilation of such an assembly are low. The strength of an assemblage increases when different sized spheres are used or when their rotations are restrained. For non-spherical particles, an increase in $\phi_\mu$ results in an noticeable increase in $\phi'_{peak}$, $\phi'_{cv}$ and volumetric dilation. The less spherical the particles, the higher the strength and the dilation rate of the assembly, probably as a result of particle interlocking. Loading conditions such as the initial porosity, confining stress and friction on the loading platen, also significantly affect a sample's stress–dilation behaviour.

Shear bands can be characterised by a defined zone of intensively rotated particles, associated with large voids and concentrated shear strain. The width of a shear band is related to particle size and shape and the direction of a shear band is related to the applied boundary conditions. Samples with low initial porosity and smooth loading platens or comprising spherical particles are less likely to develop shear bands.

The present study suggests that, under specific conditions and to a certain extent, a DEM model consisting of tens of thousands particles can be a feasible approach to investigate both the macro and micro behaviour of granular material. However, to study the micro behaviour in greater detail or to simulate a more realistic and sophisticated test, further research will be needed.

ACKNOWLEDGEMENTS

I am extremely grateful to my supervisor, Professor William Powrie, for his guidance, help, encouragement and patience throughout this period of time.

I also would like to thank Xing Zhang and Richard Harkness. Discussions with them have been enlightening and have helped me extensively in understanding and carrying out the research.

My thanks further extend to many others who have, in various ways and at various times, helped me over the past years.

Finally, special thanks to my parents and my friends whose support has kept me going throughout.

The research described in this thesis was supported by an EPSRC ROPA research grant and a University of Southampton Ph.D. studentship, and by the Computational Engineering and Design Centre of the Faculty of Engineering and Applied Science.

# Contents

**List of Figures** **vii**

**1 Introduction** **1**

1.1 Objective . . . . . 1

1.2 Thesis structure . . . . . 2

**2 Background** **6**

2.1 General strength and stress-deformation characteristics of soil . . . . . 6

2.1.1 Interparticle friction . . . . . 7

2.1.2 Plane strain and axisymmetric conditions . . . . . 12

2.2 Shear bands in soils . . . . . 14

2.2.1 Methods of observation . . . . . 14

2.2.2 Shear band angle of inclination and thickness . . . . . 15

2.2.3 Micro-structure inside a shear band . . . . . 18

2.2.4 Conditions of formation . . . . . 18

2.3 Discrete element approaches in numerical analysis of soil . . . 19

2.3.1 Excessive rolling of spherical particles . . . . . 20

2.3.2 Restrain the rotation of individual particles . . . . . 21

2.3.3 Using polygons or elliptically shaped particles . . . . . 22

2.3.4 Using clusters of bonded disks . . . . . 24

**3 Introduction to Discrete element modelling 26**

3.1 Introduction . . . . . 26

3.2 The particle flow model . . . . . 28

3.2.1 General information about PFC–3D . . . . . 29

3.2.2 Basic calculation procedure . . . . . 31

**4 Numerical simulations of granular material using spheres 34**

4.1 Introduction . . . . . 34

4.2 Modelling procedure . . . . . 35

4.3 Effects of different initial porosity . . . . . 38

4.4 Interparticle friction angle . . . . . 41

4.5 Effect of particle rotation on shearing resistance . . . . . 46

4.6 Summary . . . . . 49

**5 Numerical simulation of direct shearbox test 51**

5.1 Introduction . . . . . 51

5.2 Modelling procedure . . . . . 54

5.3 Sequence of analysis . . . . . 56

5.4 Effect of number of particles . . . . . 60

5.5 Effect of normal stress . . . . . 62

5.6 Effect of particle shape . . . . . 65

5.7 Effect of interparticle friction angle . . . . . 67

5.8 Micro-deformation of shear zones . . . . . 70

5.9 Summary . . . . . 72

**6 Numerical simulation of biaxial test 75**

6.1 Introduction . . . . . 75

6.2 Numerical modelling procedure . . . . . 77
6.3 Loading platen friction . . . . . 83
6.4 Initial sample porosity . . . . . 90
6.5 Particle shape factor . . . . . 94
6.6 Interparticle friction angle . . . . . 97
6.7 General discussion . . . . . 101
6.8 Summary . . . . . 105

**7 Summary and Conclusions** **108**
7.1 Simulation of granular material using spheres and the limitations of this approach . . . . . 109
7.2 Effect of particle shape . . . . . 111
7.3 Effect of particle properties and boundary conditions . . . . . 112
7.4 Suggestions for future research . . . . . 115
7.4.1 Limitations of the numerical simulations . . . . . 115
7.4.2 Modelling the behaviour of granular material . . . . . 116

**References** **118**

# List of Figures


2.1 The actual particle can be closely resembled by a circular disks cluster . . . . . 24

3.1 Calculation cycle in PFC–3D . . . . . 31

4.1 Schematic illustration of the shear box . . . . . 36
4.2 A sample before shearing . . . . . 36
4.3 Monitoring system used in the simulations of shearbox test using 1 $mm$ spheres . . . . . 37
4.4 Stress-strain behaviour and change of void ratio of samples with different initial porosity . . . . . 39
4.5 Observed and corrected shearing resistance curves for shear-box test simulation using 1 $mm$ spheres . . . . . 41
4.6 Stress-strain behaviour and volumetric dilation of samples with different $\phi_\mu$ . . . . . 42
4.7 $\phi'_{cv}$ of spherical particles plotted against $\phi_\mu$ . . . . . 44
4.8 Particle rotation of samples consist of $1mm$ spheres $\phi_\mu = 5°$ and $\phi_\mu = 30°$ respectively . . . . . 45
4.9 Difference of shearing resistance of the samples with different restraints of particle angular velocity . . . . . 48

5.1 Grading curve of the sample . . . . . 53
5.2 Illustrate bonded particle . . . . . 54
5.3 A sample before shearing . . . . . 55
5.4 A sample after shearing . . . . . 56
5.5 Repeatability of shearbox test simulation . . . . . 57
5.6 Bulk strength and volumetric dilation of a typical numerical sample and reference real sand . . . . . 59
5.7 Effect of varying particle size on bulk strength and volumetric dilation of numerical samples . . . . . 61
5.8 The effect of normal stress on shear strength and specific volume of a typical numerical sample . . . . . 63
5.9 Shear strength of real sand and its specific volume after shearing. 64
5.10 Effects of particle shape on sample strength and dilation . . . 66
5.11 Effect of interparticle friction angle on sample strength and dilation . . . . . 68
5.12 $\phi'_{cv}$ of non-spherical particles plotted against $\phi_\mu$ . . . . . 69
5.13 Particle rotation and displacement of a typical sample after shearing . . . . . 71

6.1 The scheme illustration of biaxial test . . . . . 78
6.2 Biaxial test model and a typical sample . . . . . 80
6.3 Particle size distribution of sands and numerical samples. . . . 80
6.4 Numerical samples at 16.7% axial strain using rough/smooth platens . . . . . 83
6.5 Shearing resistance and volumetric dilation of the samples shown in Figure 6.4(a) . . . . . 85
6.6 Contours of $\sigma'_1$ at peak shearing resistance calculated by the continuum code FLAC . . . . . 86

6.7 Individual particle rotations in the numerical samples having various loading platen friction angles . . . . . 89
6.8 Shearing resistance and volumetric dilation of the sample with various initial porosities . . . . . 91
6.9 $(\phi'_{peak} - \phi'_{crit})$ against relative density. Correlation of numerical samples with various sands from literature (average effective stress approximately 300 $kPa$) . . . . . 92
6.10 Particle rotations in numerical samples with various initial porosities . . . . . 93
6.11 Shearing resistance and volumetric dilation of the samples with various shape factors . . . . . 95
6.12 Particle rotations in numerical samples with various shape factors . . . . . 96
6.13 Shearing resistance and volumetric dilation of the samples using rough platens with various interparticle friction angles $\phi_\mu$ . 98
6.14 Particle rotations in numerical samples with various interparticle friction angles . . . . . 99
6.15 Shearing resistance and volumetric dilation of the samples using smooth platens with various interparticle friction angles $\phi_\mu$ . . . . . 100
6.16 Material continuum properties: calculated angles of shearing resistance for $\phi'_{peak}$,$\phi'_{end}$ and $\phi'_{cv}$ . . . . . 105

# Chapter 1

# Introduction

## 1.1 Objective

In the research reported in this thesis, numerical simulations are carried out by using a three-dimensional discrete element method (DEM) computer code PFC–3D (Itasca Consulting Group Inc., 1997) to investigate the effect of various factors, including particle properties and loading conditions, on the mechanical response of cohesionless granular material under general engineering stress conditions without grain crushing and the influence of fluid. The main objectives are

1. To simulate granular particles using spheres and to understand the limitations of such an approach.

2. To simulate granular material using non-spherical particles (pairs of strongly bonded spheres) and investigate the effects of particle shape on a sample's stress-strain behaviour.

3. To simulate laboratory tests in direct shear and biaxial compression, and to examine the effects of particle size and interparticle friction

angle, as well as differences in boundary and starting conditions such as different confining stresses, initial porosity and friction angle of loading platen on the macro and micro behaviour of simulated soil masses.

## 1.2 Thesis structure

In Chapter 2 (Background study), the relevant areas of the large body of studies which investigates the mechanics of soils is reviewed. The strength of a cohesionless soil is largely affected by particle properties (particle shape, interparticle friction angle) and loading conditions (testing method and boundary conditions). The failure of soil often appears as the formation of shear bands. Particular attention is drawn to the particle rotation on the shear band. The formation, width and inclination angle of shear band are also related to soil properties and boundary conditions.

The second part of Chapter 2 focuses on numerical simulation using the Discrete Element Method (DEM). Although this helped in understanding some fundamental aspects of behaviours of granular material, early researches showed that a disk/sphere was not a close enough approximation of real soil particle. Aiming at overcoming some inherited limitations of using circular/spherical particles, recent development of modelling techniques, such as introducing a more complicated interaction model (bonding and rotational resistance mechanism) at a contact point, or using elliptical particles instead of spheres, together with the improvement of computer technology (in terms of speed and capacity), have made the discrete element method a popular tool in examining directly not only macro stress–strain behaviour but also micro mechanism of deformation and failure of particle assemblages.

Chapter 3 (Introduction to discrete element modelling) briefly describes

the conceptual model and mathematical background of the discrete element method, in particular the computer code PFC-3D, which is an simplified implementation of the DEM. Its general mathematical background and some specific features which are important to this study (such as the facility to bond particles together) are also presented in this chapter.

Chapter 4 (Numerical simulations of granular material using spheres) describes the modelling procedures of direct shear box test using a random assemblage of spheres. The simulations were carried out in a numerical split box which replicated the standard laboratory shearbox apparatus. The peak shearing resistance and volumetric dilation of the samples increased with increasing initial packing density and interparticle friction, but all samples reached almost the same shearing resistance when they were approaching their critical states. The results from numerical simulations and laboratory tests shared the same trend: interparticle friction angle had little effects on sample's shearing resistance when they deform at constant volume ($\phi'_{cv}$), which differed from a theoretical prediction by Horne (1969). This is because the theoretical analysis was based on the assumption that particles only slided against each other and predicted an increase in $\phi'_{cv}$ with interparticle friction angle. However, observation of the movement of individual particles revealed that particle rotation played a major role in sample deformation. Further simulations in which the degree of rotation of the spheres was restrained showed that the particle rotation was an important, if not overriding, factor to the shear resistance of the assemblage, and reducing particle rotation led to the increase of shearing resistance. The simulations also showed that when spheres were free to rotate, a sample comprising of uniform sized spheres had a lower shearing resistance than a sample comprising various sized spheres. This might result from the lower porosity of

a finer graded sample. The major limitation of simulating materials such as sand using spheres was highlighted: excessive particle rotation would lead to unrealistically low shearing resistance and volumetric dilation.

Chapter 5 (Numerical simulations of direct shearbox tests) describes the simulations of direct shearbox tests on samples comprised of non-spherical particles. In this study, non-spherical particles were formed by bonding two spheres together to overcome the limitations (such as excessive rolling of particles) of simply using spheres. The term 'shape factor' is introduced to describe the shape of a bonded particle. Assemblies modelled followed the relative size distribution of a medium Leighton Buzzard sand. The significance of using bonded particles was discussed by comparing the results with those from Chapter 4. The results from a typical sample were compared with those from a real sand with a similar size distribution. The particle shape had a significant effect on the stress–strain behaviour of samples: both shearing resistance and volumetric dilation of the samples increased dramatically when particles became less spherical. The number of particles in the sample mostly affected the residual shearing resistance and the volumetric dilation. However, more than 15000 particles would be needed to make the effect of particle number less marked. In contrast to the behaviour of samples consisting of uniform sized spheres, higher value of $\phi'_{cv}$ was observed when the interparticle friction angle was increased. The major deformation of each sample is concentrated in a narrow zone of intense rotation in the middle of the sample and marked by a number of particles with high degree of rotation.

Chapter 6 (Numerical simulations of biaxial tests) describes numerical biaxial tests on samples having the same particle size distribution as used in the shearbox tests. The effects of particle properties and loading conditions (initial porosity, friction of loading platens, confining stress) on the

strength-dilation behaviour of samples were examined. It was shown that an assembly with lower initial porosity or higher $\phi_\mu$, or composed of particles that were less rotund had higher peak shearing resistance associated with higher dilation rate. The higher friction angle on loading platens would cause strain localisation within the sample and therefore produce a higher $\phi'_{peak}$ and a prompt failure later on. The internal structures that developed in the biaxial test simulations were explored. Sample deformation was investigated by quantifying the rotation of individual particles within a selected section. The initial porosity and friction at the loading platens were found to be important factors to the formation of shear bands. The development of shear bands and their width and angle of inclination are discussed for a typical sample.

A general discussion and summary of this study, together with recommendations for possible further work, are given in Chapter 7 (Summary and conclusions)

# Chapter 2

# Background

## 2.1 General strength and stress-deformation characteristics of soil

The stress-deformation and strength behaviour of soils is of importance in any problem where ground movements are involved. In geotechnical engineering, strength may be defined as the ability to resist shear (Powrie, 1997). Most relationships used in practice for characterising the strength properties of soils are empirical(Bishop, 1966). By far the most widely used is the Mohr–Coulomb equation:

$$\tau = c' + \sigma' \tan \phi' \tag{2.1}$$

where $\tau$ is the shear stress at failure on the failure plane, $\sigma'$ is the normal effective stress, $c'$ and $\phi'$ are effective stress strength parameters.

It is well recognised that the shear resistance of a soil depends on many factors including both macro characteristics of the assembly, such as porosity, stress history, temperature, strain, strain rate, soil structure etc., and micro characteristics of individual particles such as mineralogy, shape, and surface

condition (texture and moisture). For a given soil, values of $c'$ and $\phi'$ are determined by a particular test type (e.g., direct shear, biaxial or triaxial compression, simple shear), for given confining stress, drainage conditions, loading rate, stress history etc. These factors may not all be independent and their combined effects on the soil shearing resistance are not necessarily well understood (Mitchell, 1993).

### 2.1.1 Interparticle friction

Commonly, friction can be described by Coulomb's model of sliding of one block over another. Let

$$\phi = \tan^{-1} \frac{F}{N} \tag{2.2}$$

where the $N$ is the force perpendicular to the surface and $F$ parallel to it, then the angle $\phi$ is the largest inclination angle of the resultant force (of $F$ and $N$) to the slip surface.

Interparticle friction is generally taken to be the average coefficient of kinetic friction generated when one 'typical' particle surface is caused to slide slowly over another through a significant displacement (Procter and Barton, 1974).

Based on the above definitions, various experimental techniques, such as sliding a mass of free particles across a smooth block (Rowe, 1962) or one fixed particle over another (Skinner, 1969), were developed to measure the interparticle friction angle $\phi_\mu$ for a (granular) material as directly as possible. These experiments attempted to reveal the circumstances under which $\phi_\mu$ might be considered as a constant value and (maybe more importantly) to relate the shearing behaviour of a particle assemblage to the measured value of $\phi_\mu$.

### Testing conditions and $\phi_\mu$

The mechanisms of frictional motion are conceptually complex (Jaeger, 1971). Different or even contradictory experiment results are often obtained under different testing conditions and later lead to difficulties in interpretation. However, it is clear that the measured value of $\phi_\mu$ can be more sensitive to some factors than others.

Skinner (1969) observed a significant increase in $\phi_\mu$ for glass ballotini, steel balls and lead shot as the normal contact force increased from 0.06 to 1.1 Newton. This is in contrast with Procter and Barton (1974) and others who observed slightly decreasing or constant values of $\phi_\mu$ with increasing normal force. Procter and Barton assumed that the disagreements resulted from variations in the experimented ranges of normal force but gave no further evidence for this.

Another important factor that causes huge variations in measured values of $\phi_\mu$ is the surface condition of the particles. It is found that a different particle surface texture, which is largely related to grains' mineral nature, causes the particle to respond in different ways to surface chemistry effects, particularly to the presence of water (e.g. Mitchell, 1993; Santamarina and Cascate, 1998). Skinner (1969) found an increase in the coefficient of friction ($\tan\phi_\mu$) by a factor of ten when dry glass ballotini were flooded by water. Ishibashi et al. (1994) also reported an increase in the coefficient of friction when glass balls were flooded, but only by a smaller factor of two. In neither case, were further details such as surface cleanness and roughness given. In general, water has no effect on $\phi_\mu$ on chemically clean quartz surface, but serves as anti-lubricant when surface is 'dirty' (Bowden and Tabor, 1950, 1964). However, the anti-lubricant effect diminishes for rough surfaces (Procter and Barton, 1974).

A problem then arises when the shearing behaviour of an assembly of particles is to be related to $\phi_\mu$, as contact points in the mass are unlikely to have the same surface conditions. Hence the result of a single-contact test may not be representative. In order to more precisely represent the mass behaviour, an average value of $\phi_\mu$ by observing many sliding contacts simultaneously is needed. Therefore to this extent, the method described by Rowe (1962) and Frossard (1979) which employs a large mass of particles is more preferable to testing individual particles, because it will include the effects of any naturally presented surface condition.

### Shearing strength and $\phi_\mu$

The relationship between interparticle friction and shearing strength of mass of particles has been controversial. Based on the results of laboratory test, Bishop (1954) derived an approximation of $\phi'_{cv}$ (effective shearing resistance at constant volume) for triaxial compression in terms of $\phi_\mu$:

$$\sin \phi'_{cv} = \frac{15 \tan \phi_\mu}{10 + 3 \tan \phi_\mu} \tag{2.3}$$

and for plain strain conditions:

$$\sin \phi'_{cv} = \frac{3}{2} \tan \phi_\mu \tag{2.4}$$

After analysing the interactions among circles, Horne (1965) also proposed an expression of relationship between $\phi_{peak}$ and $\phi_\mu$ for a regular or isotropic random packing of uni-sized spheres:

$$\tan^2(\frac{\pi}{4} + \frac{\phi_{peak}}{2}) = 2 \tan(\frac{\pi}{4} + \phi_\mu) \tag{2.5}$$

These analytical (Horne's) or empirical (Bishop's) predictions suggest that shear strength increases with $\phi_\mu$. However, experimental results from various researchers have been found that both support and contradict these predictions. The results of shearbox tests on 1 *mm* and 3 *mm* glass ballotini, steel balls and lead shot reported by Skinner (1969) showed that the effective shearing resistance remained almost constant while $\phi_\mu$ was changed from 3° to over 40°. Bishop (1971) also reported similar findings from tests on rockfill and pebbles (quoting results from Tombs (1969)). Rowe (1971) claimed that the conditions which led to Skinner's results had not yet been fully understood. Tong (1970) reported that for glass ballotini, different values of $\phi_\mu$ (16° and 21° respectively, resulting from the different surface conditions) would lead to different peak angles of shearing resistance (37° and 46°). Procter and Barton (1974) suggested that the discrepancies might result from different methods used to measure $\phi_\mu$ (observing two particles as Skinner (1969) did, or a mass of particles as Rowe (1962) and Tong (1970) did) and that in the first case the tested particles might not have the same surface conditions.

Skinner (1969) believed that rolling was the dominative deformation mechanism when $\phi_\mu$ was high, and sliding when $\phi_\mu$ was low. The key to the unchanged shearing strength was that rolling was not more difficult than sliding. This conclusion was supported by Oda et al. (1982) who carried out biaxial shear tests on rod-like particles with oval cross sections. In Oda's tests, the shape of the particles can be described by axial ratio: $d_1/d_2$, where $d_1$ and $d_2$ are the long and short axis lengths respectively. For more round particles with $\frac{d_1}{d_2} \approx 1.1$, no dependence of the sample's peak angle of shearing resistance on $\phi_\mu$ was observed when $\phi_\mu$ was increased from 26° to 52°. On the other hand, for the particles with $\frac{d_1}{d_2} \approx 1.4$, the sample's peak angle of shear-

ing resistance increased by almost a third (from 39° to 52°) when $\phi_\mu$ was doubled from 26° to 52°. Those results suggested that particle shape, which has an effect on particle rolling, plays an overriding part in the behaviour of cohesionless soils (Bishop, 1971).

The importance of angularity or sphericity of particles was discussed by Koerner (1970) . The triaxial tests on three types of quartz sands with same $d_{10}$ value but different sphericity (from angular to subrounded) showed that the assembly of angular particles had significantly higher strength than that of more spherical particles.

Frossard (1979) investigated the effect of different grain shape as well as different mineralogy on the value of $\phi_\mu$ and concluded that the measured value of $\phi_\mu$ increased with angularity but was not significantly affected by the mineralogical nature of the grains. Dilatancy rate was also notably affected by sphericity.

It has long been recognised that the shearing resistance mentioned above ($\phi'$, see equation (2.1)) can be divided into two components: the frictional resistance between particles and the extra energy needed for volume change. Newland and Allely (1957) and Rowe (1962) considered the effect on $\phi'$ of the energy expended in expansion of the sample. The concept of the effective interparticle friction angle was then introduced as

$$D = 1 - \frac{d\mathrm{v}}{d\varepsilon_1} \tag{2.6}$$

$$\frac{\sigma_1'}{\sigma_3'} = D\tan^2(\frac{\pi}{4} + \frac{\phi_f}{2}) \tag{2.7}$$

where v is the volume change per unit volume, $\varepsilon_1$ is the major principle strain, $\sigma_1'$ and $\sigma_3'$ are the major and minor principle effective stress, and $D$ is dilatancy rate. Rowe (1962) suggested that in plane strain conditions

for any packing density and stress ratio up to the peak value, the effective interparticle friction angle $\phi_f$ would equal to the mobilised friction angle at the critical state, $\phi_{cv}$. In triaxial tests, on the other hand, for dense samples the $\phi_f$ would equal to true interparticle friction angle $\phi_\mu$ and for loose samples $\phi_f = \phi_{cv}$. This was later confirmed by laboratory test data (e.g., Rowe, 1969; Lee, 1966; Lee and Seed, 1967). Clearly $\phi_f$ is the result of a combination of particle rolling and sliding resistance.

### 2.1.2 Plane strain and axisymmetric conditions

Soil strength is always interpreted in terms of a failure criterion. Although many different criteria have been proposed (e.g., Roscoe et al., 1958; Bishop, 1966; Kirkpatrick and Belshaw, 1968), the Mohr-Coulomb criterion is the most commonly used one, in which only the major and minor principal stresses are used to define failure. Therefore it could be argued that a plane strain test, in which the intermediate principal stress may not be the same as either of the other stresses, is unnecessarily complex, given the fact that performing a test under axisymmetric condition (conventional triaxial test) is easier and its results are reliable.

However, many soil problems involving shear strength, such as embankments, earth dams, retaining walls, strip footing, tunnels, cuttings for roads and most of landslides etc., approximate to plane strain condition because the movement in the longitudinal direction is precluded by the shape of the construction. Although the fact that many of important structures were successfully constructed using strength parameters obtained from triaxial tests may suggest that the distinction between symmetric strain and plane strain condition might not be important for routine engineering design, it is still more valuable to engineers if the soil strength parameters to be used are

known to correspond more closely with reality.

Finn et al. (1967) used the rigid sphere model in which to investigate some aspects of the plane strain problem and found that the ideal plane strain sample was stiffer and stronger than the corresponding triaxial sample, but that the triaxial sample showed a greater tendency to dilate. Cornforth (1964) and Bishop (1966) reported that for dense sand the peak strength (effective internal friction angle) determined in a biaxial test could be up to 8° higher than determined in a triaxial test but that loose sand showed little difference in either method. It also has been found that plane strain tests require less than half the axial strain to fail compared with triaxial tests (Cornforth, 1964; Henkel and Wade, 1966). On the other hand, Bolton (1986) and Schanz and Vermeer (1996) reported that, for at least some sand, both conditions yield almost the same dilation angle $\nu$ and the critical state shearing resistance $\phi_{cv}$ is not affected either. A more comprehensive discussion can be seen in paper of Lee (1970).

In drained triaxial tests using porous disks as the end platens, failure of the sample usually concentrates either in a central zone or in a narrow rupture surface and the volume change does not reflect the whole sample (Rowe and Barden, 1964; Lee and Seed, 1964; Barden and McDermott, 1965). The sample may reach a critical state soon after the peak stress because of the development of a predominant slip surface, with the critical state only actually being achieved in the failure zone. One of the main reasons for non-uniformity of stress in a triaxial test is friction at the loading platens, as the restraining effect at the platen leads to the formation of the 'dead zone' at the ends of the sample in which the sample hardly deforms.

Rowe and Barden (1964) were among those who experimented using lubricated platens to overcome this disadvantage. They concluded that decreasing

the friction on the loading platen led to a lower peak shearing resistance. It also led to the removal of the dead zone, enabled a shorter sample to be used and achieved a more stable geometry. Bishop and Green (1965) confirmed that very efficient lubrication (two layers of thin greased membrane) was necessary to reduce the strength of a sample having a height to diameter ratio of 1 to that of a sample having a ratio of 2. The use of frictionless loading platens also helps to develop uniform dilation, even in a slender sample (Lee and Seed, 1964); thus the critical void ratio can be attained within the entire sample. The rate of dilation when the sample reaches peak shearing resistance, however, is not significantly affected by the end restraint (Bishop and Green, 1965).

## 2.2 Shear bands in soils

Deformation within granular soils is commonly concentrated in shear bands and ruptures. These localised features may be the dominant factors in controlling the overall behaviour of a particulate material. Much work have been devoted to analysing shear bands.

### 2.2.1 Methods of observation

Roscoe (1970) used X-ray techniques with lead shot to indicate a 'dark band' in the sample which represents the rupture surface. A similar observation was made using the same technique by other researchers, e.g., in the directional shear cell by Arthur and Phillips (1975) and Arthur el al. (1977$a, b$), and in a plane strain biaxial test by Vardoulakis and Graf (1982). Later, a computer-enhanced X-ray method (Computed Tomography) provided a powerful tool to obtain the void patterns on specific planes (slices of the sample)

and later to generate a three dimensional view of sample's internal density distribution(Desrues et al., 1996). Along with the Radiographic technique, the stereophotogrammetric method was used to measure the displacement field (Butterfield et al., 1970) and Desrues et al. (1985) further developed the method to quantify strain measurements in plane strain specimens, especially the volumetric strain in the shear bands. Harris et al. (1995) and (Finno et al., 1996, 1997) also used this method to examine the changes in width and angle of inclination of shear bands throughout their evolution. Recently Alshibli and Sture (1999) demonstrated that digital imaging techniques could be used for monitoring the localisation of deformation in the soil samples.

### 2.2.2 Shear band angle of inclination and thickness

The two most obvious and significant characters of a shear band are its direction and thickness, although to quantify them is not easy.

Classical theories for shear band inclination in sand subjected to plane strain are commonly referred to as Coulomb's and Roscoe's angles. Coulomb's angle arises from the assumption that the stress obliquity (i.e., the ratio of shear to normal effective stress) is maximal along the shear band. Coulomb's angle is given by

$$\theta_C = 45^\circ + \frac{\phi'}{2} \tag{2.8}$$

where $\theta_C$ is the angle between the shear band and the direction of minor principal effective stress predicted by Coulomb. The equation has one static parameter $\phi'$ and no deformation variables.

Roscoe (1970) assumed, on the bases of observations of laboratory tests, that the inclination angle of the shear band corresponded more closely to

the maximum strain obliquity in terms of strain rates. Roscoe's angle is presented as

$$\theta_R = 45^\circ + \frac{\nu}{2} \tag{2.9}$$

where $\nu$ is the dilation angle at failure, which is defined as

$$\nu = -\sin^{-1}\frac{d\varepsilon_1^p + d\varepsilon_3^p}{d\varepsilon_1^p - d\varepsilon_3^p} = \sin^{-1}\frac{D-1}{D+1} \tag{2.10}$$

where $\varepsilon_1^p$ and $\varepsilon_3^p$ are major and minor plastic principal strains, respectively. $D$ is dilatancy rate (see equation (2.6)).

Experimental evidence (e.g., Vardoulakis, 1980; Vardoulakis and Goldscheider, 1981; Han and Drescher, 1993; Finno et al., 1997; Oda and Kazama, 1998; Alshibli and Sture, 2000) had confirmed that most shear bands lie between those two bounds ($\theta_R \leqslant \theta \leqslant \theta_C$). Based on reported experimental results, Arthur et al. (1977) proposed an intermediate angle:

$$\theta_A = \frac{\theta_C + \theta_R}{2} \tag{2.11}$$

This solution was later supported by Vardoulakis (1980) on both theoretical and experimental bases.

The shear band boundaries are not always straight and are sensitive to boundary conditions (Vardoulakis et al., 1978; Oda and Kazama, 1998). Accordingly the inclination angle is not a material constant. Vermeer (1990) argued that the inclination angle decreased with increasing particle size as a result of out of balance forces at the end of the shear band caused by stress discontinuity. Han and Drescher (1993) reported that increasing the confining stress $\sigma_3$ would reduce the lower shear band inclination angle.

The thickness of the shear band is also of interest. Roscoe (1970), Scarpelli

and Wood (1982) and Oda and Kazama (1998) reported that the width of the shear band was about 10 times the average grain diameter based on direct experimental observation using X-rays or an optical microscope. Vardoulakis and Graf (1985) observed a greater shearband thickness of about 18 typical particle diameter. Mühlhaus and Vardoulakis (1987) investigated both the width and the direction of the shear band using bifurcation and plasticity deformation theory for granular materials that contain micro-structure (micro polar theory). The predicted shear band width agreed well with Roscoe's observation. Bardet and Proubet (1992) also supported the micropolar theory on the basis of the results derived from a numerical simulation of an assembly of circular particles. However, Harris et al. (1995) and Finno et al. (1996, 1997) reported an even greater shear band thickness of over 30 typical particle diameter in loose sands. The reason for this large difference is not fully understood.

Shear bands are generally not regular in shape, and do not have a constant width. The width of a shear band often changes during its development. Oda and Kazama (1998) reported that the shear band thickness expanded over 0.5 $mm$ during the biaxial test using Toyoura sand.

It is believed that two mechanisms are responsible for the widening of the shear band:

1. The shear band boundaries move as more particles are involved into the development of the shear band.

2. Particles inside the shear band dilate and push the boundaries apart.

However, some experimental evidence suggests that the latter one be indeed the key factor (Harris et al., 1995; Oda and Kazama, 1998).

### 2.2.3 Micro-structure inside a shear band

As dilation occurs inside a shear band, large voids are generated. Oda and Kazama (1998) reported that, for two different sands, void ratios inside the shear band were greater than the maximum void ratio determined by standard methods while outside the shear band the void ratio remained unchanged from the initial value. Similar behaviour was observed in a numerical simulation (Iwashita and Oda, 1998) as well as a biaxial compression test on rod-like particles (Oda et al., 1982). The reason of the development of the very large void ratio is not yet fully understood.

Particles inside the shear band rotate significantly more than those outside. Oda and Kazama (1998) found that non-spherical particles normally lie on the horizontal plane with their long axes parallel to it when deposited under gravity. Within the shear band, particles were reoriented and for one type of sand (Toyoura sand) it was found most sand grains had rotated to give an angle of about $44^\circ$ between the long axes and horizontal plane.

Large dilatancy and particle rotation cause the structure inside the shear band to be highly anisotropic.

### 2.2.4 Conditions of formation

Drescher (1976) observed bright bands in stressed assemblies of optically sensitive glass particles under polarising light and interpreted them as principal stress trajectories. Oda and Konishi (1974) suggested that anisotropy was induced during shearing up to the peak stress, such that the principal axes of anisotropy (defined as the unit vectors normal to the contact surfaces at the contact point between two particles) tended to follow the principal stress axes, and each particle rotated such that its long axis oriented perpendic-

ular to the maximum principal stress direction. Oda and Kazama (1998) reported the formation of the column-like structures through which the axial load was mainly transmitted. These structures stated the concentration of contact normals and strains. Anisotropy induced by the column-like structure is common in the strain-hardening process of granular materials (Frost and Jang, 2000).

The column-like structures collapse by a mechanism similar to buckling after the peak stress at the places where shear bands will develop. No clear shear band will generate if anisotropy induced by the column-like structures are not well developed at the peak stress. It has been reported that shear band will not appear in the following conditions:

1. in a very loose sand in which no obvious strain softening occurs after the peak (Han and Vardoulakis, 1991).

2. where the direction of the major principal stress continuously changes (Arthur et al., 1980).

3. where particles are crushed under the stress (Tatsuoka et al., 1990).

It is clear that these condition are all related to failure of stable columns which can transmit the applied stress.

## 2.3 Discrete element approaches in numerical analysis of soil

Discrete element numerical modelling methods have been used increasingly over the past decade or so to investigate the behaviour of a granular mass from a micromechanical point of view. The merits and problems of such

approaches associated with particle shape are reviewed in the following sections.

### 2.3.1 Excessive rolling of spherical particles

Idealised particles, such as steel balls, were often used in the laboratory tests to establish the basic understanding of behaviour of granular materials under stress (e.g., Rowe, 1962; Wroth and Bassett, 1965; Finn et al., 1967). It has been known that the mechanical response of an assembly of ideal spheres has similar features to the deformation of soils but the magnitudes of the parameters differ. The classic stress–dilatancy theory based on analysing the sliding movement of circles (Rowe, 1962; Horne, 1965, 1969) showed reasonable agreement with the behaviour of a range of different granular materials (e.g., Lee, 1966; Bolton, 1986).

Although the discrete element method need not be restricted particles of any particular shape, it is natural to base the numerical solution on circles/spheres as they have been proved to be useful and valid in representing the soil grains while at the same time offer great numerical efficiency with respect to contact detection and particle interactions (such as the transferring of forces and moments). Circular elements were used to model the granular materials in most previous numerical simulations using the discrete element method (e.g., Cundall and Strack, 1979; Cundall, 1989; Ting et al., 1989; Bathurst and Rothenburg, 1990; Bardet and Proubet, 1991). Those studies revealed the great potential of using this numerical method to investigate the micro- and macro-mechanical behaviour of granular media.

However, the circular elements suffered the same drawbacks as the steel balls in the lab tests: the perfectly circular shape of the particles makes them tend to roll excessively, resulting in lower overall strength. The shape of a

particle clearly affects the interaction between individual grains. The ideal circular shaped particles interact at a single contact point with the only resistance to rolling being the surface friction with surrounding particles, as the normal force is always pointing towards the centre of a particle. On the other hand, natural sand grains do not always have a perfect spherical shape. Mitchell (1993) pointed out that it was typical for sands to have more than half of their particles with a length to width ratio of more than 1.4. It is known that irregularly shaped particles interact through multiple contact points or contact surfaces (Roscoe and Schofield, 1964). This different contact model allows the moments to be transmitted across these points (surfaces) thereby further restricting the rotation of the particles. Sphericity has a significant effect on volume strain, especially on the maximal angle of dilation (Frossard, 1979). It is difficult to obtain a loose (void ratio greater than 0.27) assembly of perfect circles (Mitchell, 1993). The problem of excessive rolling in numerical simulations has been demonstrated by many researchers (e.g., Ting et al., 1989; Bathurst and Rothenburg, 1990; Bardet and Proubet, 1991; Ng and Dobry, 1992).

Many researchers have tried to modify or enhance their simulations to overcome the problems of using disks. These approaches can be generally divided into two major methods.

### 2.3.2 Restrain the rotation of individual particles

Ting et al. (1989) were among those who reported the effect of individual particle rotation on an assembly of granular material. Their samples used 562 disks with three radii, producing unusually low strength in their DEM simulations of biaxial tests. The internal friction angle of the sample was lower (as low as 18°) than the interparticle friction angle ($\phi_\mu = 25°$). Ting

et al. concluded that the particle rotation was the key factor controlling the strength and deformation. They then restrained the rotation by artificially increasing the polar moment of inertia of each particle. Mobilised friction angles closer to those of sand were thus obtained. Ng and Dobry (1992, 1994) also compared the mobilised friction angles obtained in their simulations using 240 disks with $\phi_\mu = 20°$. A increase of 19° (from 14° to 33°) was observed when the particle rotation was restrained completely. Recently Iwashita and Oda (1998) added rotation stiffness into simulating contacts between particles. Introducing this restraint not only affected a sample's shear strength but also caused strain localization. Compared with tests using free rolling particles, higher peak shear strength and clear voids localization resulted from restricting the particles from rolling.

All of those approaches involve the artificially adjustment of some numerical parameters to compensate for the circular particle shape used. Although they might seem to be effective, however, those adjustments are not satisfactory as they can hardly be related to any observable quantity.

### 2.3.3 Using polygons or elliptically shaped particles

An alternative attempt is to use non-circular particles which will more accurately represent the actual shape of natural media. Issa and Nelson (1992) employed arbitrary polygonal elements and yielded better qualitative agreements with experiment. However, using irregularly shaped particles significantly decreases the numerical efficiency. For example, contact detection is very difficult as there are so many edges that require monitoring. Also different contact types (corner to corner, corner to edge and edge to edge) need to be treated and the change from one type to another is not easy. Ting et al. (1989) indeed reported that compared to disks, using polygon shaped

particles in simulations would need an increase of computing time of at least one order of magnitude.

A number of researchers have implemented elliptical particles. Rothenburg and Bathurst (1992) investigated the relationship between particle shape and the peak friction angle and peak dilation rate. A peak friction angle more comparable to that of real sand (42°) was obtained when the particle aspect ratio (particle's length over width) was 1.5. The volumetric dilation of the assembly was found to be close to that of real sand as well. Ting et al. (1993) also reported an increase of 20° (from 25° to 45°) in peak friction angle when the particle aspect ratio was increased from 1 to 2. Lin and Ng (1997) observed similar behaviour in three dimensional DEM simulations. The sample using ellipsoids produced higher strength and a higher dilation than those of using spheres. Using elliptical particles not only has been shown to restrict particle rotation and produce more realistic strength and dilation of samples but also provide a method of studying the effect of initial anisotropy of particle orientation. An extensive investigation of elliptical particles (Ting et al., 1995) demonstrated that the increase of a sample's strength in a simulation could result from the fabric of the sample as well as from the particle shape. The mobilised friction angle differed less than 5° between circular disks and elliptical particles with an aspect ratio of three with their long axis oriented over 60° from horizontal. On the other hand, an increase from of 30° (25° to 55°) was observed when the elliptical particles were packed with their long axis horizontal. Random packing of the ellipses did not significantly increase the sample's shear strength either, only about 5° difference was found.

Although using elliptical particles can more realistically simulate the real sand, it again suffers from numerical inefficiency. Disadvantages include contact detection, which requires the solution of a fourth-degree algebraic equa-

tion (Lin and Ng, 1995). The numerical complexity of the direct modelling of a non-circular particle makes the extension from two dimensions to three dimensions very difficult and simulations involving a large number of particles become virtually impractical.

### 2.3.4 Using clusters of bonded disks

As discussed in the previous section, using circular disks or spheres has the advantage of computational efficiency but cannot accurately replicate the interactions between the real sand grains. On the other hand, using non-circular/spherical particles can reduce the excessive rolling of the particles and model a sample's behaviour more accurately, but its complexity and demanding of high computing capacity prevent it from being widely adopted.

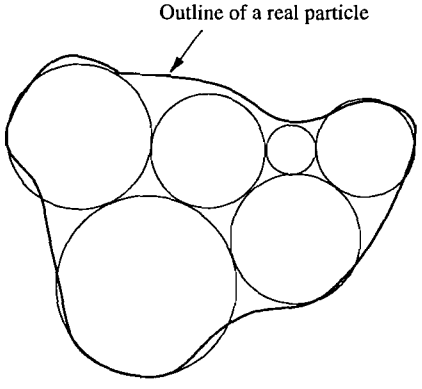


Figure 2.1: The actual particle can be closely resembled by joining a certain number of circular disks. The disks forming the particle behave like one rigid body

To overcome these shortages, the idea of clustering is a obvious solution. While the idea may not be new (e.g., Trent and Margolin (1992) modelled cemented granular solids using bonded particles), it is recently that the clusters have been used to give individual particles a rough outline. Theoretically arbitrarily shaped particle can be modelled by bonding a certain number of

simple shaped particles together, as in Figure 2.1. However, such a degree of complexity is not really necessary when modelling a real sand. Jensen et al. (1999) bonded together three circular disks with the same radius to form a cluster (the distances between each pair of disk centres in the cluster are the same) and compared the performance of 1000 clustered particles to that of 1000 circular disks in the simulated ring shear tests. The clusters rotated significantly less than circles thus increasing the strength of the sample. In another study of biaxial test simulations using the same type of three-disk cluster, Thomas and Bray (1999) reported a decrease of up to 40% in average particle rotation and a 12.5° increase in peak mobilised friction angle compared to the sample using circular disks.

Using clusters would require a larger computer capacity as substantially more disks are used. Jensen et al. (1999) found that simulations using clusters took almost three times longer to finish compared with those using simple circular disks as each cluster consisted of three disks. However, the slowdown is compensated by its better accuracy in replicating the behaviour of real sand. Also, the simplicity of its contact detection makes it much easier to be extended from 2–D to 3–D.

# Chapter 3

# Introduction to Discrete element modelling

## 3.1 Introduction

The discrete nature of granular material such as sand makes the constitutive relations of such a medium very complex. Therefore, the conventional laboratory methods (see §2.2.1) of studying the micro-structure and the behaviour of particles within an assembly are either difficult to perform or very time consuming to interpret afterwards. With the development of computer technology, it is now possible to explore the micro-mechanics as well as the macro-mechanics of granular materials in an alternative way. Computer simulations provide precise control over all parameters and the ability to present all the desired data. Special features such as truly identical samples and some extreme condition (e.g., completely frictionless surface) are obtained easily, which would be impossible to create in reality.

Soil is often simulated as a continuum. However, this approach often utilizes a complex constitutive model which includes many material constants

with no explicit physical meaning (which might result from the implicit expression of the geometry of an assemblage of particles) (Oda and Iwashita, 1999), and simulating large deformation and particle rotations may also be difficult.

An alternative is the discontinuum method which differs from the continuum method by the existence of contacts or interfaces between the discrete bodies that comprise the system. Thus, a numerical model must represent the mechanical behaviour of both discontinuities and solid material. Summarised by Cundall and Hart (1992), the discrete element method (DEM) is a type of computer programme for modelling discontinuous systems, which is able to simulate finite displacements and rotations of discrete bodies, including complete detachment, and automatically recognising new contacts as the calculation progresses. The explicit time–marching finite difference scheme used in DEM is based on the equations of motion and avoids the inversion process for stiffness matrices. A problem can be solved through a step by step procedure because the equilibrium equations of simulated bodies need not to be assembled into a large global matrix to solve the equations of the whole domain. Thus, DEM has two advantages when compared with continuum methods: being able to handle more elements within a relatively small computer memory space, and simulating the separation and the rotation of elements.

The discrete element method, in theory, is a hybrid model which can handle internally deformable solid bodies with arbitrary shapes and deformable interfaces amongst them (Itasca Consulting Group Inc., 1999). Originally developed by Cundall (1971) to analyse rock mass problems using angular blocks, the method was later applied to granular material such as soil (Cundall and Strack, 1979) by simplifying the geometry of the simulated elements

from polygons to circles. The governing equations of such models are a set of equilibrium equations for the resultant forces and moments at centres of the particles which emerge from contact forces, body forces, inertia forces and damping forces. In a matrix form, the governing equations can be expressed as

$$M\Delta\ddot{X} + C\Delta\dot{X} + S\Delta X = \Delta F \tag{3.1}$$

where $M$, $C$ and $S$ are the mass, damping and stiffness matrices respectively, $\Delta X$ is the incremental displacement vector including incremental rotations, and $\Delta F$ is the incremental force vector including incremental moments. $S$ generally changes during an analysis procedure because of the nonlinear character of granular materials.

Numerical simulation using the discrete element method is now a valuable and powerful tool in understanding the micromechanics of granular materials. To some extent it is actually pioneering the studies because of its unique capabilities in the research into extreme conditions such as frictionless particles and boundaries.

## 3.2 The particle flow model

PFC–3D (Particle flow code in three dimensions) computer code is one of the implementations of the discrete element method. It models the movement and interaction of assemblies of spherical particles under stress. Some basic conceptual models and the mathematical background of PFC–3D are presented in the following sections. However, this is not intended to be a detailed discussion of PFC–3D . Further information with regard to DEM or PFC–3D can be found in the PFC–3D manual (Itasca Consulting Group

Inc., 1997).

### 3.2.1 General information about PFC–3D

PFC–3D can be viewed as a simplified implementation of the DEM because of the restriction to rigid spherical particles whilst the DEM itself is not restricted to particles of any specific shape. The assumptions made in the particle flow model are:

1. The spherical particles are treated as rigid bodies.
2. The contacts occur over an infinitely small area.
3. A deformable contact approach is used. Therefore the rigid particles are allowed to overlap one another slightly at the contact points.
4. The magnitude of the overlapping is related to the contact force calculated by the force–displacement law and the contact stiffness model can be either linear–elastic or a simplified Hertz–Mindlin model.
5. The slip condition between particles is given by the Mohr-Coulomb law.
6. Bonds can exist at contacts between particles.

When the spheres are rigid and the contacts are 'soft', the mechanical behaviour of such a system can be described in terms of the movement of each particle and the interparticle forces acting at each contact point. For a granular assembly such as sand, this is a reasonable approximation under low stress (as in the research reported in this thesis) since the deformation of the assembly primarily results from the sliding and rotation of the particles as rigid bodies and not from individual particle deformation.

In addition to spheres, PFC–3D offers the 'wall' to allow one to apply velocity controlled boundary conditions to an assembly of particles. The spheres and walls interact with one another via the forces that arise at contacts. However, a wall is not affected by the force acting on it; its motion is specified by a user and stays constant regardless of the contact force. There is no direct interaction between two walls.

The constitutive model acting at a particular contact consists a stiffness model, a slip model and a bonding model. The linear–elastic model which provides an elastic relation between the contact forces and relative displacements in the normal and shear directions was used for the contact stiffness model in all numerical simulations carried out for the research reported in this thesis. This contact model is defined by the normal and shear stiffnesses (force over displacement) of the two contacting entities (ball to ball or ball to wall). The contact stiffnesses at a contact can be computed assuming the stiffnesses of the two contacting entities act in series.

The slip model is an intrinsic property of the two entities. It is defined by the dimensionless friction coefficient at the contact ($\mu$). Slip is allow to occur if shear contact force exceeds the maximum allowable value.

PFC–3D provides the facility of bonding spheres together to form a 'block' and by specifying different strengths and stiffnesses of bonds the block can deform or break if the stress acting on the bonds is too high.

There are two types of bond that can be modelled: contact bond and parallel bond. Both can be envisioned as a kind of elastic spring joining two spheres together. A contact bond acts only at the contact point and can only transmit a force, while a parallel bond has finite size, acts over a circular cross section lying between two spheres and both force and moment can be transmitted through it. Both types of bond can be given a strength

which would lead to bond breakage if exceeded.

The bonding feature gives PFC–3D the capability of modelling non-spherical particles with complicated intra particle deformations. One drawback is the need for a larger computer capacity if the same resolution is to be retained as one particle is now modelled by several spheres.

### 3.2.2 Basic calculation procedure

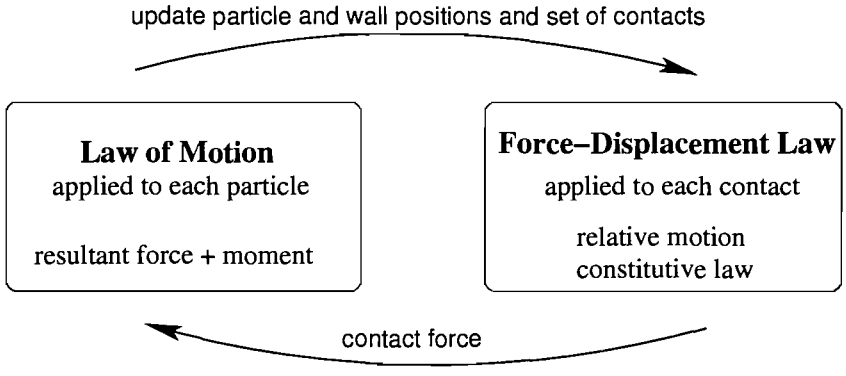


Figure 3.1: Illustration of the calculations performed by PFC–3D in one time step (Itasca Consulting Group Inc., 1997)

Figure 3.1 shows the calculation cycle in PFC–3D . At the start of each time-step the contacts are updated from the known sphere and wall positions, the force-displacement law is then applied to each contact to update the contact forces due to the relative motion between the two objects at the contact and the contact constitutive model. Next, Newton's second law is applied to each particle to update its velocity and position based on the resultant forces and moment arising from the contact force or any other body forces. The wall positions are updated based on the user specification. These procedures by default are treated as a dynamic process which is numerically represented by a time-stepping algorithm, with the velocities and accelerations are assumed constant within each time-step. The time-step should be sufficiently

small that disturbances can not propagate from any sphere further than its immediate neighbours.

For the one dimensional motion of a single mass acted on by a varying force $F(t)$, Newton's second law determines the translational and rotational accelerations as

$$\ddot{x}(t) = \frac{F}{m} \tag{3.2}$$

$$\ddot{u}(t) = \frac{M}{I} \tag{3.3}$$

where $x$ is displacement, $u$ is rotation about the centre, $t$ is time, $m$ is mass, $M$ and $I$ are moment and moment of inertia, respectively.

The following expressions describe the translational and the rotational velocities at a half-timestep point

$$\dot{x}(t + \Delta t/2) = \dot{x}(t - \Delta t/2) + \ddot{x}(t)\Delta t \tag{3.4}$$

$$\dot{u}(t + \Delta t/2) = \dot{u}(t - \Delta t/2) + \ddot{u}(t)\Delta t \tag{3.5}$$

Thus, the position and the rotation at a half-timestep point can then be expressed as

$$x(t + \Delta t) = x(t) + \dot{x}(t + \Delta t/2)\Delta t \tag{3.6}$$

$$u(t + \Delta t) = u(t) + \dot{u}(t + \Delta t/2)\Delta t \tag{3.7}$$

The calculation for the law of motion can be summarised as follows. Given the values of $\dot{x}(t - \Delta t/2)$, $\dot{u}(t - \Delta t/2)$, $x(t)$, $F(t)$ and $M(t)$, the equations mentioned above can be used to obtain $\dot{x}(t + \Delta t/2), \dot{u}(t + \Delta t/2), x(t + \Delta t)$ and $u(t + \Delta t)$. The value of $F(t + \Delta t)$ and $M(t + \Delta t)$, which will be used in the next cycle, are obtained by application of the force-displacement law.

The contact force $F$ at each contact can be resolved into normal and shear components: $F^n$ and $F^s$. The normal contact force may be calculated by

$$F^n = K^n U^n \tag{3.8}$$

where $K^n$ is the normal stiffness at the contact, $U^n$ is the overlapping in the normal direction at the contact point.

$F^s$ is calculated in an incremental fashion. The total shearforce is initialised to zero when the contact is established. An increment of elastic shear force resulted from each subsequent relative shear-displacement increment will be added to the current value. The motion of the contact must also be considered.

$$F^s = (F^s)_{rot} - k^s V^s \Delta t \tag{3.9}$$

where $(F^s)_{rot}$ is the force resulted from the rotations of the two contacting entities (calculated from change of contact direction and average angular velocity), $V^s$ is the shear component of the relative velocity at contact, and $k^s$ is the shear stiffness (tangent modulus). $F^s$ needs to be updated to account for contact motion–rotation about the line common to the old and new contact planes, and about the new normal direction.

# Chapter 4

# Numerical simulations of granular material using spheres

## 4.1 Introduction

The strength and deformation properties of granular material are of importance in many engineering problems. Non-interlocking cohesionless granular materials support shearing load through frictional contacts. If friction is absent, the mass of such a material would behave more like an inviscid fluid. It is generally accepted that the shearing resistance of such material would increase with the interparticle friction angle, and sliding is assumed to be the dominant form of particle displacement (e.g. Bishop, 1954; Newland and Allely, 1957; Rowe, 1962; Horne, 1969). However, there is evidence (Roscoe and Schofield, 1964; Oda and Konishi, 1974) suggesting that significant particle rotation also takes place during deformation.

In order to understand the effects of particle rotation on the deformation of an assemblage of spheres, particularly in relative to the initial density and the interparticle friction angle, a series of 3-D numerical simulations of

standard direct shearbox tests using a commercial code, PFC–3D (Itasca Consulting Group Inc., 1997) have been carried out. The main purposes of the work presented in this chapter are

1. To compare the results of numerical simulations and of laboratory tests on particulate material comprising spheres.

2. To investigate the effects of the initial density of packing of an assemblage of spheres on the shearing resistance and dilational behaviour.

3. To investigate the effects of interparticle friction on the shearing resistance and dilational behaviour.

4. To understand the limitations of simulating granular materials, either numerically or practically, using spheres.

## 4.2 Modelling procedure

The modelled sample, 20 $mm$ thick, was placed inside a simulated split box of internal dimensions 60 $mm \times 60$ $mm$. The vertical loading stress was applied through a platen simulated by two layers of spheres which are bonded together. The top layer consisted of rigidly bonded large spheres to increase the stiffness of the loading platen. Each sphere in the lower layer was subjected to the same downward force to provide an initial uniform stress. The loading platen was very stiff, but free to move up or down as a rigid body during compression and shearing. A platen comprising a further layer of bonded spheres was placed below the sample, and two horizontal wings were attached to the upper and lower halves of the box (Figure 4.1 and Figure 4.2), so the particles could not escape from the box during shear.

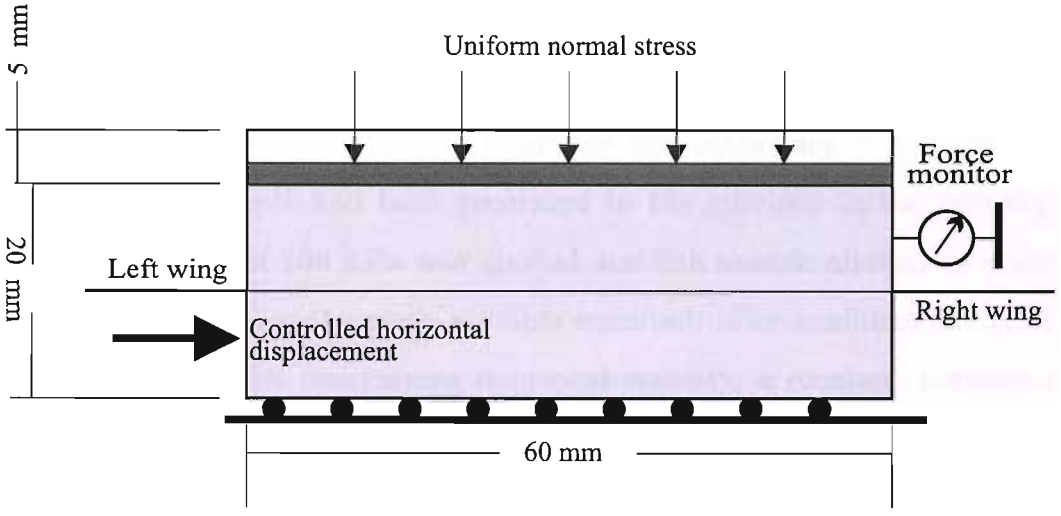


Figure 4.1: Schematic illustration of the shear box

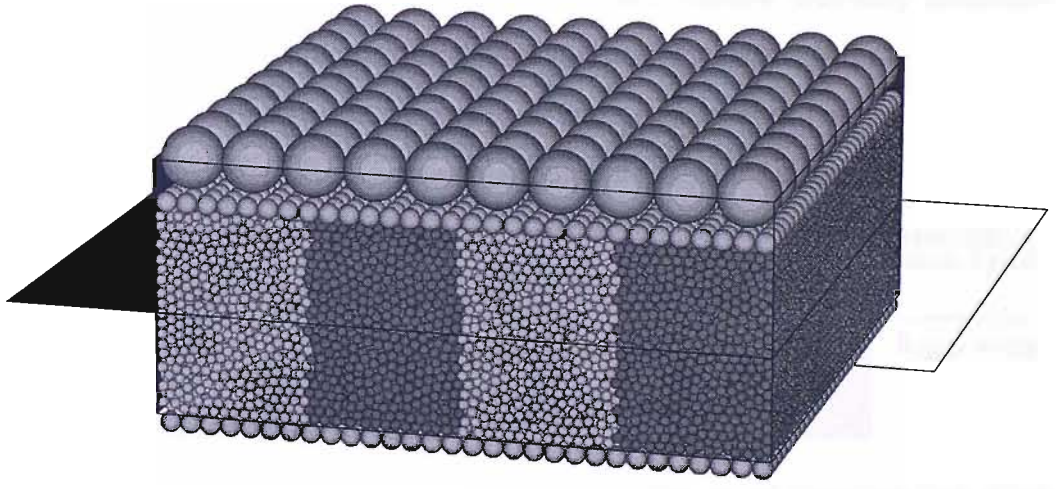

Figure 4.2: The numerical shearbox and a typical sample comprised of $1mm$ spheres

Each sample comprised approximately eighty two thousand 1 $mm$ spheres. The actual number might vary, depending on the required initial porosity, by a few thousand on either side. The spheres were initially generated with very small radii at random positions in the simulated shearbox and then gradually increased to the required size. The sample was allowed to settle (no presented excessive contact force) between each increase of sphere size.

The numerical test was carried out by shearing the two halves of a sample relative to each other by moving the lower half of the box and the bottom platen horizontally while the upper half was kept stationary.

After the sample had been generated to the specified initial porosity, a vertical stress of 100 $kPa$ was applied and the sample allowed to come into equilibrium (i.e. to reach a stable condition after confinement) prior to shearing. Whilst maintaining numerical stability, a constant horizontal velocity of $2.5 \times 10^{-5}$ $mm$ per calculation step was then applied to the lower half of the shearbox until a horizontal displacement of 10 $mm$ was achieved. For the simulations reported in this thesis, the normal and shear stiffness of all the spheres and walls were set to $10^8$ $N/m$ to ensure that only minimum overlapping is occurring at ball–ball or ball–wall contacts.

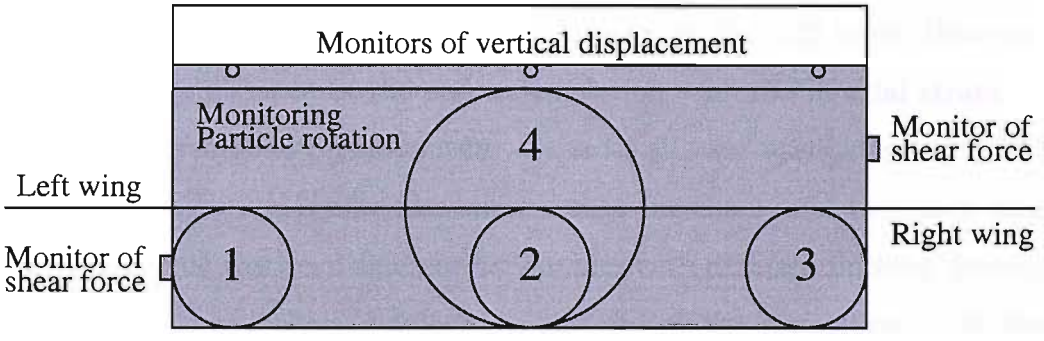


Figure 4.3: Monitoring system used in the simulations of shearbox test using 1 $mm$ spheres

The shear force on the side walls and displacement at various locations on loading platen were monitored during shearing. Changes in porosity and stress were tracked in the specified zones 1 to 4. A group of spheres fitting in a vertical section stretching from left to right end through middle of sample (lightly shaded area) was selected and their rotations calculated (Figure 4.3).

## 4.3 Effects of different initial porosity

Simulations of four samples with different initial porosities were carried out. The initial porosities used were 37.5%, 40.3%, 41.5% and 43.1% covering the range of porosities that could be practically achieved under a normal loading of 100 $kPa$ with an interparticle friction angle of 30°, which is close to the friction angle of quartz materials.

Figure 4.4 shows the results of four simulations in terms of the bulk angle of shearing resistance and void ratio against relative shear displacement. The bulk angle of shearing resistance $\phi'$ was defined as $\phi' = \tan^{-1}(\tau/\sigma')$, where $\tau/\sigma'$ is the ratio of shear to normal effective stress applied to the sample.

The peak angle of shearing resistance varied from 23° for the densest sample to 13° for the loosest. The corresponding range of shear strain at peak strength was between 1.8% (1.11 $mm$) and 10.4% (6.22 $mm$). However, the shearing resistance at the end of simulation – at 16.7% axial strain, or 10 $mm$ relative shear displacement – was in all case approximately 12.5° (Figure 4.4(a)). The results also showed that the changes of the voids ratio during shearing was very different for samples with different packing density. All samples then behave similarly to the end of the simulation . At the early stage of shearing the voids ratios of the two loose samples decreased for the first 3 $mm$ of relative shear displacement (5% shear strain) and then started to increase until their peak strengths were reached. For the two dense samples, void ratios increased continuously during shearing. In all cases, the void ratios varied very slowly during latter stage of shearing (after 7 $mm$) until the final void ratio of about 0.72 was reached. Figure 4.4(b) also shows that the peak strength is associated with sample dilation. For the densest sample, the dilation angle at peak strength was nearly 16° compared with 3.5° for the loosest. Starting with different densities of packing and at the

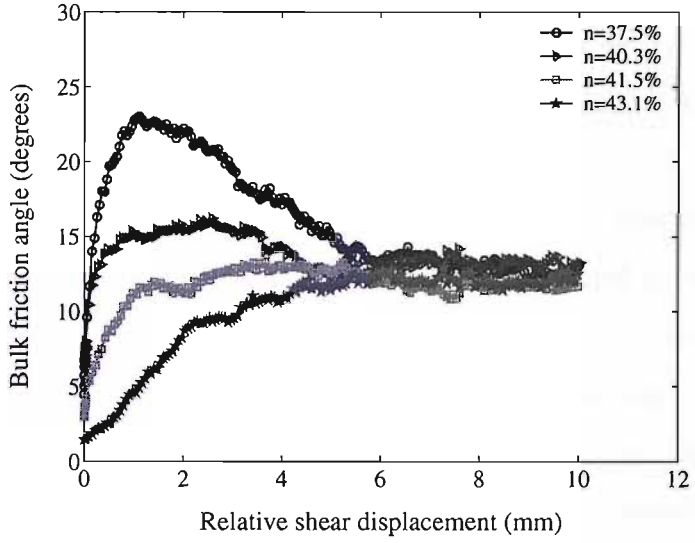


(a) Bulk friction angle

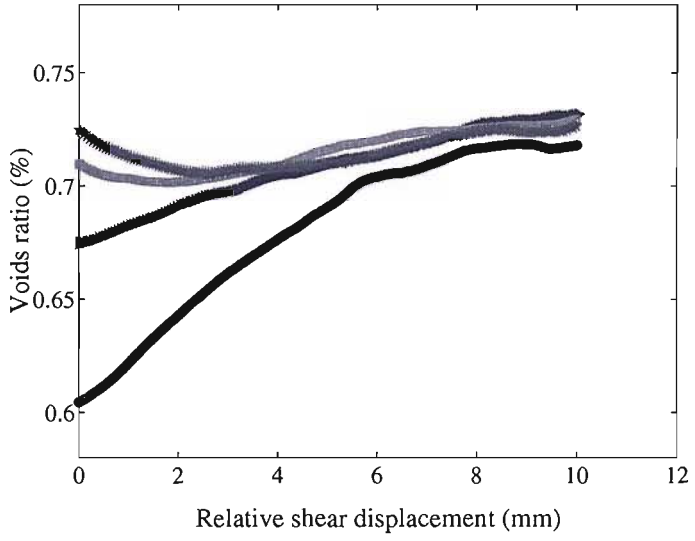


(b) Void ratio

Figure 4.4: Stress-strain behaviour and change of void ratio of samples with different initial porosity. Numerical samples consisted of 1 $mm$ balls having $\phi_\mu = 30°$ were tested at normal stress of 100 $kPa$.

same value of $\sigma'$, these simulations reached a final state within a narrow band at which the dilation rate of all simulations was very low but still not completely levelled off, the 2° dilation angle indicating that critical states were very close but had not yet been reached.

Roscoe et al. (1958) and Wroth (1958) pointed out that the measured shear stress $\tau$ could be split into two components $\tau_e$ and $\tau_i$, where $\tau_e$ was that part of the shear stress which would be just sufficient to provide the energy used by the soil sample in changing its volume against the confining pressure, and the reminder $\tau_i$ was that which provides the work absorbed internally by the sample. With the convention that $\tau_e$ is positive when the sample is expanding and negative when contracting, it always holds that

$$\tau = \tau_e + \tau_i \tag{4.1}$$

For a shearbox:

$$\tau_e = \sigma' \frac{dy}{dx} \tag{4.2}$$

where $y$ and $x$ are the sample thickness and relative shear displacement (relative displacement of shearbox halves) respectively.

In Figure 4.5, the internal shearing resistance, calculated according to $\tau_i$, is seen to be practically constant for all but the initial stage of the simulation. A difference about 2° at the end of the shearing between two curves confirms that volume change has not ceased and that the sample is still dilating slightly. The critical state angle of shearing resistance can be estimated by subtracting the dilation angle (about 2°) from the final angle of shearing resistance (12.5°). This corrected value of $\phi'_{cv}$ is very close to the internal shearing resistance calculated from $\tau_i$, which keeps the sample deforming without volume change. A similar observation was made from tests using

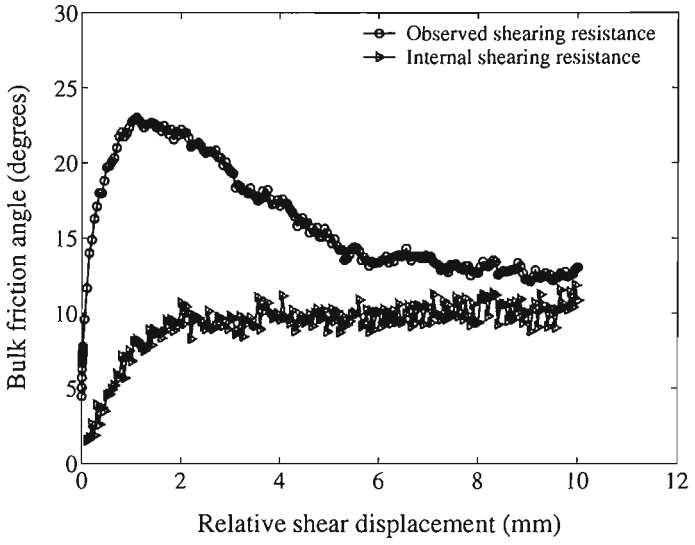


Figure 4.5: Observed and corrected shearing resistance curves for shearbox test simulation using 1 $mm$ spheres, $\sigma' = 100kPa$

steel balls (Roscoe et al., 1958).

## 4.4 Interparticle friction angle

It is generally believed that the deformation behaviour of a soil is significantly affected by interparticle friction (e.g. Lee and Seed, 1967; Schanz and Vermeer, 1996). However, the relationship between interparticle friction and shear resistance of an assemblage of spheres is still unclear.

Four samples with different interparticle friction angles ($\phi_\mu$) of 5°, 15°, 30° and 45° were used to investigate the effect of this property on the overall stress-strain behaviour. This range of $\phi_\mu$ covers a wide variety of materials from steel to feldspar, and of glass ballotini under various loading and surface conditions (Skinner, 1969; Procter and Barton, 1974). The samples used in the numerical simulations had the same initial porosity of 37.5% and were sheared under a normal stress of 100 $kPa$.

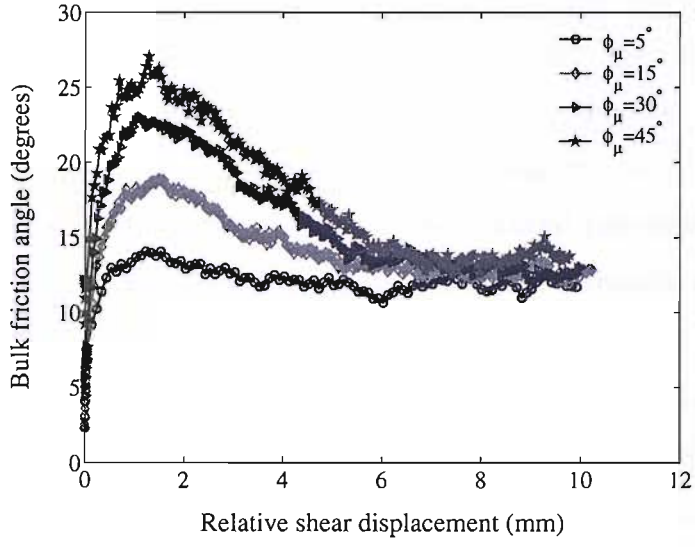


(a) Bulk friction angle

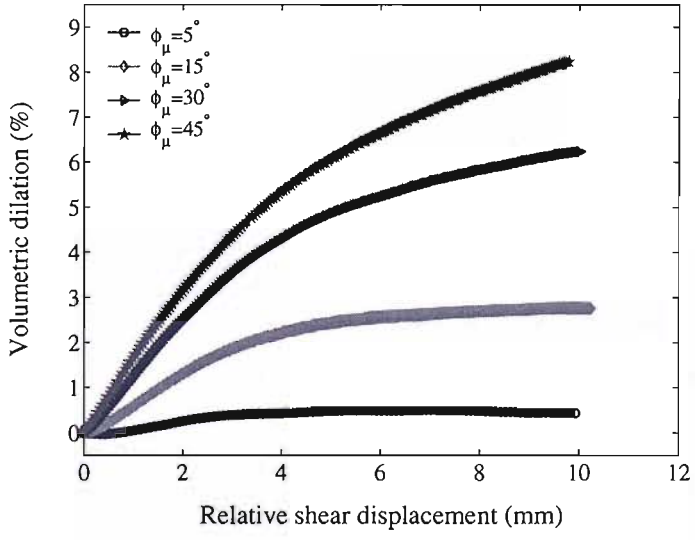


(b) Volumetric dilation

Figure 4.6: Stress-strain behaviour and volumetric dilation of samples with different interparticle friction angle $\phi_\mu$. Numerical samples consisted of 1 $mm$ balls were tested at normal stress of 100 $kPa$ with initial porosity of 37.5%.

Figure 4.6 shows that interparticle friction had a large effect on the peak angle of shearing resistance, as well as on the maximum dilation rate and the overall sample volumetric dilation at the end of shear. However, the shearing resistance at the end of shear was within a small range in the vicinity of 12.5° in all cases, as with the samples with different initial porosities. Although the samples had not quite reached critical states, this strongly suggests that the shearing resistance at the critical state $\phi'_{cv}$ would not be significantly affected by the interparticle friction of spheres. Figure 4.6(b) also shows that the overall volumetric dilation was larger for samples with a higher $\phi_\mu$ than for samples with a lower $\phi_\mu$. The dilation rate at the end of shear was also significantly higher at 3.6° for the sample with $\phi_\mu = 45°$ compared with 0° for the sample with $\phi_\mu = 5°$, suggesting that might be harder for an assemblage which consists of particles with a higher $\phi_\mu$ to reach a critical state.

The shearing resistance at the end of the simulations shown in Figure 4.6(a) seems to be in contradiction to general belief and theoretical work based on the assumption of pure sliding ball-to-ball contact such as by Horne (1969). However, Figure 4.7 shows that $\phi'_{cv}$ for spherical particles, either from laboratory tests on spheres of different materials or from numerical simulations (note: values for numerical simulations are corrected by subtracting dilation angle from shearing resistance at the end of test), is not significantly affected by changing $\phi_\mu$. Neither the experimental nor the numerical data follow the theoretical curve either. The difference between actual values of the two groups is believed to result from assumptions made in numerical model. For real material, e.g., glass ballotini, it is impossible to ensure that each particle is perfectly spherical and absolutely the same size, in contrast with the numerical simulations. Also, the particle surface conditions, which are in

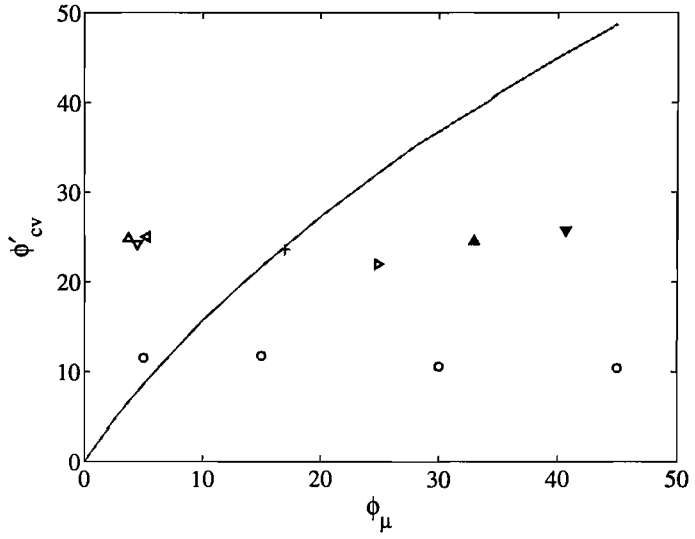


Figure 4.7: $\phi'_{cv}$ of spherical particles plotted against $\phi_\mu$ and compared with the theoretical curves of Horne (1969). ○: numerical simulations using $1mm$ spheres; Triangles are shearbox tests after Skinner (1969). △: $1mm$ glass ballotini (dry); ▽: $3mm$ glass ballotini (dry); ◁: $3mm$ lead shot (dry); ▷: 1/8 inch steel ball (dry); ▲: $1mm$ glass ballotini (flooded); ▼: $3mm$ glass ballotini (flooded); +: $0.25mm$ glass ballotini (Rowe, 1962)

reality complex and hard to quantify, are somewhat simplified in numerical simulations. The idealised particles produced in a numerical simulation lead to lower overall sample strength. If this argument is correct, changes in $\phi'_{cv}$ might be more affected by particle shape and size, and even small differences in these two properties from perfect uni-sized spheres would lead to higher value of $\phi'_{cv}$. More research is needed to investigate how particle shape and size variation would affect the overall stress-dilation behaviour of a sample.

It is remarkable that an assemblage of particles having $\phi_\mu = 5°$ exhibits a shearing resistance of over $10°$, or even higher at about $26°$ for the tests in which glass ballotini were used (Skinner, 1969), in the absence of volume change. What caused these results is still open to debate. The deviation from Horne's theoretical prediction, which is based on a pure frictional model

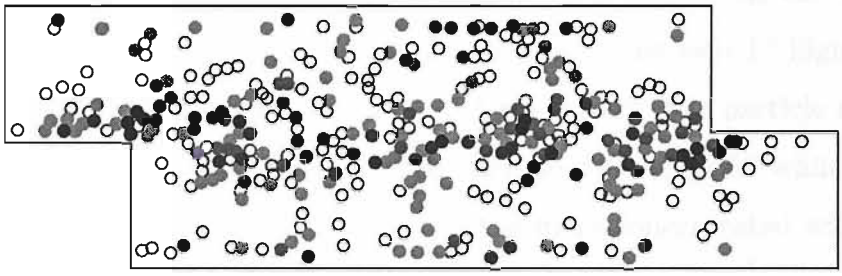

(a) $\phi_\mu = 5°$

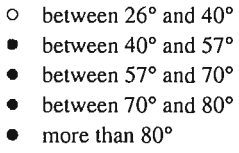


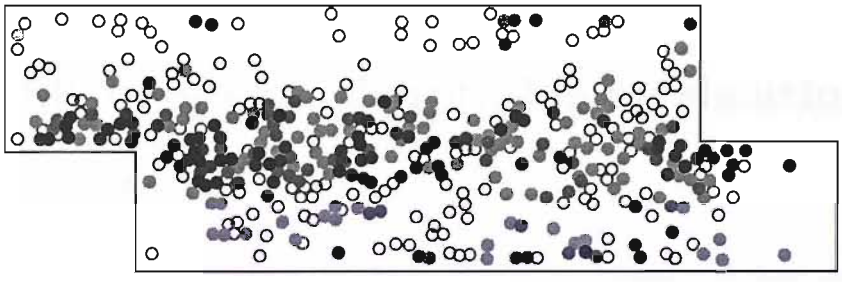

(b) $\phi_\mu = 30°$

Figure 4.8: Particle rotation. The numerical samples consisted of 1 $mm$ spheres with $\phi_\mu = 5°$ and $\phi_\mu = 30°$ respectively. Normal stress of 100 $kPa$ and initial porosity of 37.5% were used.

with no particle rotation, suggests that mechanism other than pure sliding was also controlling the movements of the spheres. One possible explanation is that particle rolling as well as sliding plays an important role in deforming the sample, especially when $\phi_\mu$ is high.

Figure 4.8 shows a larger proportion of particle rotations greater than 70° (those darker shades) in the simulation with particles having $\phi_\mu = 30°$ (Figure 4.8(b)) than for the simulation with $\phi_\mu = 5°$. However, both sam-

ples show a substantially similar average particle rotation: at the value of about 24.6° for the high friction particles, it is only just over 1° higher than that (23.4°) for the $\phi_\mu = 5°$ test. Figure 4.8(a) shows that particle rotation was more evenly distributed all over the sample with $\phi_\mu = 5°$ while in Figure 4.8(b) for the sample with $\phi_\mu = 30°$ it is more concentrated within the middle band.

When $\phi_\mu$ is high, particles are supposed to roll over rather than slide against other particles resulting in higher dilation than sliding (Skinner, 1969). Figure 4.6(b) seems to support this idea as the volumetric dilation of 8.5% at 16.7% shear strain for the sample with $\phi_\mu = 45°$ is almost 12 times that of the sample with $\phi_\mu = 5°$.

## 4.5 Effect of particle rotation on shearing resistance

The movement of cohesionless granular material in a shear test does not result either pure sliding or pure rolling, even for perfect spheres in a numerical simulation. Previous researcher in the past (e.g. Skinner, 1969; Bishop, 1971; Oda et al., 1982), together with the numerical simulations using 1 *mm* spheres described above, have suggested that particle rotation is an important, even overriding factor in the stress-strain behaviour of assemblage of such particles.

There are two extreme cases for the movement of a particle

1. The particles have complete freedom to spin if the particle is perfectly spherical, and particle deformation and the surface damage (if there is any) have no effect on particle movement. It is assumed that an assemblage of such particles will produce the lowest shearing resistance and highest particle rotation.

2. The particles have no freedom to spin and can move by sliding only. No breakage of any sort occurs. In this circumstance, the angular velocity ($\omega$) of this ideal particle is zero and an assemblage of such particles will produce the highest shearing resistance in a shear test.

In reality, the movement of particles, and therefore the shearing resistance, should fall somewhere between the two.

Five shearbox test simulations with different restraints on the angular velocity of particles were carried out to investigate the relationship between the shearing resistance and particle rotation. Different sized spheres, of which size distribution will be discussed in more details in next chapter, were used instead of uniform 1 $mm$ spheres, since the results from previous simulations also suggested that variation in particle size would affect a sample's shearing resistance. The sample with different sized particles consisted of 30000 spheres and had a lower initial porosity of about 32% which is also close to its practical maximum packing density. an interparticle friction angle $\phi_\mu = 30°$ was used and samples were tested under a normal stress of 100 $kPa$.

Figure 4.9 shows that the shearing resistance increases with the decrease of angular velocity $\omega$ . Compared with that of the sample with free spheres, the bulk friction angle increased slightly when the restraint on maximum permissible $\omega$ was as high as $1 \times 10^{-4}$ $rad/step$. When the maximum permissible angular velocity was lowered to $1 \times 10^{-6}$ $rad/step$, on the other hand, the peak shearing resistance was almost doubled from 36° to 65° and was approaching the value for the sample with 'slide only' spheres. AS similar trend could be seen for the shearing resistance at the end of shearing. Varying particle size also had a dramatic effect on sample's strength. The shearing resistance for sample consisted of 1 $mm$ spheres, both at peak and end of test, were only about half of those shown by sample with non-uniform

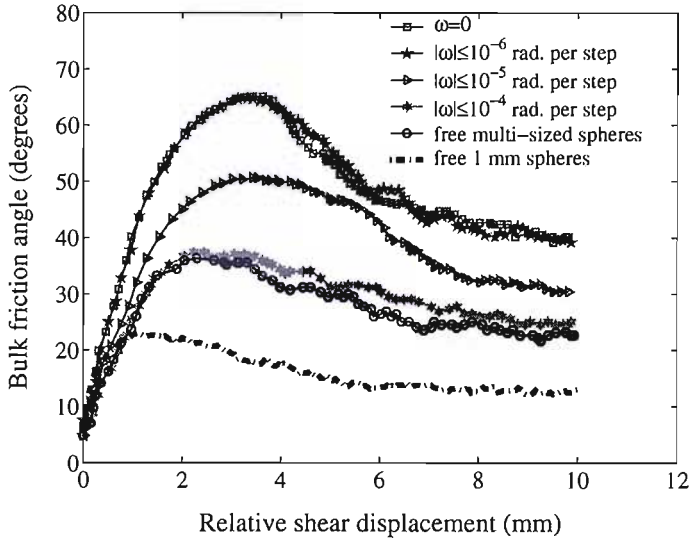


Figure 4.9: Difference of shearing resistance of the samples with different restraints of particle angular velocity. Samples consisted of spheres with $\phi_\mu = 30°$. Normal stress $\sigma' = 100kPa$

sized spheres, despite they have the same other particle properties.

The results clearly demonstrated the correlation between shearing resistance and particle rotation. For real granular materials, e.g. sand, the particles hardly can be perfectly smooth and spherical and therefore the movements of particles during shear, unlike those of spheres, must be restrained by geometry. It can be assumed that the strength will be lower than if all particles are not allowed to spin, and higher than if all particles are free to rotate. By carefully choosing particle properties such as $\phi_\mu$ and size distribution, simulating an assemblage of spheres with restricted rotation provides a way of predicting a possible range of strengths of certain granular material, given that the material has no interlocking and no particle damage will occur.

## 4.6 Summary

The effects of packing density and the micro-properties of an assemblage of spheres on its shear behaviour have been investigated by numerical simulations of a direct shearbox test. The stress-strain behaviour and shear strength were examined for four different initial porosities, four different interparticle friction angles and different degrees of particle restraint against rotation under a common normal stress of $100kPa$. Particle rotations within the samples were discussed within the context of interparticle friction.

The densest sample showed a significant peak angle of shearing resistance and a high volumetric dilation compared with looser samples. The very loose sample suffered a volume reduction at the beginning of shearing and then gradually dilated towards the critical volume. All samples reached almost the same angle of shearing resistance of 12.5° and void ratio of 0.72 at the end of shear, although the critical state had not quite been achieved. However, $\phi'_{cv}$ can be estimated by subtracting dilation angle from angle of shearing resistance at the end of test, as suggested by Roscoe et al. (1958).

The peak angle of shearing resistance increased by 13° and the volumetric dilation of the sample by a factor of nearly 12 when $\phi_\mu$ increased from 5° to 45°. This indicates that the $\phi_\mu$ makes an important contribution to the dilation of sample and to the angle of shearing resistance when sample starts to dilate.

The results from the numerical simulations showed the same trends as those from laboratory tests (Skinner, 1969): the shear resistance at the critical state ($\phi'_{cv}$) was independent of the initial porosity and interparticle friction angle of spheres. This was different from a theoretical relation (Horne, 1969) between shearing resistance and interparticle friction which was based on a mechanism of pure sliding and without particle rotation and which predicted

an increase of $\phi'_{cv}$ with interparticle friction angle.

In a series of simulations, the degree of rotation of the spheres was restrained, and resulted in increased $\phi'_{cv}$ with the reduced degree of particle rotation. For a given interparticle friction angle, the spheres that were free to rotation had the lowest $\phi'_{cv}$, and the spheres that were prevented from rotating had the highest $\phi'_{cv}$. An non-interlocking granular material should have a $\phi'_{cv}$ between these two values because some degree of rotation will occur between granular particles during shearing.

For spheres that were free to rotate, a sample comprising a variety of particle sizes had a higher $\phi'_{cv}$ than a sample comprising uniform sized spheres, which suggests that the distribution of particle size might be an important factor in the shear resistance of an assemblage of particles. This might be due to the lower porosity and more contact points of a sample comprising a variety of particle sizes than of an assemblage with uniform sized particles.

Results from numerical simulations using samples made up of spheres with only restricted rotation suggest that a shearing resistance close to that of real material can be achieved by manipulating the particles' maximum angular velocity. However this procedure cannot be linked to any measurable property of a real granular material.

# Chapter 5

# Numerical simulation of direct shearbox test

## 5.1 Introduction

Perhaps the main problem arising from the use of circular discs (in 2-D) or spheres (in 3-D) in numerical simulations (or even in physical experiments) is the excessive freedom of the particles to rotate compared with real soils. This affects both the dilation that takes place during deformation and the shear strength of the soil (e.g. Bardet and Proubet, 1991; Mitchell, 1993; Oda and Kazama, 1998; Rothenburg and Bathurst, 1992; Thornton, 2000). Various attempts have been made to address this by constraining the rotation of individual particles (Ng and Dobry, 1992; Iwashita and Oda, 1998) or by using non-spherical/non-circular particles, typically ellipsoids (Ting et al., 1993; Lin and Ng, 1997) or clusters of bonded discs/spheres (Thomas and Bray, 1999).

Iwashita and Oda (1998) reported that higher peak shear strengths and clearer void localisations were observed when the freedom of particles to

rotate was constrained than in simulations in which the particles were free to roll. This was also observed in three-dimensional numerical simulations of direct shear tests reported in Chapter 4: the shear strength of a sample was found to depend on the degree to which particle rotation was constrained (i.e. the sample in which particle rotation was prevented had the highest shear strength, while the sample in which particles were allowed to rotate freely had the lowest). However, constraining particle rotation is not satisfactory because the degree of constraint is not a parameter that can be related easily or directly to the physical properties of real particles.

A more satisfactory approach is to use non-circular/non-spherical particles to simulate the non-sphericity of real particles. Ting et al. (1993) used ellipses and Lin and Ng (1997) used 420 ellipsoids to demonstrate that particle shape had a significant effect on sample strength and internal fabric. Thomas and Bray (1999) used 468 clusters of bonded disks to investigate shearing resistance and particle rotation in 2-D simulations of biaxial tests. All of these studies demonstrated that a sample consisting of non-circular/non-spherical particles can more closely represent the deformation behaviour of real soil than a sample made up of discs or spheres.

This chapter presents the results of a series of numerical simulations of standard direct shearbox tests on assemblages of particles using PFC–3D (Itasca Consulting Group Inc., 1997). Non-spherical granular particles were simulated by means of pairs of strongly bonded spheres to give particles of different shapes. The numerical samples replicated the relative particle size distribution of a medium Leighton Buzzard sand (Figure 5.1), with the actual size range multiplied by a certain factor so that the specified number of particles filled the standard shear box at the desired porosity. The effect of the micro properties of the particles (particle shape, particle size

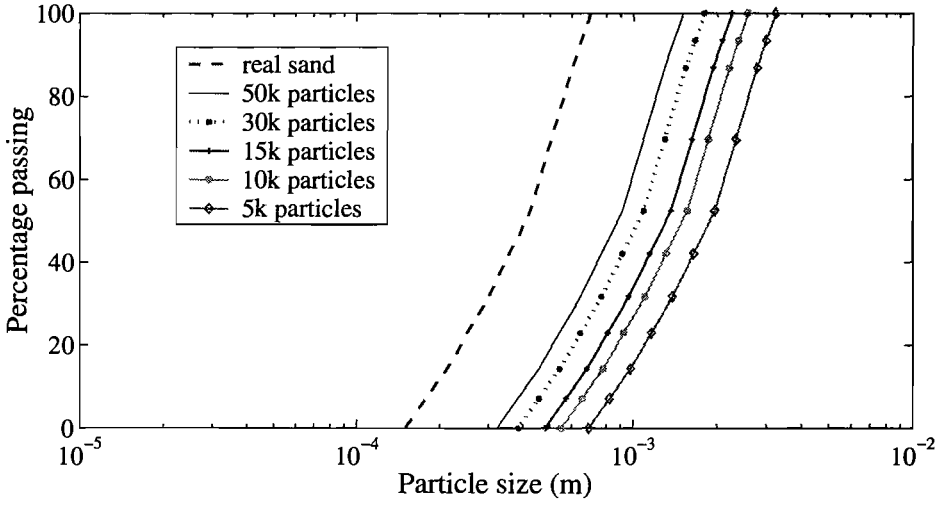


Figure 5.1: Particle size distribution of numerical samples and reference real sand.

and interparticle friction angle) on the overall stress-strain behaviour of the sample, on the micro-mechanisms controlling deformation and failure have been investigated. The main purposes of the work are

1. To investigate the effects of the particle shape on the shearing resistance and dilational behaviour.

2. To investigate the effects of particle properties such as particle size and interparticle friction on the shearing resistance and dilational behaviour.

3. To compare the results of numerical simulations and of laboratory tests on particulate materials with the similar particle size distribution.

4. To explore the mechanism of deformation within shear zone.

## 5.2 Modelling procedure

Each particle was formed by bonding two spheres together, as shown in Figure 5.2.

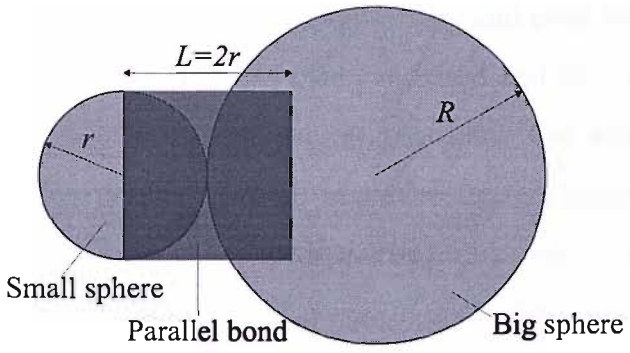


Figure 5.2: Schematic illustration of a bonded particle. The length and width of the parallel bond are the same as the diameter of the smaller sphere.

The bond can be imagined to act as a column of elastic glue between the two spheres and its strength and stiffness adjusted as required. A force and a moment will develop within the bond as a result of the relative motion at the contact and the bond stiffness. In principle, the bond strength and stiffness can be varied to simulate different deformation behaviour, such as crushing, within the particle. However, in this study, the strength and stiffness of bond were chosen to be high enough so that the bonds would not break and no significant deformation would occur within a single particle. In other words, each pair of spheres behaved as a single rigid particle.

The overall shape of a particle was characterized by a shape factor defined as $(R+r)/R$, where $R$ and $r$ are the radii of the larger and smaller spheres respectively. A spherical particle has a shape factor of 1 and a particle comprising two spheres of the same size has a shape factor of 2. In the study described in this thesis, the shape factor ranged between 1 and 2. The radius

of the bigger ball is taken as the mesh-passing size of the whole particle.

The procedure of preparing a sample consisted of bonded particles was different from that consisted of spheres. The larger spheres of each pair were first generated and expanded to the required size which could be calculated from prospected particle numbers, initial porosity and total volume of sample. The smaller spheres of each pair was then generated and attached to a random position on the surface of their respective partners. The whole sample then would be allowed to 'settle' until no excessive contact forces existed. The normal and shear stiffness of all the spheres and parallel bond were set to $10^8$ $N/m$. The geometry and construction of simulated split box, as well as the modelling procedure were described in Chapter 4

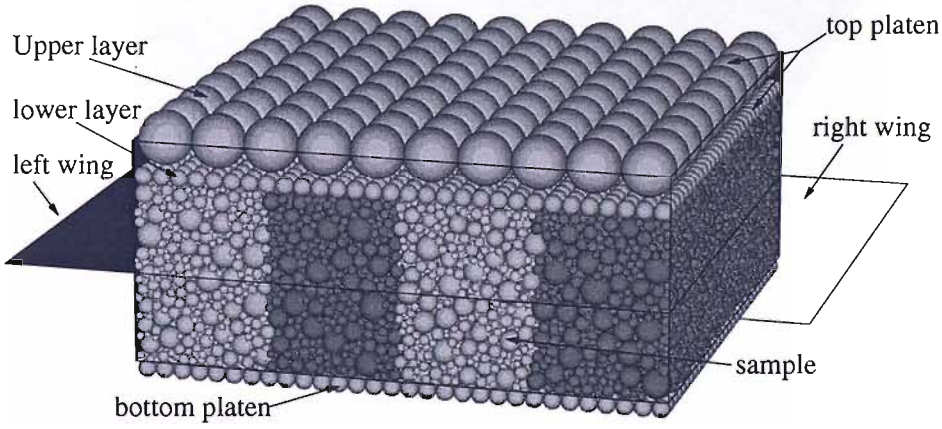


Figure 5.3: The numerical shearbox and a typical sample

Figure 5.3 shows a sample with 30000 particles of shape factor 1.3 and a porosity of 0.33. In this study, the number of particles in numerical samples using non-spherical particles ranges from 5000 to 50000. For the sample with 50000 particles the radius of the particles is about twice that of the reference real sand (Figure 5.1).

The porosity, stress and displacement at certain locations within the sam-

ple were monitored during shear. Two groups of particles, one in the middle and one close to the right edge of sample were selected, each consisting of eleven particles evenly spaced between the top and the bottom of the sample, and their displacements and rotations calculated. The shear force on and vertical displacement of the loading platens were also monitored.

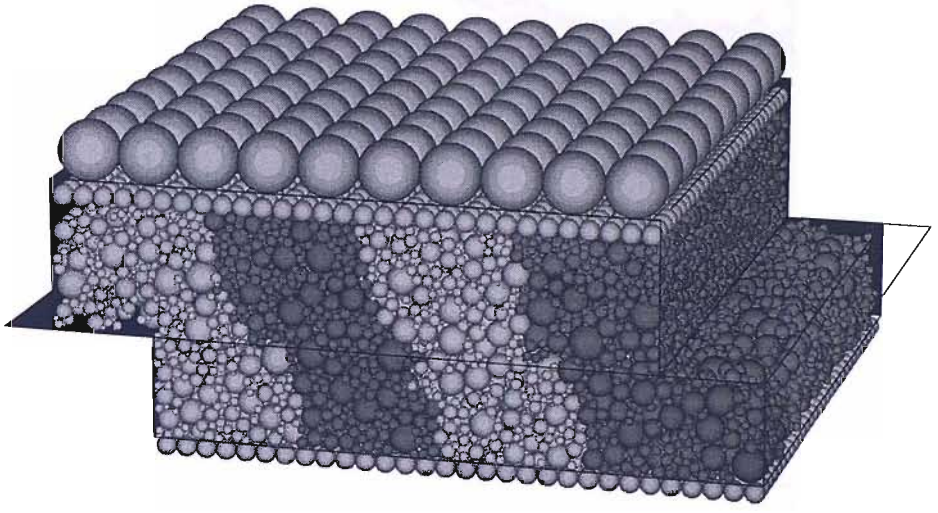

Figure 5.4: A sample after shearing

## 5.3 Sequence of analysis

After the sample had been generated to the specified initial porosity, a vertical stress was applied and the sample allowed to come into equilibrium prior to shearing. A constant horizontal velocity of $2.5 \times 10^{-5}$ $mm$ per calculation step was then applied to the lower half of the shearbox until a horizontal displacement of 10 $mm$ was achieved.

Figure 5.4 shows the maximum shear displacement of the sample in Figure 5.3 (30000 particles) under a vertical stress of 100 $kPa$: the sample stress-deformation behaviour is shown as the second sample in Figure 5.5

and also in Figure 5.6.

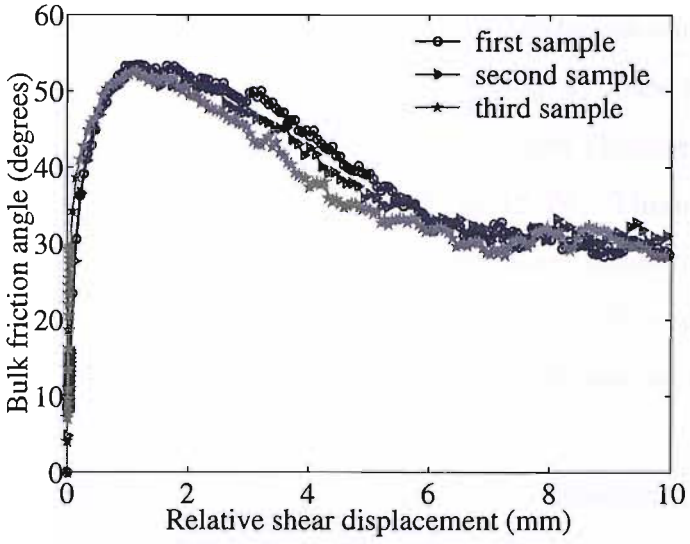


(a) Bulk friction angle

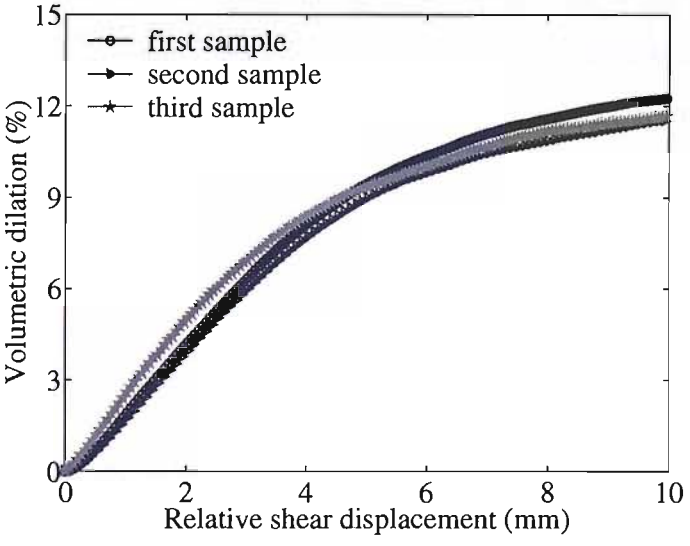


(b) Volumetric dilation

Figure 5.5: Repeatability of simulations. Three numerical samples with the same properties: 30000 particles of shape factor 1.3, $\phi_\mu = 30°$ and initial porosity of 0.33 were tested at normal stress of 100 $kPa$.

Differences in recorded deformation behaviour caused by random variations in sampling are shown in Figure 5.5. Three randomly simulated samples with the same particle properties were tested under the same conditions. The bulk angle of shearing resistance (defined in Chapter 4)varies from 51.9° to 53.3° at peak and 29.0° to 31.1° at the end of the test (Figure 5.5(a)). The overall volumetric dilation varies from 11.5% to 12.3%. These results indicate that random sampling does not produce significant differences in sample behaviour and that the simulations are repeatable. Therefore, the numerical shearbox model can be used to investigate the effect of particle properties on overall soil behaviour.

The bulk strength of a typical numerical sample reached its peak value of 53° after the sample had been sheared by about 1.4 $mm$. Following the peak value, the shear stress decreased and the stress ratio approached a constant value of approximately 31°. Dilation at this stage had all but ceased, indicating that the critical state had almost been reached. The overall volumetric dilation at a relative horizontal displacement of 10 $mm$ was 11.5% (see Figure 5.6).

A laboratory test also was carried out on a reference real sand under the same vertical stress (100 $kPa$). The real sand sample had an initial porosity of 0.37, compared with 0.33 for the numerical sample. The results are also shown in Figure 5.6. For the real sand, the peak bulk strength is smaller (47.7°) and is achieved sooner (after a relative shear displacement of 1.14 $mm$). The dilation of the numerical sample is more than three times that of the real sample. This might be because the thickness of the shear band is related to the particle size (Roscoe, 1970; Scarpelli and Wood, 1982; Oda and Kazama, 1998) and the mean particle size in the numerical model is 2.5 times greater than that of the real sand.

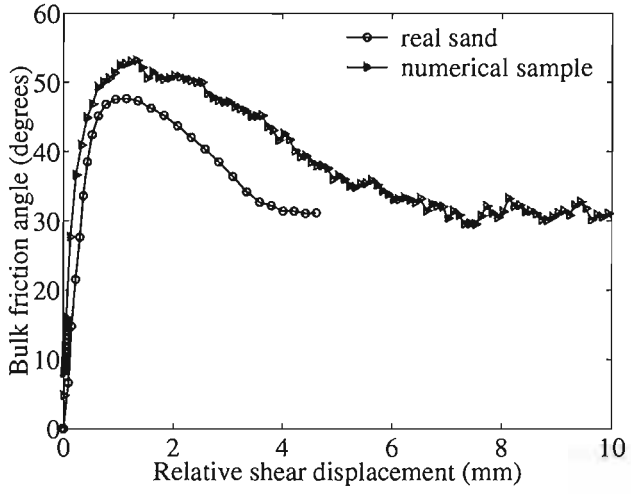


(a) Bulk friction angle

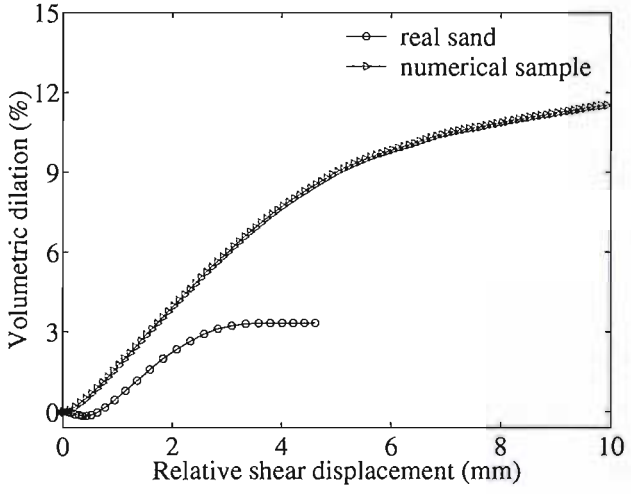


(b) Volumetric dilation

Figure 5.6: Bulk strength and volumetric dilation at normal stress of $100kPa$: numerical sample comprising 30000 particles of shape factor 1.3 and real sand.

Figure 5.6 shows that the behaviour of the numerical sample in the simulation of the shearbox test is generally similar to a real sand, although differences in actual strength and overall dilation are noticeable. It suggests

that the numerical simulation can be used to gain a better understanding of the behaviour of particle assemblages and the particle-scale mechanisms governing it. However, the numerical sample is not intended to mimic exactly the behaviour of the real sand, and the numerical simulation is not intended to replace a laboratory test.

## 5.4 Effect of number of particles

To examine the effect of the number of particles in the sample, simulations with samples comprising 5000, 10000, 15000, 30000 and 50000 particles were carried out. The sample volume and initial porosity are not varied, thus a sample comprising more particles has a smaller particle size. The smallest mean particle size used in the numerical simulations was still about 2.1 times larger than the reference real sand. In other words, a numerical sample comprising approximately 500000 particles would be needed to match the particle size of the real sand. This is beyond the resources available to the project.

Figure 5.7 shows the variation of shear strength and volumetric dilation with the number of particles. Horizontal lines indicate the bulk friction angles at the peak and the end of the tests on the real sand . The peak friction angle showed a slight decrease from 54.9° for the sample comprising 10000 particles, to 52.6° for the sample comprising 50000 particles. All of the peak strengths of the numerical samples are greater than the peak strength of the real sand. On the other hand, the friction angle at the end of simulations decreased significantly from 37.4° to 28.3° (from above to below the value for the real sand) as the number of particles was increased, as shown in Figure 5.7(a). The overall volumetric dilation also decreased

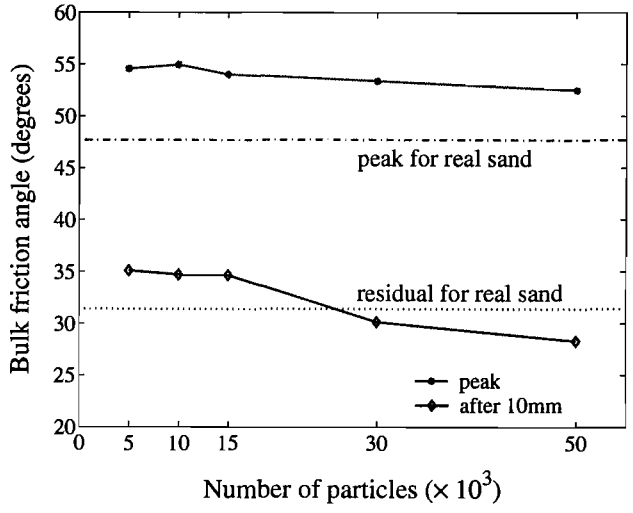


(a) Bulk friction angle against number of particles

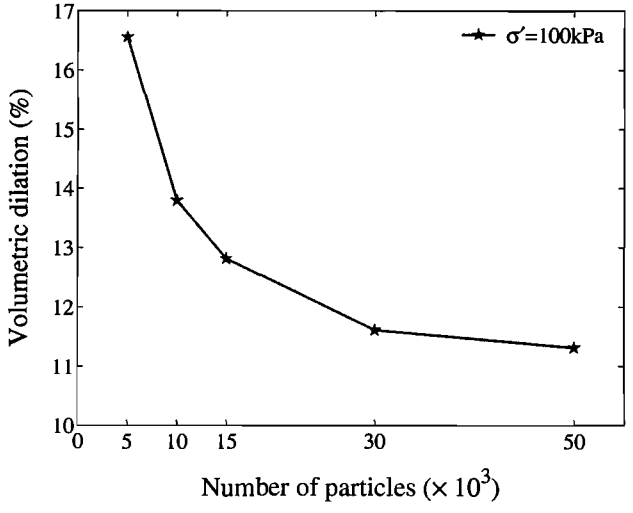


(b) Volumetric dilation against number of particles

Figure 5.7: Effect of number of particles, samples of shape factor 1.3, $\phi_\mu = 30°$ and initial porosity 0.33 at a normal stress of $100kPa$. Real sand sample had approximate $5 \times 10^5$ particles, initial porosity 0.37 and overall dilation after test was 3.3%

significantly from 16.5% to 11.8% (Figure 5.7(b)). The strength and dilation of samples generally decrease with the particle size (i.e. the number of particles is increased) in general. As discussed later, many factors (particle size, shape, density, interparticle friction angle $\phi_\mu$ etc.) control the strength-dilation behaviour of a sample, and changing any of them could alter the results. Trying to distinguish the exact reasons for the difference in detail between the results of the numerical simulations and the tests on real sand is difficult, and in any case unnecessary for the purpose of this study.

In view of the computer time taken to run an analysis with a very large number of particles, further simulations were carried out on samples comprising 30000 particles only. This is considered reasonable in view of the relatively small changes in calculated behaviour on increasing the number of particles from 30000 to 50000.

## 5.5 Effect of normal stress

Numerical simulations at normal effective stresses of $25, 50$ and $200\ kPa$ were carried out for samples comprising 30000 particles with shape factor 1.3, $\phi_\mu = 30°$ and initial porosity 0.33. The results of these analyses are shown in Figure 5.8.

The peak bulk friction angle reduces significantly with increasing normal stress, as would be expected due to the suppression of dilation. The bulk friction angle at the end of test also displayed a gradual decrease with increasing normal stress, perhaps rather more than might be expected in reality. A small error might be introduced because the critical states had not really been reached. The same type of behaviour was observed in the real sand (Figure 5.9) but to a much smaller extent. The relationship between

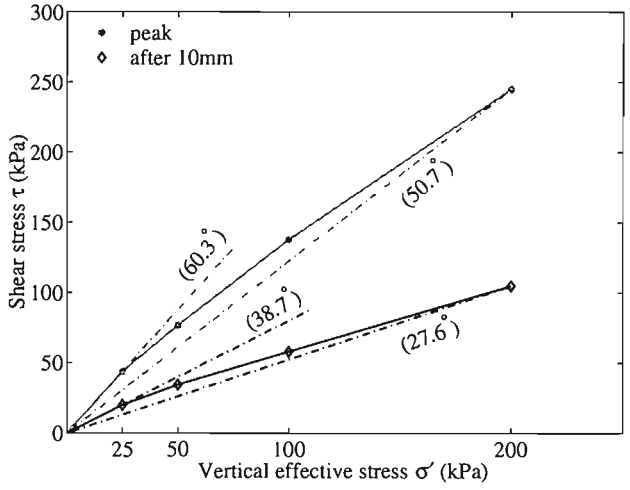


(a) Shear failure envelopes for the numerical samples

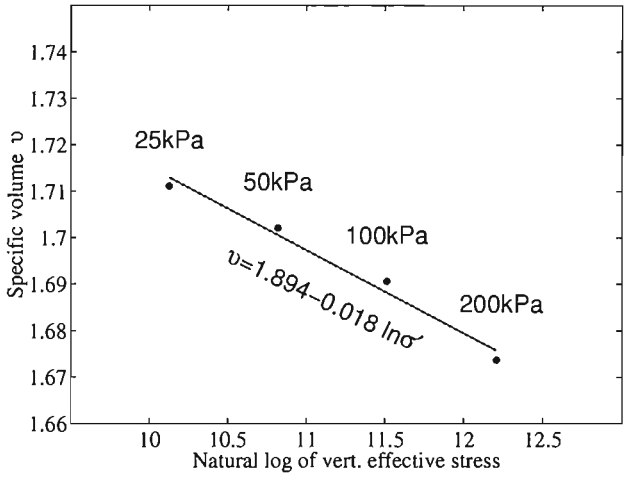


(b) Specific volume after shearing against $\ln \sigma'$

Figure 5.8: The effect of normal stress on shear strength and specific volume. The samples had 30000 particles with a shape factor of 1.3, initial porosity 0.33 and $\phi_\mu = 30°$

the normal stress and the specific volume after shearing was linear in a semi-log plot, Figure 5.8(b) for the numerical simulation and Figure 5.9(b) for

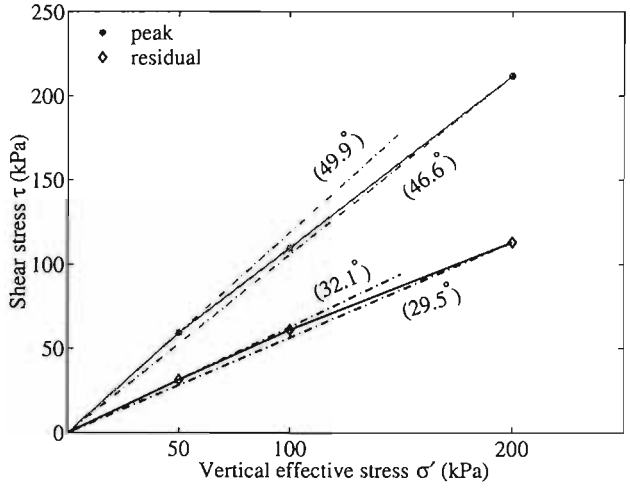


(a) Shear failure envelops of the real sand

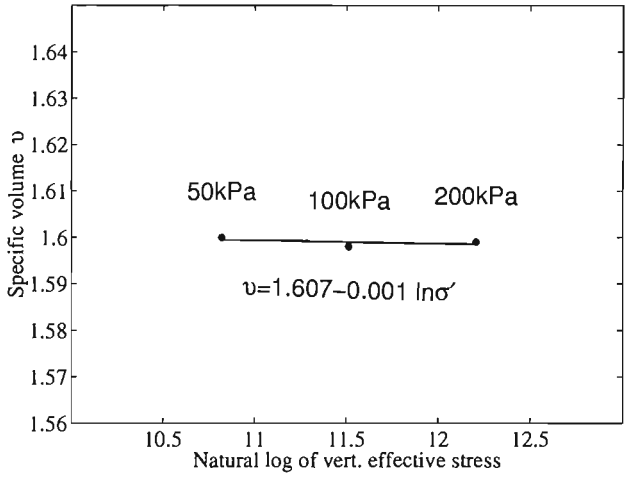


(b) Specific volume of real sand after shearing against $\ln \sigma'$

Figure 5.9: Shear strength of real sand and its specific volume after shearing.

real sand. These are broadly as would be anticipated for an ideal granular material, according to the concepts of critical state soil mechanics (Schofield and Wroth, 1968).

It is clear that the numerical samples are more sensitive to normal stress

than the reference real sand. As mentioned before, numerical samples displayed much more volumetric dilation than real sand. Also the dependence of dilation on vertical effective stress is more pronounced in the numerical simulations than in the real sand (shown by a greater slope of the $\upsilon$-$\sigma'$ line in Figure 5.8(b) than that in Figure 5.9(b)). This suggests that the shear resistance contributed by volume change decreases more significantly with increasing vertical effective stress for the numerical sample than for the real sand. This is consistent with the more significant reduction in peak angle of shear resistance with increasing vertical effective stress for the numerical simulations.

The following numerical simulations with different particle shapes and interparticle friction angles, were carried out at a normal stress of $100kPa$ only.

## 5.6 Effect of particle shape

Numerical simulations were carried out to investigate the effect of particle shape factor in the range 1 to 2. In each of the simulations, the sample had 30000 particles and was sheared at a vertical effective stress of $100kPa$. The horizontal lines given in Figure 5.10(a) are the bulk friction angles at peak (47.7°) and at the end of the test (31.4°) for the reference real sand.

Figure 5.10 shows the bulk angle of shearing resistance and overall dilation of the numerical simulations as a function of the particle shape factor. The particle shape had a significant effect on the bulk shear strength. As the shape factor was increased from 1 to 2, the peak bulk friction angle increased from 36.5° to 80°, and the bulk friction angle at the end of shearing increased from 22.6° to 43.3°. For the case of spherical particles, a further numerical

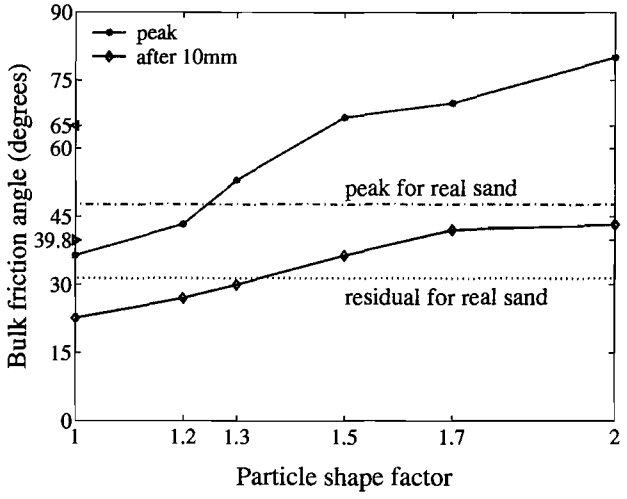


(a) Bulk friction angle against particle shape factor

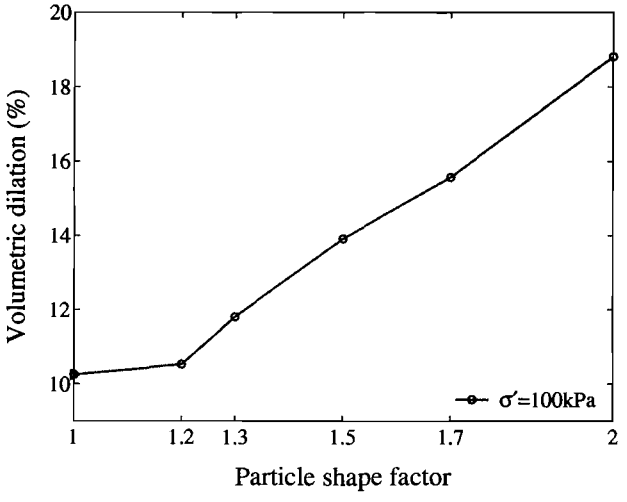


(b) Volumetric dilation against particle shape factor

Figure 5.10: Effects of particle shape: samples of initial porosity 0.33, $\phi_\mu = 30°$ and at normal stress of $100kPa$

simulation was carried out in which particle rotation was prevented. This increased the bulk friction angle from 36.5° to 65° at peak and from 22.6° to 39.8° at the end of shearing (see also Figure 4.9). This suggests that particle

rotation influences the strength-dilation behaviour significantly, and that the particle shape factor (with its effect on the freedom of a particle to rotate) will therefore also be an important factor influencing deformation and shear strength behaviour.

However, the particle shape may also contribute to the bulk shear strength in its own right, since the bulk shear strength of a sample comprising bonded particles with shape factor greater than 1.7 is higher than that of single spheres with rotation prevented. This is probably a result of the greater potential for interlocking as the particle shape factor is increased.

The variation in volumetric dilation with particle shape factor is shown in Figure 5.10(b). The volumetric dilation increased by almost 90% of its value (from 10% to 17%) as the particle shape factor was increased from 1 to 2. On the other hand, preventing the rotation of single spheres had little effect on volumetric dilation. This confirms that particle shape is a key factor affecting sample volume change, with a sample likely to dilate more if the particles are less spherical.

## 5.7 Effect of interparticle friction angle

Procter and Barton (1974) and Frossard (1979) found that the interparticle friction angle $\phi_\mu$ of saturated irregular quartz particles varies between 5° and 40°. The value used in the analyses described in this report (30°) is at the high end. Particle friction angles of 25° and 35° were used to examine the effect of this particle property on bulk shear strength and volumetric dilation. Simulations were run with 30000 particles, a vertical effective stress of 100 $kPa$ and a shape factor of 1.3. The results are shown in Figure 5.11.

While the peak bulk friction angles increased faster than those at the

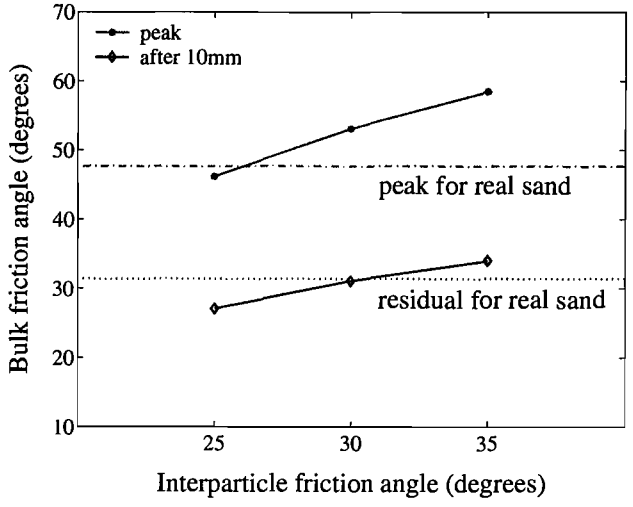


(a) Bulk friction angle against interparticle friction angle

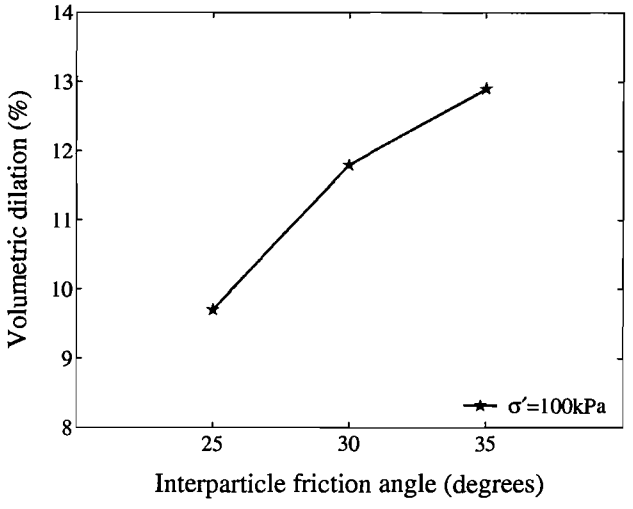


(b) Volumetric dilation against interparticle friction angle

Figure 5.11: Effects of interparticle friction angle: samples of the same number of particles, initial porosity and tested at constant normal stress

end of the simulations as $\phi_\mu$ was increased, both increased from less than to more than the values for the reference real sand. An explanation for

the increasing dilation with particle friction angle (Figure 5.11(b)) might be that increased interparticle friction results in more rotation and less sliding between particles and a consequent increase in the thickness of the shearing zone. This will be discussed further in the thesis.

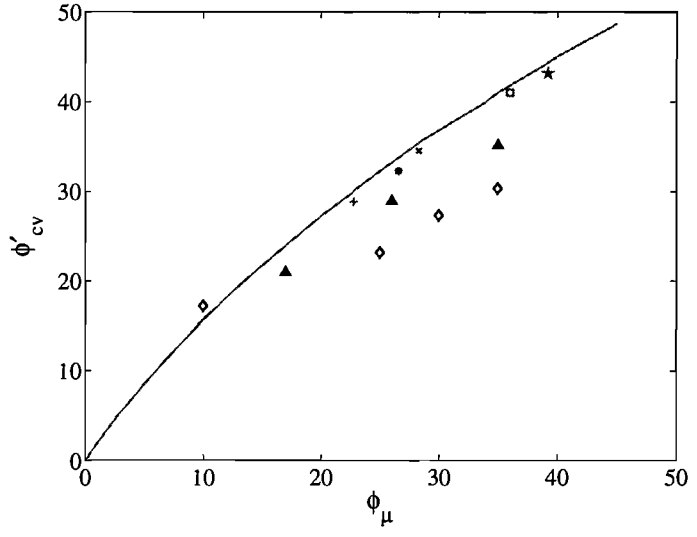


Figure 5.12: $\phi'_{cv}$ of non-spherical particles plotted against $\phi_\mu$ and compared with the theoretical curves of Horne (1969). ◇: numerical simulations (shearbox test) using bonded particles with shape factor 1.3, initial porosity 33%; ▲: numerical simulations (shearbox test) using bonded particles with shape factor 1.5, initial porosity 37%; □: feldspar (Lee, 1966); +: zircon, ∗: Mersey river sand (Rowe, 1962); ×: Welland river sand, ⋆: crushed glass (Parikh, 1967)

Unlike those of samples composed of uniform sized spheres (Figure 4.7), the values of $\phi'_{cv}$ for samples composed of non-spherical particles match the theoretical prediction by Horne (1969) better, though the values obtained from the numerical simulations are generally still less than the values predicted by Horne's relationship. The deviation might again result from significant particle rotation taking place in numerical samples. This seems to be supported by the fact that samples with higher particle shape factor of 1.5, hence more difficult for its particles to rotate, showed higher $\phi'_{cv}$ than

the samples with particle shape factor of 1.3.

Changing $\phi_\mu$ has the similar effect on the sample strength and dilation as changing other properties such as particle shape. However, these changes all affect the particle rotation. This suggests that the behaviour of a sample is related to the way particles move against each other, which is heavily affected by particle shape, $\phi_\mu$ and sample density . The concept of interference between particles affecting the thickness of the shear zone could also account for the increased dilation with particle shape factor noticed earlier. These will be discussed further in the thesis, with reference to previous experimental works.

## 5.8 Micro-deformation of shear zones

It is known that the deformation of an assembly of granular material results mainly from the sliding and rotation of particles (Oda, 1977; Oda et al., 1985; Ting et al., 1989). However, it is not clear how particle properties such as particle shape, particle size and interparticle friction angle will affect particle movement. An attempt has been made to gain an insight into the micro-movement of the particles of a sample during shearing by monitoring both the sliding and the rotation of individual particles. As described in Section 5.2, in each of the simulations, a total of 22 particles located within two columns was monitored. Figure 5.13 shows the rotations and displacements of these individual particles in the test using 30000 particles with a shape factor of 1.3 under a normal stress of $100kPa$.

The thickness of the zone of intense rotation (especially for column A, which is located in the middle of the sample) is considerably less than that of the shear zone as a whole. This increased rotation is not reflected in the dis-

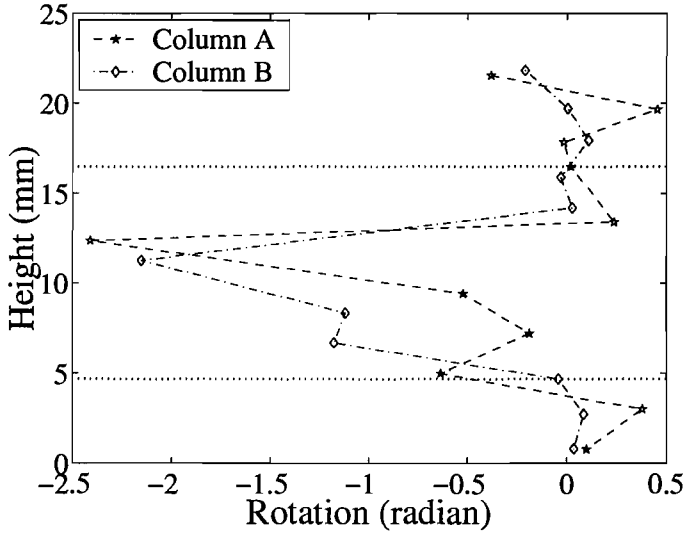


(a) Rotations of individual particles at different heights

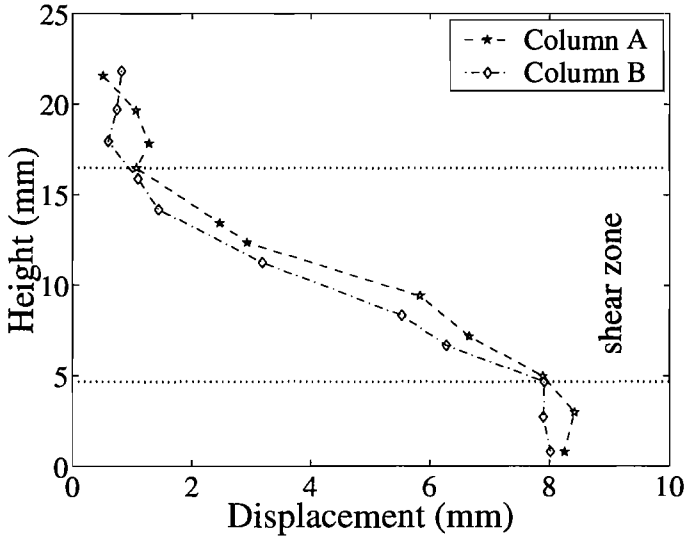


(b) Displacements of individual particles

Figure 5.13: Particle rotation and displacement for a sample comprising 30000 particles with particle shape factor 1.3 and interparticle friction angle 30°

placements defining the extent of the shear zone, which shows an essentially uniform gradient throughout the zone. It must therefore be concluded that the mechanisms in the shear zone which allow the necessary rearrangement of particles are more complicated than might have been thought. However, the shear zone is restricted by the boundaries of the shearbox and the predefined direction of relative movement, which means the shearbox is not an ideal tool to investigate the development of shear zones. The effects of particle properties (shape, $\phi_\mu$, etc.) on the width, inclination and micro-structure of the shear zone (particle rotation, voids) will be investigated in the simulations reported in the next chapter.

## 5.9 Summary

Numerical shearbox tests have been carried out to investigate the effects of the micro-properties of a granular material on its shear behaviour. The shear strength and stress–strain behaviour were examined for different particle shape factors, different numbers of particles in the sample, and for three different interparticle friction values and four normal effective stresses. An increase in the normal effective stress resulted in a decrease in the mobilised friction angle, both for the peak and residual values, though the amount of decrease (for both peak and residual angle of shearing resistance) was considerably greater for the numerical model than for the real sand over the range investigated. Also, the movements of individual particles in the shear zone were investigated. The main conclusions are as follows:

1. The number of particles in the sample is important. It affects most significantly the residual bulk friction angle and the volumetric dilation of the sample. Both fell by about 24% when the number of particles

was increased from 5000 to 50000, while the peak bulk friction angle decreased slightly by 4%. However, the changes in peak friction angle and volumetric dilation were less marked when the number of particles was more than 30000.

2. Particle shape plays an important role in the movement of the particles. Greater bulk friction and dilation angles were apparent with less spherical particles. Both the peak and residual bulk friction angles exceed those of single spheres whose rotation is prevented when the particle shape factor is greater than 1.7. This might be a result of interlocking which makes it more difficult for particles to rotate when they are less spherical.

3. An increase of 10° in interparticle friction angle resulted in an increase of 12.5° in the peak bulk friction angle. This indicates that the particle friction angle contributes significantly to the shear strength as the sample starts to dilate. The bulk friction angle at the end of simulation was slightly less than the interparticle friction angle when the latter was 35°. This might reflect a higher proportion of rotational as opposed to sliding movement (once the sample had dilated to the residual value) than for lower interparticle friction values. In contrast to the behaviour of samples consisting of spheres, the value of $\phi'_{cv}$ increases with the value of $\phi_\mu$ and the results from samples consisting of non-spherical particles with shape factor 1.5 show a closer match with the theoretical work of Horne (1969) than the results from samples with shape factor 1.3.

4. The major deformation of each sample was located within a 10 *mm* thick zone (shear zone) in the middle of the sample. Within this zone

was a narrower zone of intense rotation. This suggests a complicated mechanism of micro-deformation which awaits further investigation.

# Chapter 6

# Numerical simulation of biaxial test

## 6.1 Introduction

The results from numerical simulations of direct shearbox tests revealed that particle shape had significant effect on the stress–strain behaviour of samples. When the samples were composed of uniform sized spheres, the shearing resistance at the critical state ($\phi'_{cv}$) was independent of the interparticle friction angle $\phi_\mu$ (Chapter 4. When the samples were composed of bonded pairs of spheres (Chapter 5, and Ni et al. 2000), the shear strength increased with increasing $\phi_\mu$. As the particles became less rotund, the sample showed higher bulk shear strength resulting from greater potential for interlocking. The results from simulations of shearbox tests also suggested that particle rotation was an important factor in sample deformation.

However, the deformation imposed on the shearbox sample is far from uniform. The strain is concentrated at the central horizontal plane, resulting in a rupture surface at the interface between the two sections. Thus,

shearbox is not the best tool to study the development of shear bands in regard to particle properties and loading conditions because the shear zone in a shearbox has a fixed direction and location.

This Chapter presents the results of a series of numerical simulations of biaxial tests on assemblages of particles using the discrete element computer code PFC–3D . Individual particles were modelled by means of pairs of strongly bonded spheres. Stress controlled flexible boundaries, simulating rubber membranes, were used to apply the minor principal effective stress, $\sigma_3'$. Simulations were carried out to investigate the effect of varying the friction of the loading platens, the initial porosity of the sample, the particle shape (aspect ratio or rotundity), and the interparticle friction angle $\phi_\mu$. The results of the simulations are discussed with reference to the stress-strain behaviour observed in biaxial tests on a real sand reported by Alshibli and Sture (2000).

The main aims of the study were

1. to demonstrate the ability of numerical simulations in which the soil is modelled as an assemblage of discrete particles to capture the essential macro-features of soil behaviour as observed in laboratory tests, including the dependence of peak strengths on the initial void ratio relative to the critical state,

2. to explore the effect on the numerical model of varying the porosity, particle shape factor and surface (interparticle) friction angle, and

3. to investigate the development of strain localisations or shear bands in the numerical simulations.

Biaxial tests, rather than the more usual triaxial tests, were modelled in the numerical simulations as being more relevant to most practical problems

and for reasons of computational expediency.

## 6.2 Numerical modelling procedure

The sample modelled in the numerical biaxial test simulations had dimensions of 30 $mm$ × 20 $mm$ × 60 $mm$ in the directions of the minor ($x$), intermediate ($y$) and major ($z$) principal stresses respectively, as shown in Figure 6.1. The sample was constrained by a pair of stress-controlled flexible boundaries (membranes) normal to the $\sigma_3'$ or $x$-direction, each of which was formed by a single layer of frictionless spheres. These boundary spheres were small and close enough to prevent particles escaping from the sample through the gaps between them. Rigid frictionless plates (not shown in Figure 6.1) were placed to constrain the sample in the $\sigma_2'$ or $y$-direction. A confining stress of 100 $kPa$ was maintained normal to the flexible boundaries during each test. Each of the spheres forming the flexible boundary was free to move horizontally in the direction of the minor principal stress, but movement towards the rigid front and back side plates ($y$-direction) was prevented. Initially, a small gap was specified between the horizontal rows of spheres representing the membrane. Contraction of the membrane during the numerical biaxial test was modelled by imposing a vertical ($z$-direction) velocity proportional to the movement of the end loading platens on each of the successive horizontal layers of boundary spheres, gradually closing the gaps.

Each of the particles used to make up the simulated soil sample was formed by bonding two spheres together, as shown in Figure 5.2. The bond acts in effect as a column of elastic glue, of specified strength and stiffness. In principle, the bond strength and stiffness can be varied to simulate deforma-

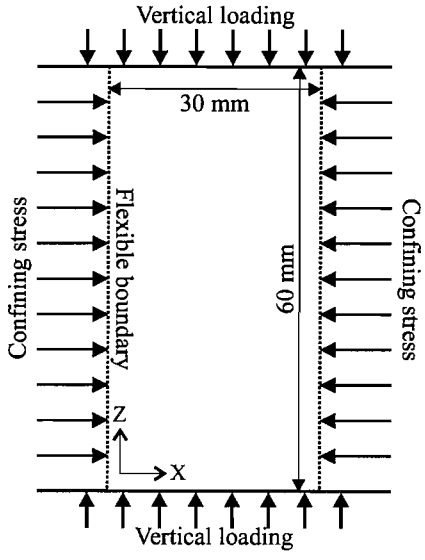


Figure 6.1: Schematic illustration of the biaxial test

tion behaviour within the particle. In this study, the strength and stiffness of bond were high enough for the bonds not to break or deform significantly so that each pair of spheres behaved as a single rigid particle. Particle breakage, which may in reality (depending on the soil type and stresses being applied) influence the behaviour of a real soil (McDowell and Bolton, 1998) was not modelled in the analyses reported in this thesis. Particle breakage has been modelled in samples comprising particles each made up of clusters of less strongly bonded spheres (McDowell and Harireche, 2002; Cheng et al., 2003), but to extend this to the 10000-particle samples used in this study would have resulted in excessive computational times.

The procedure of preparing a sample and the choices of stiffness for particle and parallel bond were the same as described in Section 5.2.

The overall shape of a particle was characterised by a shape factor defined as (R+r)/R, where R and r are the radii of the larger and smaller spheres respectively (see also in Chapter 5). A single spherical particle has a shape factor of 1 and marks one end of the range of possible shape factors, whilst a

particle comprising two spheres of the same size has a shape factor of 2 and defines the other end of the range. In one of the series of analyses carried out as part of this study, the shape factor was varied between these limits to examine the effects of particle shape. In other analyses a shape factor of 1.5 was used as this value is close to that of many real sands (e.g. Mitchell, 1993; Saussus and Frost, 2000).

The particle size relative to the overall sample dimensions (i.e. the number of particles in a sample of given volume) is also important. It affects most significantly the bulk effective friction angle (by changing the proportion of particles affected by the presence of boundary surfaces) and the total volumetric dilation of a sample (by changing the proportion of particles in the active shearing zone). Simulations of shearbox tests (Chapter 5 and Ni et al. (2000)) suggested that the number of particles within a sample of dimensions 60 $mm$ × 60 $mm$ × 20 $mm$ had to be greater than 15000 not to affect significantly the peak effective friction angle and the volumetric dilation in 3-D numerical simulations of direct shear tests. This is equivalent to fitting 7500 particles into the 60 $mm$ × 30 $mm$ × 20 $mm$ samples used in this study, suggesting that the 10000 particles actually used to form each sample would be sufficient to avoid the results being significantly affected by the number of particles used.

Figure 6.2 shows a sample comprising 10000 particles of shape factor 1.5 and having a porosity of 0.35: for clarity, the loading platens and side plates have been omitted. Taking the diameter of the larger ball as the mesh-passing size of the whole particle, the particle size distribution for this numerical sample ranged from 0.41 $mm$ to 1.89 $mm$.

The numerical samples replicated the relative particle size distribution (with the small tails at either end of the range removed) of a medium Leighton

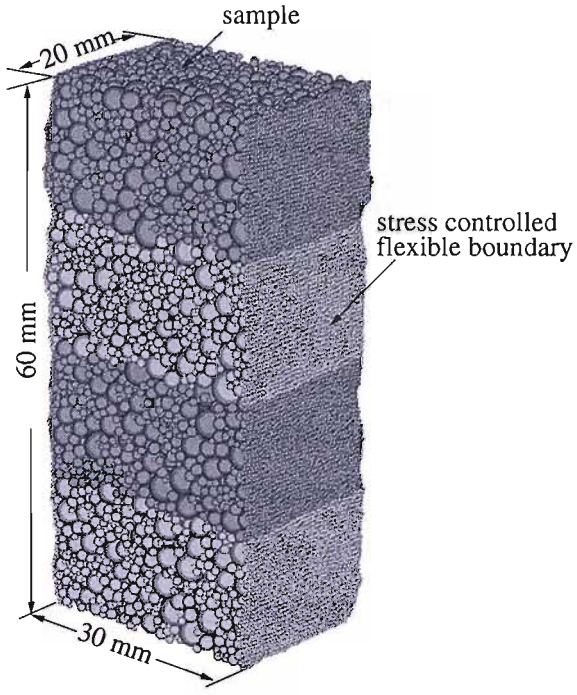


Figure 6.2: A typical sample with 10000 particles

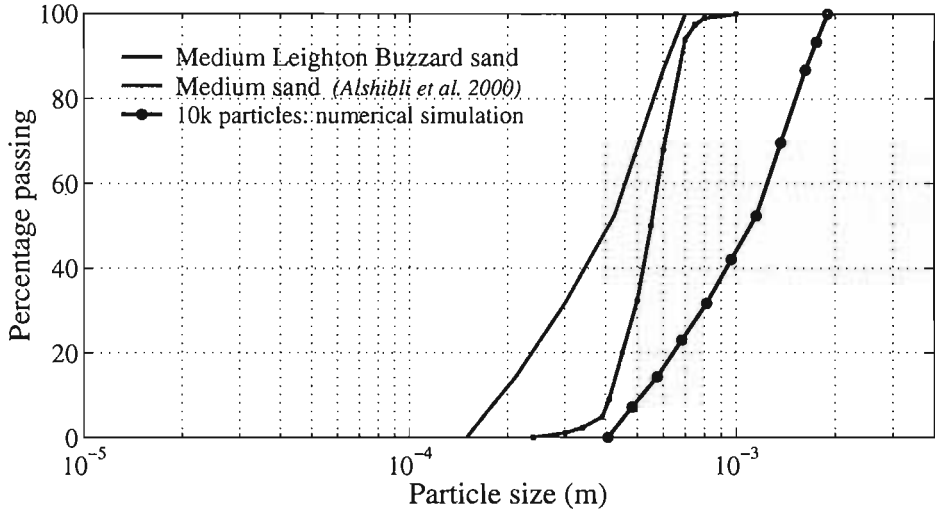


Figure 6.3: Particle size distribution of sands and numerical samples.

Buzzard sand (Figure 6.3). The mean particle size to give 10000 particles in the numerical model was about 2.7 times that of the Leighton Buzzard sand, varying slightly depending on the chosen values of shape factor and initial

porosity. The range of porosity investigated was 0.35 to 0.40 corresponding to the maximum and minimum packing found practical for these particles. Figure 6.3 also shows the particle size distribution of the medium subangular quartz sand (with $d50 = 0.55\ mm$) used in biaxial tests by Alshibli and Sture (2000), whose results are compared later with those from the numerical simulations.

After a numerical sample had been generated at the required porosity, a confining stress of 100 $kPa$ was applied to the two flexible boundaries and the sample was allowed to come to equilibrium with the loading platens and the two side plates fixed. The numerical biaxial test was then carried out by driving the two rigid loading platens at the top and the bottom of the sample towards each other at a relative speed of $3 \times 10^{-5}\ mm$ per calculation step until their relative displacement approached 10 $mm$ (corresponding to an axial strain of 16.7% ). Lateral displacement and tilting of the loading platens was prevented, and the two smooth side plates were kept stationary throughout sample preparation, application of the confining stress and shear.

During each simulation, the vertical load and the overall volumetric dilation of the sample were recorded. Also, rotations were monitored for each of about 5,000 particles within a 10 $mm$ vertical slice of the sample centred between (and thus 5 $mm$ away from) the two side plates.

Four series of analyses were carried out to investigate the effects on overall behaviour of loading platen friction, the initial porosity of the sample, the particle shape factor, (R+r)/R and the interparticle friction angle, $\phi_\mu$ as summarised in Table 6.1.

In each series (except for a subsidiary series for intergranular friction in which the platen friction was set to zero) the remaining parameters were set to common reference values. The interparticle friction angle $\phi_\mu$ was taken as

Table 6.1: Summary of numerical simulations reported in this chapter

| | $\delta_{platen}$ | $n_{init}$ | Shape factor | $\phi_\mu$ |
|---|---|---|---|---|
| $\delta_{platen}$ | 0°, 0.5°, 2.5°, 5°, 26° | 0.35 | 1.5 | 26° |
| $n_{init}$ | 26° | 0.35, 0.37, 0.38, 0.40 | 1.5 | 26° |
| Shape factor | 26° | 0.35 | 1.0, 1.3, 1.5, 2.0 | 26° |
| $\phi_\mu$ | 26° | 0.35 | 1.5 | 17°, 26°, 35° |
| | 0° | 0.35 | 1.5 | 17°, 26°, 35° |

26° typical for medium quartz sand (Rowe, 1962; Rowe and Barden, 1964; Procter and Barton, 1974). The initial porosity of 0.35 corresponded to a relative density of, perhaps, 90% to 100% , for the simulated material with this shape factor. For all tests the confining stress on the lateral boundaries was fixed at 100 $kPa$.

The third objective of the study was to explore the development of localisations during shear. Oda and Kazama (1998) reported that, within shear-bands, particles re-orientated when sheared. This was also observed in 2-D DEM simulations of biaxial tests by Iwashita and Oda (1998). Localisation in the numerical simulations was therefore investigated by monitoring the magnitude of particle rotations to give an indication of the degree of structural disturbance and its distribution. However, the degree of disturbance is indicated by the absolute magnitude of the particle rotations rather than the underlying (much lower) rotation of the material continuum.

Because of the difficulty in obtaining true material properties from a test or simulation which results in non-homogeneous deformation, the results quoted for axial stresses (except for a discussion and diagrams relating to homogeneous deformation using smooth platens) are uncorrected for changes in cross-sectional area: they should therefore be regarded as comparable but

qualitative.

## 6.3 Loading platen friction

In these analyses, the angle of friction between the loading platens and the sample ($\delta_{platen}$) was set at a variety of values representing zero (a theoretical ideal) and a range (0.5°, 2.5°, 5° and 26°) from lubricated to rough platens that might be obtained in laboratory tests: results for $\delta_{platen} = 0°, 2.5°$ and 26° are reported. In a laboratory test, end platen friction might be reduced to about 0.5° by means of one or more layers of lubricated membrane, but cannot be eliminated entirely (Hettler and Vardoulakis, 1984; Head, 1988). The friction angles between the sample and the side plates and between the sample and the flexible boundaries was set to zero.

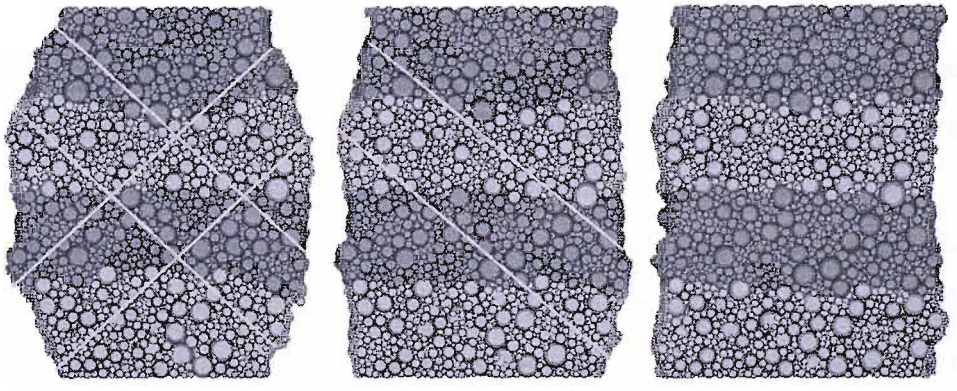

(a) $\delta_{platen} = 26°$ (b) $\delta_{platen} = 2.5°$ (c) $\delta_{platen} = 0°$

Figure 6.4: Numerical samples at 16.7% axial strain using rough/smooth platens. (a) $\delta_{platen} = 26°$. (b) $\delta_{platen} = 2.5°$. (c) $\delta_{platen} = 0°$

The deformations at the end of test of the three numerical biaxial test samples, having $\delta_{platen} = 26°, 2.5°$ and 0°, are shown in Figure 6.4. In the test with the 26° friction platens the development of platen shear stresses

significantly restrained the movement of the particles at the ends of the sample and resulted in the formation of 'dead zones' at the ends, an obvious bulging of the centre, and the development of two shear bands as indicated in Figure 6.4(a). Figures 6.4(b) and 6.4(c) show that, as expected, the degree of restraint decreased and the sample deformed more uniformly as the loading platen friction angle was reduced towards zero. Evidence for the development of shear bands is discussed later, but it was found necessary to reduce the loading platen friction angle to 2.5° or below to ensure substantially uniform deformation during imposition of the 16.7% axial compression.

Figure 6.5 show graphs of shearing resistance and mean volumetric dilation $\varepsilon_{vol}$ against mean axial strain $\varepsilon_{ax}$ for the three numerical biaxial test simulations. The shearing resistance was calculated using Equation (6.1):

$$\phi' = sin^{-1}(\frac{\sigma'_1 - \sigma'_3}{\sigma'_1 + \sigma'_3}) \tag{6.1}$$

where $\sigma'_1$ and $\sigma'_3$ denote the mean major and minor effective stresses (taken, respectively, as the mean vertical and horizontal principal effective stresses). For the simulation using rough loading platens ($\delta_{platen} = 26°$), the sample reached a peak angle of shearing $\phi'_{peak}$ of 54° at an axial strain of 2.8% , followed by softening to a mobilised angle of shearing of 43° at the final mean axial strain of 16.7%. For the simulations modelling low (2.5°) and zero friction platens, the peak in strength was less pronounced ($\phi'_{peak} = 50°$) and occurred at the slightly greater axial strain of about 4% . The mean volumetric dilation for the latter two simulations was somewhat greater than for that with rough platens and inspection of the graph of $\varepsilon_{vol}$ against $\varepsilon_{ax}$ suggests that a critical state had not quite been achieved in any case.

It would seem reasonable to regard the zero friction test, with its essentially uniform distortion, as an example of plane strain behaviour for a

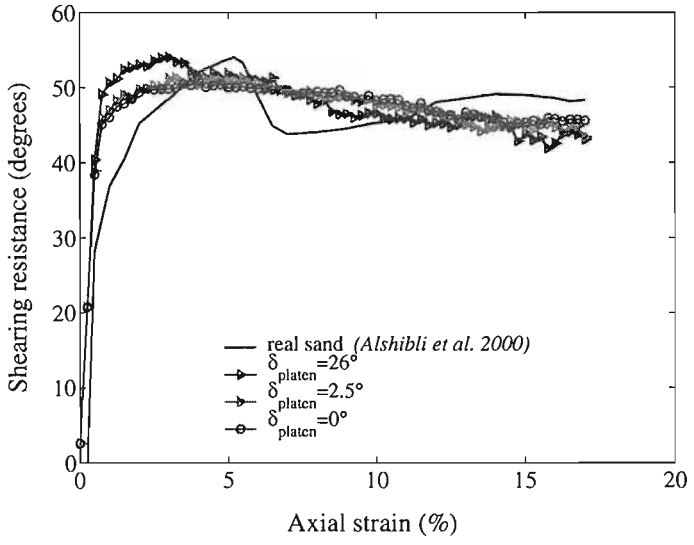


(a)

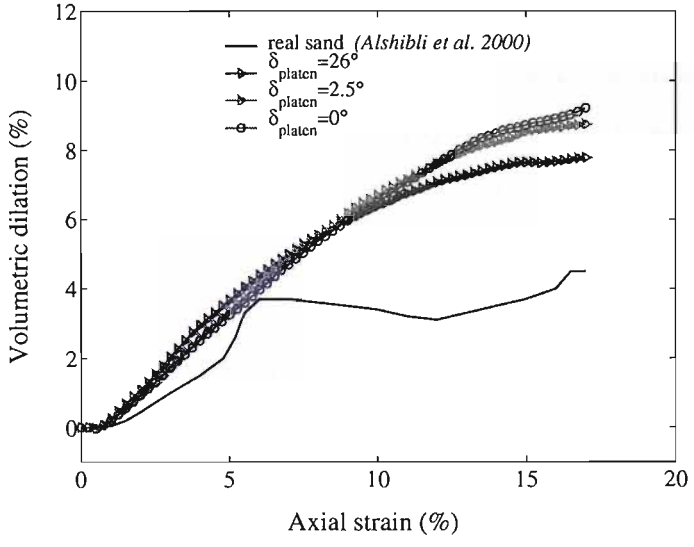


(b)

Figure 6.5: Shearing resistance and volumetric dilation of the samples in Figure 6.4(a) and of a real sand using data from Alshibli and Sture (2000) (a) Shearing resistance against axial strain. (b) Volumetric dilation against axial strain

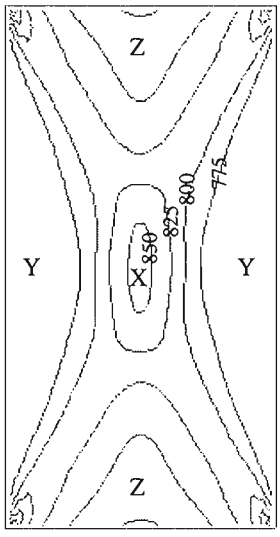


Figure 6.6: Contours of $\sigma'_1$ (kPa) at peak shearing resistance calculated by the continuum code FLAC (Ni et al., 2003)

material element. For the standard particle properties and smooth loading platens, the peak effective friction angle $\phi'_{peak}$ and the dilation angle at peak may be taken from Figures 6.5(a) and 6.5(b) as 50° and 16° respectively. To help explain the higher peak strength in the rough platen test, the stress distribution within the sample was determined from an elastic/Mohr-Coulomb plastic continuum analysis carried out using the program FLAC 4.0 from Itasca Consulting Group, 2000. In the continuum analysis the peak frictional and dilational material properties ($\phi'_{peak} = 50°$, $\psi_{max} = 16.3°$), obtained from the PFC–3D simulation with smooth platens, were taken as the yield values and used with a platen friction angle of 26°. The resulting contours of major principal stress at peak axial stress are shown in Figure 6.6. It may be seen that the mid height values of vertical stress vary from a minimum on the lateral boundaries of 755 $kPa$ (governed by the applied lateral stresses), to a maximum in the centre of the sample lying inside (and therefore with a value greater than) the 850 $kPa$ contour. These values may

be compared with the theoretical vertical yield stress using smooth platens which, for the same 50° friction angle material, is a uniform 755 $kPa$.

The fact that the rough platen simulation showed a higher strength and a higher dilation angle at peak than the smooth platen simulation can now be explained as follows. At mid height the major principal stress would, by symmetry, be vertical and, on the face of it, would be limited at yield by the applied lateral stress (as with the smooth-platen sample). Clearly, the vertical stress must build up to a higher value away from the lateral boundaries and, for this to happen, the local lateral stress must also be higher. The stress distribution indicated by the contours of $\sigma'_1$ in Figure 6.6 obtained in the Mohr-Coulomb continuum analysis of the rough platen test show a clear arching mechanism, springing from the edges of one platen to the edges on the same side of the opposite platen. To maintain equilibrium, the curvature of the lines of action of $\sigma'_1$ must be balanced by a corresponding increase in $\sigma'_3$ across the thickness of the arch, resulting in higher horizontal stresses between the two arches (zone X in Figure 6.6) than on the boundary (zones Y). The higher $\sigma'_3$ stress in the centre then allows a higher $\sigma'_1$ (vertical) stress without the Mohr-Coulomb yield value of the material being exceeded.

The continuum analysis also helps to explain the higher apparent dilation rate up to peak shown by the curve for the rough platen simulation in Figure 6.5(b) compared with the smooth platen case. The material zones on either side of the 'dead zone' wedges (Z) are not compressing vertically but along the inclined edges of each wedge. This causes the major principal strain in these areas to become inclined to and greater the strain in the vertical direction. Since strain occurs in the denominator of the dilation rate expression (Equation (6.2) from Bransby (1971)), the true dilation rate is less than the value derived on the basis of vertical strain and would thus be

closer to that found in the smooth platen simulations.

$$\nu = \sin^{-1}\left(\frac{-\frac{d\varepsilon_{vol}}{d\varepsilon_1}}{2-\frac{d\varepsilon_{vol}}{d\varepsilon_1}}\right) \tag{6.2}$$

For the numerical biaxial simulation test with rough platens, approximately one third of the material (i.e., that contained in zones Z in Figure 6.6) does not yield appreciably beyond peak strength. The conclusion is that the overall plastic vertical displacement and volume change are a result of what is happening in the remaining two thirds of the material. It follows that, to obtain the true strain scales for the deforming material beyond the peak strength, the coordinates of both axes in Figure 6.5(b) must be multiplied by a factor of 1.5. If this is done for the rough platen test results, having first set the initial dilation rate to that of the smooth-platen simulation (for the reason just described), it will be found that its curve lies very close to that for the smooth platen case, but then extends on to a dilation of about 10% at 23% axial strain. The implication is that the smooth platen simulations would have behaved similarly to those with rough platens had they been allowed to compress sufficiently to do so.

After the sample had reached the peak shearing resistance, the mode of deformation in the simulation with rough platens changes from a general compression of all of the material outside the dead zones, Z, to one of shear in two shear bands, as can be seen in Figure 6.4(a). However, there is no direct indication here of material localisation since the width of the bands is the maximum consistent with each band penetrating completely through the sample. The arches that developed before peak are destroyed when a shear band cuts across them (as happened in the continuum simulation when carried beyond peak), resulting in the rapid removal of the extra strength that arching was able to provide.

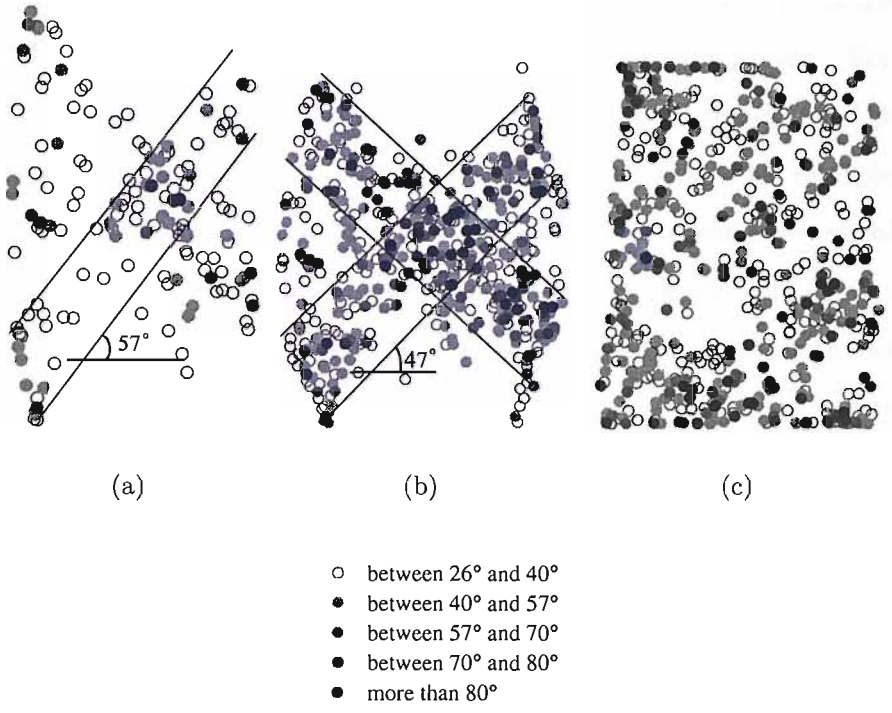


Figure 6.7: Distribution of particle rotation in the numerical samples using particles with shape factor 1.5 and $\phi_\mu = 26°$. With 26° friction angle on the loading platens, (a) the shearband emerges at the peak stress and (b) fully developed at the end of the test. (c) With 0° friction angle on the loading platens, no shearband appears

During each numerical biaxial test simulation, the degree of particle rotation generally increased with increasing axial strain. Figures 6.7(a) and 6.7(b) show the evolution of particle rotations within the middle 10 *mm* thick vertical slice of the rough end-platen sample (parallel to the smooth side platens). At the peak angle of shearing resistance (reached after an axial strain of 2.8% ), considerable particle rotation has occurred within localised zones (Figure 6.7(a)). By the end of the simulation (corresponding to an axial strain of 16.7% ), large particle rotations were concentrated mainly within the two bands following the sample diagonals as indicated in Figure 6.7(b). Particle rotations are smallest in the two wedge-shaped 'dead zones' adjacent

to the loading platens, and are particularly intense in the central diamond shaped area formed by the intersection of the diagonal bands. For comparison, Figure 6.7(c) shows the much more uniform distribution of particle rotations at the end of the simulated biaxial test with smooth end platens.

With the sample having smooth loading platens, there were no obvious zones of intense particle rotation even by the end of the simulation (Figure 6.7(c)). Analysis of the distributions of particle rotation for the samples having 26° and 0° angles of loading platen friction shows the average particle rotation to be approximately the same for both (about 24°). In both cases, 7% of particles rotated more than 57°. For the rough loading platen simulation, were concentrated within the shear bands while, for the smooth-platen simulation, they were evenly distributed throughout the sample. Again in both cases, about 70% of particles rotated less than 26°.

## 6.4 Initial sample porosity

The analyses described in this section were carried out to investigate the effect of the initial sample porosity on its stress-strain behaviour. Apart from the initial porosity, the samples were generated and the biaxial tests simulated exactly as above, each sample comprising 10000 particles of shape factor 1.5 and interparticle friction angle $\phi_\mu = 26°$. The confining stress was 100 $kPa$ and the loading platen friction angle was 26°. Figure 6.8 show the results of four simulations carried out from initial porosity, $n$, of 0.35, 0.37, 0.38 and 0.40, in terms of shearing resistance $\phi'$ (Equation (6.1)) and specific volume against axial strain $\varepsilon_{ax}$.

The peak angle of shearing resistance varied from 54° for the densest sample to 44.5° for the loosest. The corresponding range of shear strains at peak

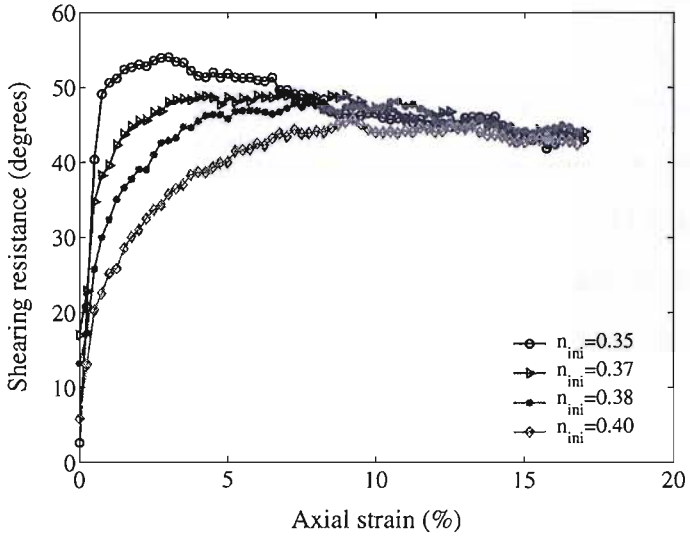


(a)

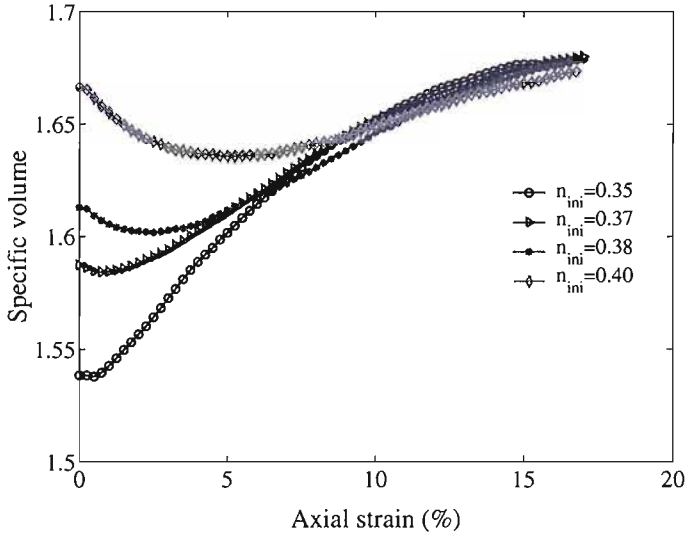


(b)

Figure 6.8: Stress ratio and volumetric dilation of the sample with various initial porosities (a) Shearing resistance against axial strain. (b) Specific volume against axial strain

strength was 2.8% (densest) to 10% (loosest). The final angle of shearing resistance, at 16.7% axial strain, was about 43° in all cases (Figure 6.8(a)). The graph of specific volume against axial strain (Figure 6.8(b)) shows that the peak strength is associated with sample dilation. For the densest sample, the dilation angle at peak strength was nearly 18° compared with 4.5° for the loosest. All the simulations showed a dilation rate of about 3° after 16.7% axial strain, indicating that a critical state had not quite been reached.

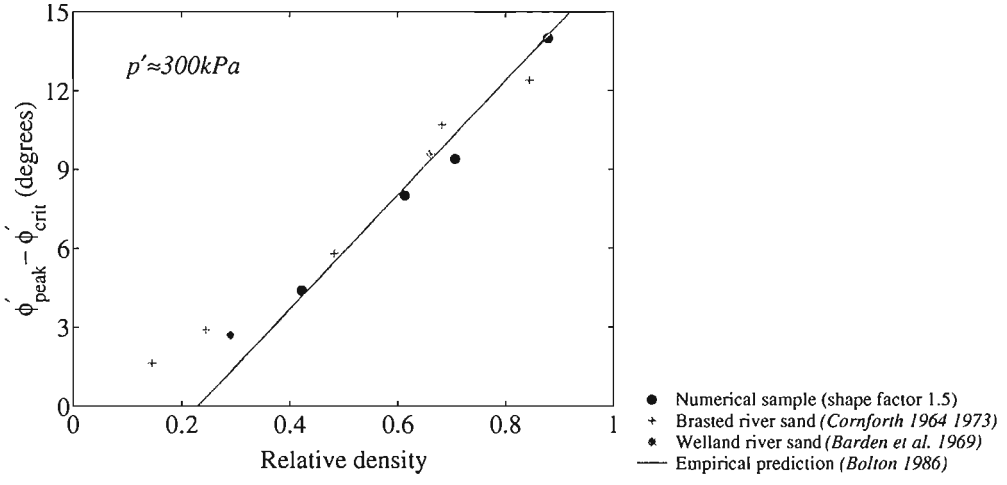


(a)

Figure 6.9: $(\phi'_{peak} - \phi'_{crit})$ against relative density. Correlation of numerical samples with various sands from literature (average effective stress approximately 300 $kPa$)

Figure 6.9 shows various biaxial test data plotted as $\phi'_{peak} - \phi'_{cv}$ against relative density, $I_D = (e_{max} - e)/(e_{max} - e_{min})$. Data from the numerical simulations reported in this chapter are also shown, with the porosities expressed as relative densities having chosen the maximum and minimum porosities ($n_{max} = 0.44$ and $n_{min} = 0.335$) to give the best fit with data from Bolton (1986). (There is no easy way to decide what the porosities at 0%

and 100% relative density should be with numerical models. The fit shown in Figure 6.9 required an unexpectedly high porosity, n = 0.44, for 0% relative density compared with the loosest numerical sample, n = 0.40, but this could be justified by the difficulty in obtaining very loose numerical samples with particles made of spherical elements: real sand has relatively sub-angular particles. Figure 6.9 shows that all the numerical values lie essentially on the same straight line as the real sand data, given by Equation (6.3) (Bolton, 1986, Eq. 15).

$$\phi'_{peak} - \phi'_{cv} = 5I_R \qquad \text{where} \qquad I_R = I_D(10 - \ln p') - 1 \tag{6.3}$$

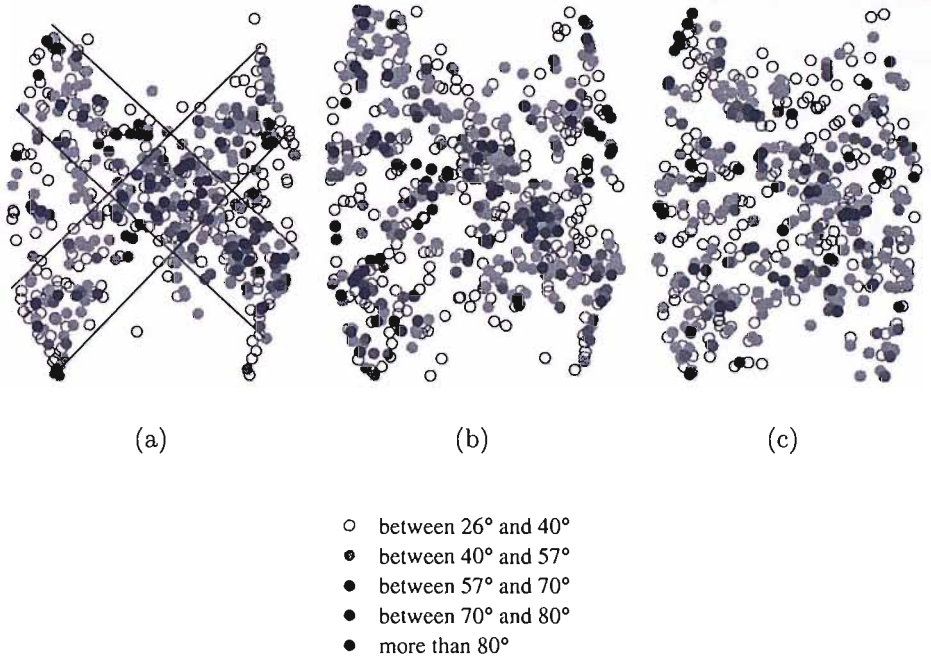


Figure 6.10: Particle rotations in numerical samples with various initial porosities, samples using particles shape factor 1.5 and $\phi_\mu = 26°$. (a) n=0.35, (b) n=0.38 (c) n=0.40

The effect of porosity on particle rotations is illustrated by comparing

Figures 6.10(b) and 6.10(c) for the (loose) samples with 0.38 and 0.40 initial porosity, with Figure 6.10(a) (a repeat of Figure 6.7(b)) for the dense sample. With increasing porosity, the degree of banding (as indicated by the proportion of particles rotating more than 80°) reduces. Banding has practically disappeared in the loosest sample, in which all the material outside the dead zones exhibits a similar rotation pattern and even the 'dead zones' are beginning to be affected.

## 6.5 Particle shape factor

The simulations reported in this section involved numerical biaxial tests on samples comprising particles of shape factor (= $(R+r)/R$) of 1.0, 1.3 and 2.0 in addition to the value of 1.5 used to obtain the results already discussed. Each of the samples contained 10,000 particles with interparticle friction 26°; the loading platen friction angle was also 26°. All samples were prepared at an initial (dense) porosity of 0.35 under a confining stress of 100 $kPa$ and then sheared exactly as described earlier.

Figure 6.11 show the shearing resistance and the mean volumetric dilation against mean axial strain for each of four particle shape factors. The peak angle of shearing resistance increases with shape factor, as would be expected owing to the increased opportunity for interlocking and dilation (Mitchell, 1993). Both the maximum angle of dilation $\psi_{peak}$ (Figure 6.11(b): calculated according to Equation (6.2)) and the overall dilation of the sample during the test increased with increasing particle shape factor. These trends are consistent with those obtained in simulations of direct shear box tests reported by Ni et al. (2000) and in Chapter 5.

Comparison of these results with those of Alshibli and Sture (2000) tends

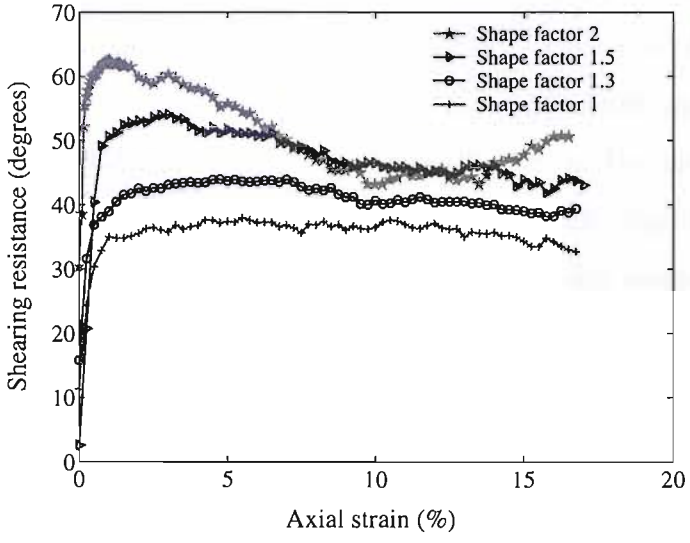


(a)

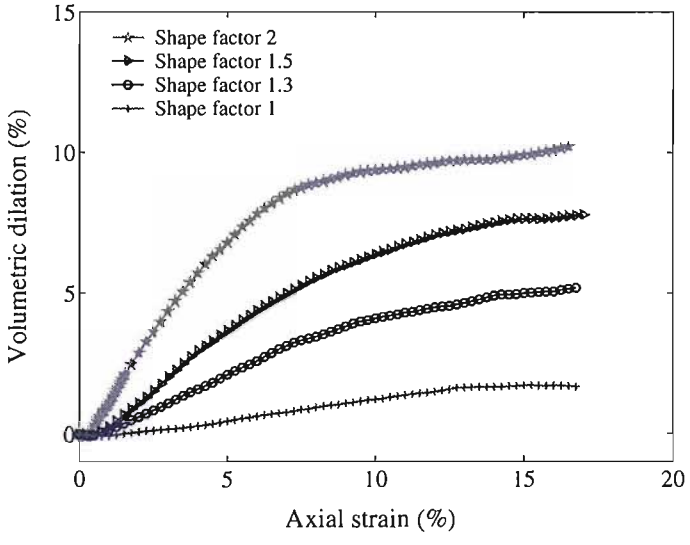


(b)

Figure 6.11: Shearing resistance and volumetric dilation of the samples with various shape factors (a) Shearing resistance against axial strain. (b) Volumetric dilation against axial strain

to confirm that a particle shape factor of 1.5 can provide a reasonable representation of the behaviour of a real sand (albeit one tested from a larger initial porosity), at least in terms of the peak and end-of-test angles of shearing resistance. However, the overall sample dilation at the end of the test is much greater in the numerical simulation than in the real test. This is almost certainly due to the relatively narrow shear band localisation in the real sand, perhaps as a result of the smaller particle size.

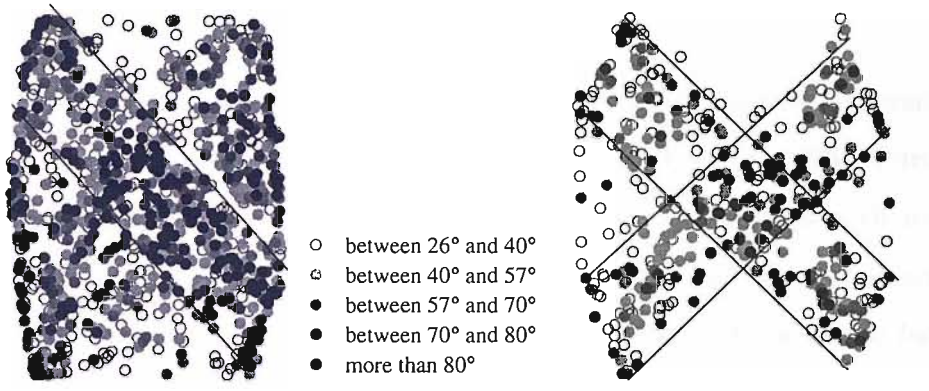


Figure 6.12: Particle rotations in numerical samples with various shape factors at 16.7% axial strain, initial porosity of 0.35 and $\phi_\mu = 26°$. (a) shape factor = 1 (b) shape factor = 2 . Rotations for shape factor = 1.5 are shown in Figure 6.7(b)

The effect of particle shape factor on particle rotation is illustrated in Figure 6.12, which show particle rotations at the end of test (axial strain of 16.7%) for samples having the extreme shape factors of 1.0 (Figure 6.12(a)) and 2.0 (Figure 6.12(b)). (The equivalent data for a shape factor of 1.5, the standard value, are shown in Figure 6.7(b)). The loading platen friction angle in these simulations was kept at 26°, as was the interparticle friction angle $\phi_\mu$. The degree of particle rotation reduces significantly as the particle shape factor is increased. The average of the end-of-test particle rotation

angles for the sample with particles having a shape factor of 1.5 was 20° (rising to 23° in an additional test (not shown) with smooth loading platens). The corresponding figure for the sample composed of spheres (shape factor 1.0) was 37°, reflecting the much greater proportion of large rotations. The simulation with a particle shape factor of 2.0 showed only a modest reduction of 2° in average particle rotation compared with a shape factor of 1.5.

## 6.6 Interparticle friction angle

Interparticle friction is known to have a significant effect on the deformation behaviour of a soil (Lee and Seed, 1967; Schanz and Vermeer, 1996). Further numerical biaxial test simulations were carried out on samples with interparticle friction angles of 17° and 35°, to complement the 26° tests already reported. The initial sample porosity was kept at 0.35 and the shape factor at 1.5.

The results, shown in Figure 6.13, show that interparticle friction has a large effect on both the peak and the end-of-test angles of shearing resistance, as well as the overall sample dilation at the end of shear.

Figures 6.14(a) and 6.14(b), for $\phi_\mu = 17°$ and 35° respectively, (and the equivalent plot for $\phi_\mu = 26°$ is Figure 6.7(b)) show a substantially higher proportion of rotations greater than 70° in the tests with particles having $\phi_\mu = 26°$ and 35° than for the test with $\phi_\mu = 17°$ - even though the average particle rotation for the high friction particles, at 22°, is only 3° higher than the 19° average of the $\phi_\mu = 17°$ test.

Comparison of the results of the simulations carried out to investigate the effect of shape factor and interparticle friction angle (Figures 6.12 and 6.14) shows that increasing the shape factor, at least from spherical up to a shape

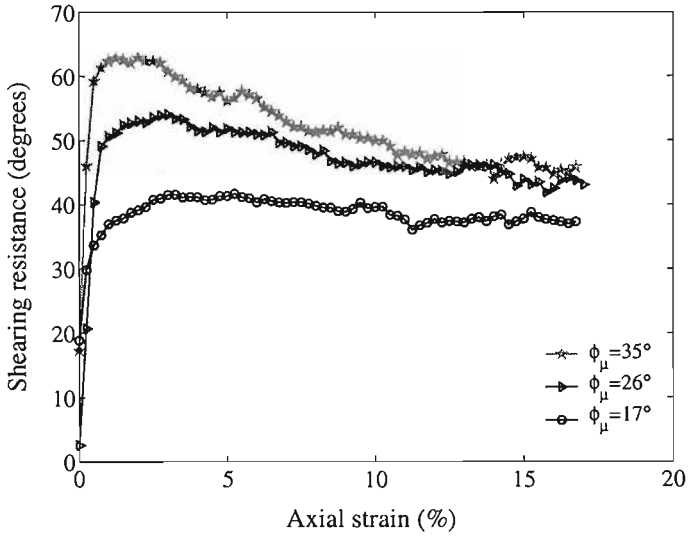


(a)

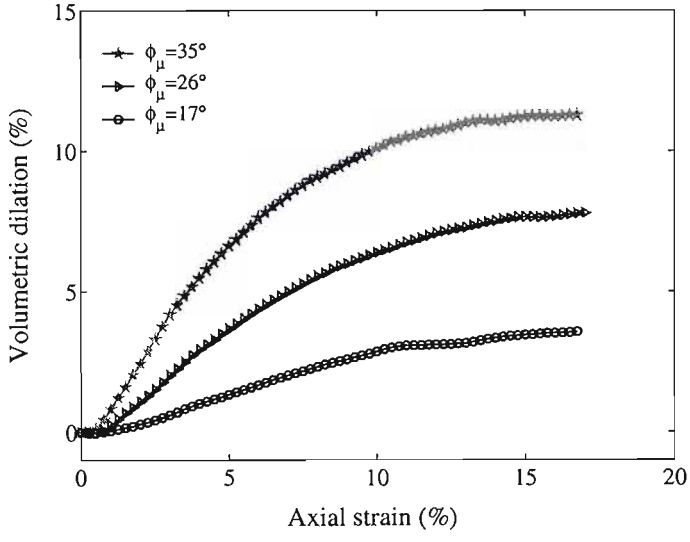


(b)

Figure 6.13: Shearing resistance and volumetric dilation of the samples using rough platens with various $\phi_\mu$ (a) Shearing resistance against axial strain. (b) Volumetric dilation against axial strain

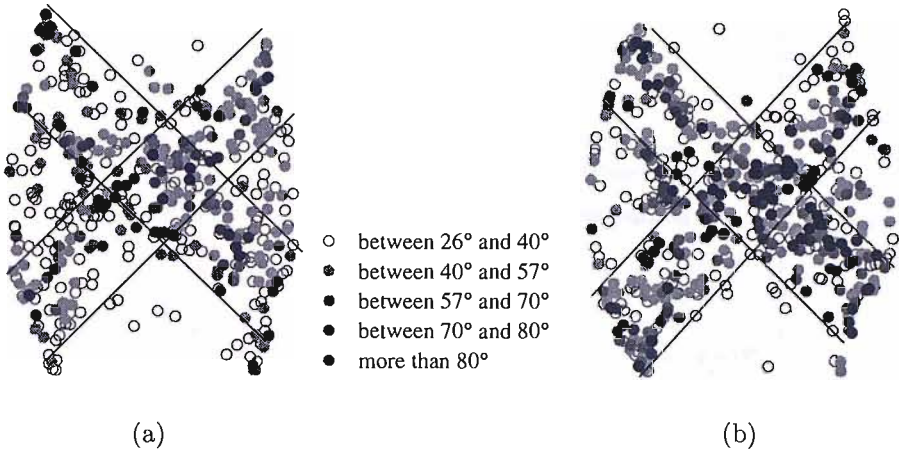


Figure 6.14: Particle rotations in numerical samples with various $\phi_\mu$ at 16.7% axial strain, samples initial porosity of 0.35 and shape factor 1.5 . (a) $\phi_\mu = 17°$ (b) $\phi_\mu = 35°$ Rotations for $\phi_\mu = 26°$ are shown in Figure 6.7(b)

factor of 1.5, dramatically decreased particle rotations (the further decrease for shape factor 2.0 being only 2° in average value), while increasing the intergranular friction angle from 17° to 35° resulted in an increase in average particle rotations from 19° to 22°. The spherical particles (Figure 6.12(a)) not only had much higher rotations (an average of 37° compared with 20° for the sample having a particle shape factor of 1.5) but these rotations were more evenly distributed over the sample and are seen to propagate into the wedge areas (termed dead zones in the context of other simulations).

A subsidiary series of interparticle friction angle simulations with smooth loading platens and from a low initial porosity ($n_{init} = 0.35$) was carried out to provide a set of uniformly-deformed samples from which material strength and dilation properties could be deduced, taking into account the actual cross-sectional areas resulting from axial strain and volume change at each stage of the simulations. The results - to allow comparison with the main series - for $\phi_\mu = 17°$, 26° and 35°, are given in Figure 6.15. These show

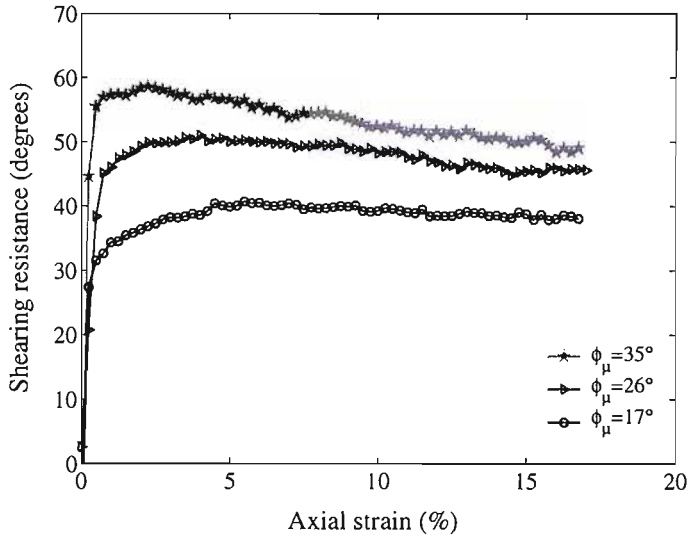


(a)

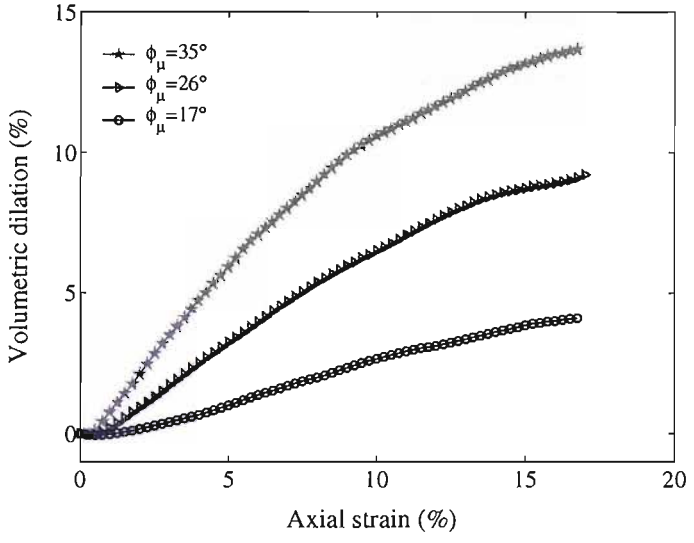


(b)

Figure 6.15: Shearing resistance and volumetric dilation of the samples using smooth platens with various $\phi_\mu$ (a) Shearing resistance against axial strain. (b) Volumetric dilation against axial strain

slightly lower peak values and greater end-of-test values of shearing resistance (Figure 6.15(a)) than those already reported for a platen friction angle of 26° (Figure 6.13(a)); volumetric dilation and dilation rates at end of test are also higher (Figure 6.15(b) compared with Figure 6.13(b)). Corrections for axial strain and volume change make little difference to peak values of shearing resistance which occur at small strain, but the end-of-test values are substantially lower (by 5° and 6° respectively for $\phi_\mu = 17°$ and 35°).

## 6.7 General discussion

The simulation in which the loading platen friction angle was set to zero Figures 6.4(c) and 6.7(c) demonstrates that for this boundary condition the behaviour of the (dense) numerical model was essentially homogeneous. The initial portion of the stress/strain curve is linear up to an angle of shearing resistance of about 40°, deviates very slightly from this initial line to about 45° and then curves smoothly through a peak of 50° (at an axial strain of 4% ) to fall gently to a final shearing resistance of about 45° at 16.7% axial strain. Both the angle of shearing resistance at the end of test and the accompanying 5° dilation rate were higher (by about 2°) than for the simulations with non-zero platen friction. This suggested the critical state had not been reached, but an estimate of 40° for the critical state angle of shearing resistance might be obtained by deducting the measured dilation angle from the angle of shearing resistance at the end of the analysis (this is discussed later).

In simulations with zero or very little friction on the end platens, the sample is not constrained laterally (as happens with rough platens) as there is little or no resistance to sliding on the platen surfaces. This can result in

the formation of a single slip band (as is beginning to happen in Figure 6.4(b)) that skews the sample, upsetting the uniform stress distribution and leading to a reduction in axial resistance. On these premises, a similar single shear band might be expected to occur at some stage in the zero platen friction simulation, the stage and direction at which it occurs being largely a matter of chance.

The rotation data in Figure 6.7 further illustrate the formation of shear bands in the numerical simulation with rough ($\delta_{platen} = 26°$) end-platens. Comparison of Figure 6.7(b) with Figure 6.4(a) demonstrates that the diagonal zones contain the main concentration of particle rotations and form bands of more intense shearing. At the peak angle of shearing resistance, the diagonal band shown in Figure 6.7(a) is inclined at about 57° to the horizontal plane, not too different from a theoretical value ($45° + \psi/2$, by Roscoe 1970), based on the dilation rate of 54°. However, although the width of the shear band at approximately 10 particle diameters is in agreement with that commonly reported (Scarpelli and Wood, 1982; Stone and Wood, 1992; Oda and Kazama, 1998), it is also (as discussed earlier) the maximum width that is kinematically possible for a shear band with this slope to pass through a sample of the dimensions used without intersecting the loading platens. At the end of the simulation the two diagonal bands defining zones of relatively high particle rotation were inclined at an angle of about 47° to the horizontal, and approximately 12 particle diameters thick (Figure 6.7(b)) - consistent with the original shear parallelograms becoming shorter and fatter in the course of deformation. Thus the shear bands seem to be controlled by the constraints of the boundary and could be regarded as uniform within those constraints rather than being determined by a random bifurcation and subsequent localisation as part of the shearing process.

The results for the range of initial porosity values between 0.35 and 0.40 are shown in Figure 6.8, in which the essential difference in deformation behaviour between the dense and the looser samples is seen to occur in the first 5% of axial compression (Figure 6.8(a)): the loose samples suffer a reduction in volume. After a transition phase occupying a further 5% axial strain, all samples then behave similarly to the end of the test. The dilation rates at the end of the simulations indicate that a critical state had not been reached in any of them. As with the simulation using frictionless platens, the critical state angle of shearing resistance (uncorrected for change in cross-sectional area) can be estimated by subtracting the end-of-test dilation angle (3°) from the final resistance angle (43°): again the value is 40° in all cases.

The two series of simulations involving varying particle properties - shape factor and interparticle friction angle - would appear, on the basis of the stress/strain and dilation/strain plots of Figures 6.11 and 6.13, to show similar effects. Peak strengths varied between 43° and 62° for the range of shape-factor (not including spherical particles), and between 41.5° and 62.5° for the range of interparticle friction angles investigated. The corresponding ranges for $\phi'_{cv}$ (after end-of-test dilation rate corrections) were 36° to 45.5° and 35° to 44°.

In all cases but the densest, the dilation rate at peak in the initial porosity series of simulations accounted for the difference between the peak angle of shearing resistance and the estimated critical value (thus justifying the much smaller end-of-test dilation rate adjustment to obtain the critical state value). For the densest (lowest initial porosity) sample, this difference was less being about 80% of dilation angle rather than 100% as in the other simulations. The dense porosity had been chosen as the standard for all the remaining simulations (see Table 6.1) and therefore warranted closer investigation of

the relation between $\phi'_{peak}, \phi'_{cv}$ and their respective dilation rates. It was to this end that further simulations using smooth platens (with a range of interparticle friction angles) were run to supplement the one smooth platen simulation in the series investigating the effect of loading platen friction. The uniform deformation produced in these tests enabled good estimates of the cross-sectional areas (taking into account both volume change and axial strain) and thus a closer estimate of the (true) material strength and dilation properties to be made.

The approach adopted for analysing the results of the smooth platen simulations (in order to deduce a value for $\phi'_{cv}$) was to look for the proportion of a dilation rate which, when subtracted from the corresponding mobilised angle of shearing, would give the same value for both peak and at the end of test. Using the volume dilations and axial strains as indicated in Figure 6.15 the area-corrected angles of shear resistance at peak become 39.2°, 49.5° and 57.9° for interparticle friction angles of 17°, 26° and 35° respectively. The corresponding dilation angles with respect to axial strain are 9.0°, 16.2° and 23.4°. For the angles of shearing resistance at the end of test, the area-corrected values become 33.2°, 39.7° and 42.3° with corresponding dilation angles of 3.7°, 7.2° and 7.3°. By subtracting the full (100% ) dilation angle from the corresponding angle of shearing resistance it is found that in all cases $\phi'_{cv}$ at peak and at the end of the simulation were the same. Thus, for interparticle friction angles of 17°, 26° and 35° respectively, the deduced values of $\phi'_{cv}$ are 30°, 33°and 35° in which the pairs of values at a particular interparticle friction angle are each within 0.5° of the rounded means quoted.

These values are plotted in Figure 6.16 and show that

- the peak angle of shearing resistance $\phi'_{peak}$ increases at about the same rate as the interparticle friction angle

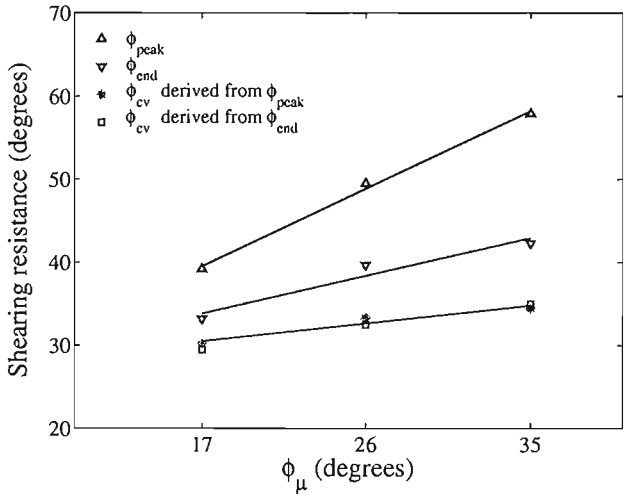


Figure 6.16: Material continuum properties: calculated angles of shearing resistance for $\phi'_{peak}$,$\phi'_{end}$ and $\phi'_{cv}$, based on true cross-sectional areas, as function of interparticle friction angle

- the calculated angle of shearing resistance at the critical state, $\phi'_{cv}$, increases at about one quarter the rate of that at peak.

For the simulations using smooth platen and different interparticle friction angle, although all three of them were carried out from the same initial porosity, the dilation increased with increasing interparticle friction angle, so that the (modest) increases in residual strength were achieved despite the resulting higher void ratios.

## 6.8 Summary

Numerical simulations of biaxial tests, in which soil samples were modelled using 10,000 particles comprising pairs of bonded spheres of shape factor 1.5 and interparticle friction angle $\phi_\mu = 26°$ (values reported in the literature as being close to that of many real sands for shape factor and of quartz for $\phi_\mu$), were carried out and the results showed close qualitative agreement

with laboratory test data for a medium subangular quartz sand presented by Alshibli and Sture (2000).

Over a range of initial sample porosities, biaxial test simulations using rough platens exhibited peak strength and dilation behaviour reasonably representative of sands in states varying from dense to loose, with the critical state being approached at the same rate and to the same extent at the end of the simulations. In addition, by assuming that the residual angle of shearing resistance at the critical state is given by the value at the end of test minus the dilation angle at the same stage, it was found that the same relation ($\phi'_{peak} = \phi'_{cv} + \psi$) held for all the simulations at peak except the densest, for which $\phi'_{peak} = \phi'_{cv} + 0.8\psi$. All simulations, however, fell on the same straight line on a graph of $\phi'_{peak} - \phi'_{cv}$ against relative density. Simulations over a range of interparticle friction angles using smooth loading platens and the densest packing, deformed very uniformly and made it possible to present stresses corrected for cross-sectional area both at peak and at residual points in the simulations. With these corrected values the relationship $\phi'_{peak} = \phi'_{cv} + \psi$ held over the full range investigated.

Modelling to investigate the effect of loading platen friction angle produced shear banding in the simulations with rough platen friction, the shear bands being the maximum width (consistent with the slope at which they occurred) that allowed them to pass through the sample from one side to the other without intersecting the loading platens. The implication is that, for these simulations, the formation of shear bands could have been a result of the boundary constraints rather than any material tendency to bifurcate, and that the results may not give an indication of any inherent material shear-band width. The simulation with rough ($\delta_{platen} = 26°$) end platens was also modelled using a continuum code which produced, by demonstrating arching

between the platens, a convincing explanation for the higher value and lower axial strain of the peak angle of shearing resistance in this case.

Simulations using the dense sand model to explore the effects of different particle properties gave, for the particle shape factor tests, a 25° rise in the peak angle of shearing resistance over the full shape factor range of 1 to 2 or, if the test on spherical particles is excluded ( being rather extreme), a rise of 19° for the reduced shape factor range of 1.3 to 2.0. The corresponding increases in the dilation angle at peak strength were 20° and 15° respectively. Interparticle friction was also found to have significant effects on the strength and dilation of the sample. For dense samples having a shape factor of 1.5, increasing the interparticle friction angle from 17° to 35° increased the peak angle of shearing resistance by 21°, with comparable changes in dilation rates. In simulations with smooth loading platens over the same range of interparticle friction angles, deformation was uniform allowing stress and strength values to be calculated based on actual cross-sectional areas. The results show a simple relationship between mobilized strength and dilation rate and indicate consistent values of residual shearing resistance which, for the range of interparticle friction investigated, increased at one quarter that of the peak angle of shearing resistance.

Particle rotations were monitored and showed the extent of structural disturbance, proving a useful tool for understanding and confirming deformation mechanisms. The formation and growth of shear bands in simulations using high loading platen friction angles, the increased amounts of rotation with particles having lower (i.e., more rounded) shape factors, and the rather greater proportion of large particle rotations when the intergranular friction angle was increased were all apparent.

# Chapter 7

# Summary and Conclusions

A three-dimensional discrete element method computer code PFC–3D has been used to investigate the mechanical response of cohesionless granular materials under general engineering stress conditions without grain damage and the presence of fluid. The investigation included:

1. Simulating granular materials using spheres; and understanding the limitations of such approaches.

2. Simulating granular material using non-spherical particles (pairs of bonded spheres); and to investigating the effects of particle shape.

3. Simulating laboratory tests in the direct shearbox and under biaxial compression; and investigating the effects of initial porosity and interparticle friction for assemblages of non-spherical particles on their mechanical response.

## 7.1 Simulation of granular material using spheres and the limitations of this approach

Uniform, 1 *mm* diameter spheres were used to simulate a granular material, and the effects of the initial porosity and interparticle friction of an assemblage of spheres on its shearing resistance and volumetric behaviour were investigated using numerical simulations of direct shearbox tests. A total of four different initial porosities ranging from 0.375 to 0.431, and total four different interparticle friction angles ranging from 5° to 45°, were examined. The conclusions are:

1. The peak shearing resistance increased with decreasing initial porosity and with increasing interparticle friction, but all the samples reached almost the same shearing resistance of 12° when the samples were approaching their critical states.

2. In simulations with different initial porosities, the very loose sample underwent a volumetric reduction at the beginning and then gradually dilated, while denser samples started to dilate from beginning of shearing.

3. The peak angle of shearing resistance increased by 13° and the volumetric dilation of the sample by a factor of almost 12 times when $\phi_\mu$ increased from 5° to 45°. This indicates that $\phi_\mu$ influences both the sample dilation and the angle of shearing resistance when the dilation begins.

4. The results from the numerical simulations and laboratory tests (Skinner, 1969) showed the same trends: the shearing resistance at the critical state ($\phi'_{cv}$) was independent of the initial porosity and interparticle

friction angle of spheres, which was different from a theoretical relation (Horne, 1969) between shearing resistance and interparticle friction. This is because the theory was based on a mechanism of pure sliding and without particle rotation, which predicts an increase of $\phi'_{cv}$ with interparticle friction angle.

5. A series of simulations in which the degree of rotation of the spheres was restrained showed that the rotation of particles during shearing made a major contribution to the shearing resistance of the assemblages, and both $\phi'_{peak}$ and $\phi'_{cv}$ increased as the degree of particle rotation was reduced.

6. For a given interparticle friction angle, the assemblage of spheres that were free to rotate had the lowest shearing resistance, and the spheres that were prevented from rotating had the highest. An non-interlocked granular material should have a shearing resistance between these two values because some degree of rotation will occur between granular particles during shearing.

7. For spheres that were free to rotate, a sample comprising a variety of particle sizes had a higher shearing resistance than a sample comprising uniform sized spheres, which suggests that the distribution of particle size might be an important factor in the shearing resistance of an assemblage of particles. This might be due to the lower porosity and more contact points of a sample comprising a variety of particle sizes than of an assemblage with uniform sized particles.

8. Numerical simulations using 1 $mm$ spheres showed a lower $\phi'_{cv}$ than laboratory tests using glass ballotini. This might result from assumptions made in the numerical model. In contrast to the numerical sample,

a real material will suffer from imperfection in uniformity of particle shape and size. Also the particle surface conditions are somewhat simplified in numerical simulations.

9. It was demonstrated that particle rotation is an overriding factor in determining the stress–strain behaviour of granular material. This highlights a major limitation of simulating materials such as sand using spheres: unrealistically low shearing resistance and volumetric dilation often result from excessive particle rotation.

## 7.2 Effect of particle shape

Non-spherical particles were simulated by bonding two spheres together and the overall shape of such a particle was characterised by a shape factor (R+r)/R; where R and r are the radii of the bigger and smaller spheres. A particle has a shape factor of 1 if it consists of one sphere, and shape factor of 2 if consists of two spheres of the same size.

1. The particle shape had a significant effect on the stress-strain behaviour of samples. Both peak shearing resistance and that at the end of shear almost doubled when the shape factor increased from 1 to 2. The dilation rate as well as the overall volumetric dilation of the samples also increased significantly when particles became less spherical.

2. The average of the particle rotation angles at the end of test dropped from 37° for the sample composed of spheres (shape factor 1) to 18° for the sample composed of particles with shape factor 2. This suggests that particle shape significantly affects the freedom of a particle to rotate.

3. The bulk friction angle of a sample comprising particles with a shape factor greater than 1.7 is higher than that of single spheres with rotation prevented. This indicates that the particle shape also contributes to the bulk friction angle in its own right, as a greater potential for interlocking will result from an increase in particle shape factor.

4. The formation of shear bands is dramatically affected by particle shape. Particle rotation in the sample comprising particles of shape factor 2 is concentrated within two bands which are clearly defined by adjacent dead zones. In a sample comprising spheres, particle rotation is much more evenly distributed and the dead zones are not apparent (i.e., Figure 6.12).

## 7.3 Effect of particle properties and boundary conditions

More numerical simulations (shearbox and biaxial test) were carried out using bonded particles to investigate the effects of the micro-properties of a granular material on its shear behaviour. For the simulations of shearbox tests, the shear strength and stress-strain behaviour were examined for different numbers of particles in the sample, three different interparticle friction values and four normal effective stresses. For the simulations of biaxial tests, the effect of initial packing density, interparticle friction angle and friction on the loading platen on the sample stress-strain behaviour and the formation of shear bands were investigated. The main conclusions are as follows.

1. The number of particles in the sample is important. The simulations of shearbox tests revealed that it affected most significantly the residual

bulk friction angle and the volumetric dilation of the sample. Both fell by about 24% when the number of particles was increased from 5000 to 50000, while the peak bulk friction angle decreased slightly by 4%. However, the changes in peak friction angle and volumetric dilation were less marked when the number of particles was more than 15000.

2. In both types of simulations, greater shearing resistance (both peak and at the end of shear) and volumetric dilation were observed when the interparticle friction angle was increased. In contrast to the behaviour of samples consisting of spheres, the value of $\phi'_{cv}$ increases with the value of $\phi_\mu$ and the results from samples consisting of bonded particles with shape factor 1.5 show a trend similar to the theoretical work of Horne (1969). Also a higher $\phi_\mu$ (35°) caused a substantially higher proportion of particles in the sample to rotate by more than 70° than a lower $\phi_\mu$ of 17°.

3. In the simulations of shearbox tests, an increase in the normal effective stress resulted in a decrease in both the peak and residual angles of shearing resistance, though the amount of decrease was in both cases considerably greater for the numerical model than for a real sand over the range investigated.

4. Over a range of initial sample porosities, biaxial test simulations using rough platens exhibited peak strength and dilation behaviour reasonably representative of sands in states varying from dense to loose, with the critical state being approached at the same rate and to the same extent at the end of each of the simulations. In addition, by assuming that the residual angle of shearing resistance at the critical state is given by the value at the end of simulation minus the dilation

angle at the end of simulation, it was found that the same relation ($\phi'_{peak} = \phi'_{cv} + \psi$) held for all the simulations at peak except the densest, for which ($\phi'_{peak} = \phi'_{cv} + 0.8\psi$). All simulations, however, fell on the same straight line on a graph of ($\phi'_{peak} - \phi'_{cv}$) against density index (Figure 6.9). With increasing initial porosity, shearbands in the sample become less pronounced and practically disappear in the loosest sample, in which the dead zones are not so clearly defined (by particle rotations) as in the denser samples.

5. Friction angle of 26° on the loading platens clearly restricted the movement of particles adjacent to them resulting in a non uniform distribution of stress. This leads to a higher peak shearing resistance and formation of dead zones. Simulations over a range of interparticle friction angles using smooth loading platens and the densest packing, deformed very uniformly and made it possible to present stresses corrected for cross-sectional area at both peak and residual points in the simulations. With these corrected values, the relationship ($\phi'_{peak} = \phi'_{cv} + \psi$) held over the full range investigated.

6. Particle rotations were monitored and clearly showed the extent of structural disturbance, proving a useful tool for understanding and confirming deformation mechanisms. The formation and growth of shear bands in simulations using high loading platen friction angles, the increased amounts of rotation with particles having lower (i.e., more rounded) shape factors, and the rather greater proportion of large particle rotations when the intergranular friction angle was increased were all very apparent.

## 7.4 Suggestions for future research

### 7.4.1 Limitations of the numerical simulations

Numerical simulation in general is a technique used to interpret natural processes and activities observed in real world, and also used to predict possible behaviour caused by processes and activities under given conditions. It usually requires the physical action of the problem to be understood well enough to choose suitable kinds of numerical methods which should adequately consider both the behaviour to be investigated and the physical structure to be modelled. Numerical simulations often suffer two basic limitations:

- Numerical methods rely on mathematical models based on certain assumptions to approximate reality. The assumptions, which often result from the lack of a precise understanding of physical action or from the need for mathematical simplicity, will inevitably introduce errors into the simulation results. The choice of simulated conditions which best fit the assumptions made in the models therefore become fundamentally important. In the DEM used in this study, for example, an individual particle is modelled as a rigid non-deformable sphere and interacts with other particles via deformable contact. This assumption is reasonable at low stresses. When stresses are high, considerable particle deformation may occur and the validity of this assumption then needs to be verified (e.g., the difference between particle deformation and contact deformation).

- Errors occur in numerical calculation. Even if the right mathematical model is chosen, compromises often have to be made because of insufficient computing power or limitations in computer precision.

It is important to realise that numerical simulation helps to understand reality, not to prove it.

### 7.4.2 Modelling the behaviour of granular material

In the simulations carried out in this study, the strength and dilation behaviour were investigated for changes in only a few particle properties at low stresses. The effect of particle deformation and damage, or the influence of fluid was not taken into consideration. This is not to say that these factors are not important; in fact, they represent the broader and more realistic conditions which can be found in many real engineering problems. However, they will introduce unnecessary complexities, therefore are omitted, in the present study of the effect of particle shape and size on the strength of assemblages.

The simulations using uniform sized 1 $mm$ spheres revealed that the shearing resistance at the critical state ($\phi'_{cv}$) was independent of the interparticle friction. Particle rotation is believed to be the reason. Future research will further investigate the behaviour of an assemblage comprising 1 $mm$ spheres

1. When the rotation of individual particles is restrained, particularly when all particles are only allowed to slide. Will the relationship between $\phi'_{cv}$ and $\phi_\mu$ in this extreme case match the theoretical prediction by Horne (1969)?

2. When the interparticle friction angle is very close to zero. Will the restraint on particle rotation make any difference?

It was found that samples consisting of different sized spheres showed higher shearing resistance than those comprising of 1 $mm$ spheres. It is

assumed that the higher density, and therefore the larger number of inter-particle contacts, resulting from the non-uniform size is the important factor. Future research could be aimed at

1. The effect of different particle size distributions on the shearing resistance of an assemblage of spheres.

2. Whether the similar effects can be found for non-spherical particles?

Particle shape dramatically affects particle rotation and the overall sample strength. However, the simulated non-spherical particles, formed by bonding two spheres together, represent a very simplified approximation far from real particles such as sand. It is possible to bond more particles together to form a more sophisticated and therefore more realistically shaped particle. Due to limitations in computing power, it might still be impractical to model a laboratory test using such particles. Nevertheless, such particles will enable further investigation into

1. How the particle size will affect particle behaviour?

2. The effects of particle deformation and crushing.

3. The effect of the constitutive rule for particle interaction.

Further understanding could be obtained by developing numerical simulations of the laboratory test, e.g., the standard triaxial test or shearbox test using smaller sample with correct sized particles.

# References

Alshibli, K. A. and Sture, S. (1999). "Sand shear band thickness measurement by digital imaging techniques." *Journal of Computing in Civil Engineering*, ASCE, 13(2), 103–109.

Alshibli, K. A. and Sture, S. (2000). "Shear band formation in plane strain experiments of sand." *Journal of Geotechnical and Geoenvironmental Engineering*, ASCE, 126(6), 495–503.

Arthur, J. R. F., Chua, K. S., and Dunstan, T. (1977). "Induced anisotropy in a sand." *Géotechnique*, London, 27(1), 13–30.

Arthur, J. R. F., Chua, K. S., Dunstan, T., and Rodriguez, J. I. (1980). "Principal stress rotation: A missing parameters." *Journal of the geotechnical engineering division*, ASCE, 106(GT4), 419–433.

Arthur, J. R. F., Dunstan, T., Al-Ani, Q. A. J. L., and Assadi, A. (1977). "Plastic deformation and failure in granular media." *Géotechnique*, London, 27(1), 53–74.

Arthur, J. R. F. and Phillips, A. B. (1975). "Homogeneous and layered sand in traxial compression." *Géotechnique*, London, 25(4), 799–815.

Barden, L. and McDermott, J. W. (1965). "Use of free ends in triaxial testing

of clays." *Journal of the soil mechanics and foundations division*, ASCE, 91(SM6), 1–23.

Bardet, J. P. and Proubet, J. (1991). "A numerical investigation of the structure of persistent shear bands in granular media." *Géotechnique*, London, 41(4), 599–613.

Bardet, J. P. and Proubet, J. (1992). "Shear-band analysis in idealized granular material." *Journal of engineering mechanics*, ASCE, 118(2), 397–415.

Bathurst, R. J. and Rothenburg, L. (1990). "Observations on stress-force-fabric relationships in idealized granular materials." *Mechanics of Materials*, 9(1), 65–80.

Bishop, A. W. (1954). "Correspondence on shear characteristics of a saturated silt, measured in triaxial compression." *Géotechnique*, London, 4(1), 43–45.

Bishop, A. W. (1966). "The strength of soils as engineering materials." *Géotechnique*, London, 16(2), 91–130.

Bishop, A. W. (1971). "Discussion of session one." *Stress-strain behaviour of soils: Proceedings of the Roscoe Memorial Symposium*, R. H. G. Parry, ed., G. T. FOULIS & CO LTD, Oxfordshire, 125–139.

Bishop, A. W. and Green, G. E. (1965). "The influence of end restraint on the compression strength of a cohesionless soil." *Géotechnique*, London, 15(3), 243–266.

Bolton, M. D. (1986). "The strength and dilatancy of sands." *Géotechnique*, London, 36(1), 65–78.

Bowden, F. P. and Tabor, D. (1950). *The friction and lubrication of solids. Part I.* Oxford University Press, London.

Bowden, F. P. and Tabor, D. (1964). *The friction and lubrication of solids. Part II.* Oxford University Press, London.

Bransby, P. L. (1971). "Disscussion of papers in session 2." *Stress-strain behaviour of soils: Proceedings of the Roscoe memorial symposium*, Oxfordshire. G. T. FOULIS & CO LTD, 255–258.

Butterfield, R., Harkness, R., and Andrawes, K. Z. (1970). "A stereophotogrammetric method for measuring displacement field." *Géotechnique*, London, 20(3), 308–314.

Cheng, Y. P., Nakata, Y., and Bolton, M. D. (2003). "Distinct element simulation of crushable soil." *Géotechnique, (under review).*

Cornforth, D. H. (1964). "Some experiments on the influence of strain conditions on the strength of sand." *Géotechnique*, London, 14(2), 143–167.

Cundall, P. A. (1971). "A computer model for simulating progressive large scale movements in blocky rock system." *Proceedings of the symposium of the International Society of Rock Mechanics*, Vol. 1. Paper Number: II-8, Nancy, France.

Cundall, P. A. (1989). "Numerical experiments on localization in frictional materials." *Ingenieur-Archiv*, 59(2), 148–159.

Cundall, P. A. and Hart, R. D. (1992). "Numerical modelling of discontinua." *Engineering computations*, 9, 101–113.

Cundall, P. A. and Strack, O. D. L. (1979). "A discrete numerical model for granular assemblies." *Géotechnique*, London, 29(1), 47–65.

Desrues, J., Chambon, R., Mokni, M., and Mazerolle, F. (1996). "Void ratio evolution inside shear bands in triaxial sand specimans studied by computed tomography." *Géotechnique*, London, 46(3), 529–546.

Desrues, J., Lanier, J., and Stutz, P. (1985). "Localization of the deformation in tests on sand sample." *Engineering Fracture Mechanics*, 21(4), 909–921.

Drescher, A. (1976). "An experimental investigation of flow rules for granular materials using optically sensitive glass particles." *Géotechnique*, London, 26(4), 591–601.

Finn, W. D., Wade, N. H., and Lee, K. L. (1967). "Volume changes in triaxial and plane strain tests." *Journal of the soil mechanics and foundations division*, ASCE, 93(SM6), 297–308.

Finno, R. J., Harris, W. W., Mooney, M. A., and Viggiani, G. (1996). "Strain localization and undrained steady state of sand." *Journal of geotechnical engineering*, ASCE, 122(6), 462–473.

Finno, R. J., Harris, W. W., Mooney, M. A., and Viggiani, G. (1997). "Shear bands in plane strain compression of loose sand." *Géotechnique*, London, 47(1), 149–165.

Frossard, E. (1979). "Effect of sand grain shape on interparticle friction: indirect measurements by Rowe's stress dilatancy theory." *Géotechnique*, London, 29(3), 341–350.

Frost, J. D. and Jang, D. J. (2000). "Evolution of sand microstructure during shear." *Journal of Geotechnical and Geoenvironmental Engineering*, ASCE, 126(2), 116–130.

Han, C. and Drescher, A. (1993). "Shear bands in biaxial tests on dry coarse sand." *Soils & Foundations*, Tokyo, 33(1), 118–132.

Han, C. and Vardoulakis, I. (1991). "Plane-strain compression experiments on water-saturated fine-grained sand." *Géotechnique*, London, 41(1), 49–78.

Harris, W. W., Viggiani, G., Mooney, M. A., and Finno, R. J. (1995). "Use of stereophotogrammetry to analyze the development of shear bands in sand." *Geotechnical testing journal*, ASTM, 18(4), 405–420.

Head, K. H. (1988). *Manual of Soil Laboratory Testing*, Vol. 2, 616–650. PENTECH PRESS, London : Plymouth.

Henkel, D. J. and Wade, N. H. (1966). "Plane strain tests on a saturated remolded clay." *Journal of the soil mechanics and foundations division*, ASCE, 92(SM6), 67–80.

Hettler, A. and Vardoulakis, I. (1984). "Behaviour of dry sand tested in a large triaxial apparatus." *Géotechnique*, London, 34(2), 183–198.

Horne, M. R. (1965). "The behaviour of an assembly of rotund,rigid cohesionless particles, Part I and II." *Proceedings of the Royal Society*, Vol. 286 of *A*, London. The Royal Society, 67–97.

Horne, M. R. (1969). "The behaviour of an assembly of rotund, rigid cohesionless particles, Part III." *Proceedings of the Royal Society*, Vol. 310 of *A*, London. The Royal Society, 21–34.

Ishibashi, I., C. Perry III, and Agarwal, T. K. (1994). "Experimental determinations of contact friction for spherical glass particles." *Soils & Foundations*, Tokyo, 34(4), 79–84.

Issa, J. A. and Nelson, R. B. (1992). "Numerical analysis of micromechanical behaviour of granular materials." *Engineering computations*, 9, 211–223.

Itasca Consulting Group Inc. (1997). *$PFC^{3D}$ User's manual, Version 1.1.* Minnesota, 55415, USA.

Itasca Consulting Group Inc. (1999). *3DEC User's manual, Version 2.0.* Minnesota, 55415, USA.

Iwashita, K. and Oda, M. (1998). "Rotational resistance at contacts in simulation of shear band development by DEM." *Journal of engineering mechanics division*, ASCE, 124(3), 285–292.

Jaeger, J. C. (1971). "Friction of rocks, and stability of rock slopes." *Géotechnique*, London, 21(2), 97–134.

Jensen, R. P., Bosscher, P. J., Plesha, M. E., and Edil, T. B. (1999). "DEM simulation of granular media-structure interface: effects of surface roughness and particle shape." *International Journal for Numerical and Analytical Methods in Geomechanics*, 23, 531–547.

Kirkpatrick, W. M. and Belshaw, D. J. (1968). "On the interpretation of the triaxial test." *Géotechnique*, London, 18(3), 336–350.

Koerner, R. M. (1970). "Effect of particle characteristics on soil strength." *Journal of the soil mechanics and foundations division*, ASCE, 96(SM4), 1221–1234.

Lee, I. K. (1966). "Stress-dilatancy performance of feldspar." *Journal of the soil mechanics and foundations division*, ASCE, 92(SM2), 79–103.

Lee, K. L. (1970). "Comparison of plane strain and triaxial tests on sand." *Journal of the soil mechanics and foundations division*, ASCE, 96(SM3), 901–923.

Lee, K. L. and Seed, H. B. (1964). "Discussion on 'Importance of free ends in triaxial testing'." *Journal of the soil mechanics and foundations division*, ASCE, 90(SM6), 173–175.

Lee, K. L. and Seed, H. B. (1967). "Drained strength characteristics of sands." *Journal of the soil mechanics and foundations division*, ASCE, 93(SM6), 117–141.

Lin, X. and Ng, T.-T. (1995). "Contact detection algorithms for three-dimensional ellipsoids in discrete element modeling." *International Journal for Numerical and Analytical Methods in Geomechanics*, 19, 653–659.

Lin, X. and Ng, T.-T. (1997). "A three-dimensional discrete element model using arrays of ellipsoids." *Géotechnique*, London, 47(2), 319–329.

McDowell, G. R. and Bolton, M. D. (1998). "On the micromechanics of crushable aggregates." *Géotechnique*, London, 48(5), 667–679.

McDowell, G. R. and Harireche (2002). "Discrete element modelling of soil particle fracture." *Géotechnique*, London, 52(2), 131–135.

Mitchell, J. K. (1993). *Fundamentals of soil behavior.* Wiley, New York.

Mühlhaus, H.-B. and Vardoulakis, I. (1987). "The thickness of shear bands in granular materials." *Géotechnique*, London, 37(3), 271–283.

Newland, P. L. and Allely, B. H. (1957). "Volume changes in drained triaxial tests on granular materials." *Géotechnique*, London, 7(1), 17–34.

Ng, T.-T. and Dobry, R. (1992). "A non-linear numerical model for soil mechanics." *International Journal for Numerical and Analytical Methods in Geomechanics*, 16, 247–263.

Ng, T.-T. and Dobry, R. (1994). "Numerical simulations of monotonic and cycled loading of granular soil." *Journal of Geotechnical Engineering*, ASCE, 120(2), 388–403.

Ni, Q., Powrie, W., Harkness, R., and Zhang, X. (2003). "Numerical modelling of biaxial shear tests on sands using a particulate approach." *Géotechnique, (under review).*

Ni, Q., Powrie, W., Zhang, X., and Harkness, R. (2000). "Effect of particle properties on soil behaviour: 3-D numerical modelling of shearbox tests." *Geotechnical Special Publication*, Vol. 96, Reston,VA. ASCE, 58–70.

Oda, M. (1977). "Co-ordination number and its application to shear strength of granular material." *Soils & Foundations*, Tokyo, 17(2), 29–42.

Oda, M. and Iwashita, K. (1999). *Mechanics of granular materials–An introduction.* A. A. Balkema, Rotterdam, Netherlands.

Oda, M. and Kazama, H. (1998). "Microstructure of shear bands and its relation to the mechanisms of dilatancy and failure of dense granular soils." *Géotechnique*, London, 48(4), 465–481.

Oda, M. and Konishi, J. (1974). "Microscopic deformation mechanism of granular material in simple shear." *Soils & Foundations*, Tokyo, 14(4), 25–38.

Oda, M., Konishi, J., and Nemar-Nasser, S. (1982). "Experimental microme-

chanical evaluation of strength of granular materials: effect of particle rolling." *Mechanics of Materials*, 1, 267–283.

Oda, M., Nemar-Nasser, S., and Konishi, J. (1985). "Stress-induced anisotropy in granular masses." *Soils & Foundations*, Tokyo, 25(3), 85–97.

Parikh, P. V. (1967). "The shearing behaviour of sand under axisymmetric loading," PhD thesis, Manchester University.

Powrie, W. (1997). *Soil Mechanics: Concepts and Application*, chapter 2. E & FN SPON, London.

Procter, D. C. and Barton, R. R. (1974). "Measurements of the angle of interparticle friction." *Géotechnique*, London, 24(4), 581–604.

Roscoe, K. H. (1970). "The influence of strains in soil mechanics." *Géotechnique*, London, 20(2), 129–170.

Roscoe, K. H. and Schofield, A. N. (1964). "Discussion of 'Stress-dilatancy, earth pressures, and slopes'." *Journal of the soil mechanics and foundations division*, ASCE, 90(SM1), 136–150.

Roscoe, K. H., Schofield, A. N., and Wroth, C. P. (1958). "On the yielding of soils." *Géotechnique*, London, 8(1), 22–53.

Rothenburg, L. and Bathurst, R. J. (1992). "Micromechanical features of granular assemblies with planar elliptical particles." *Géotechnique*, London, 42(1), 79–95.

Rowe, P. W. (1962). "The stress-dilatancy relation for static equilibrium of an assembly of particles in contact." *Proceedings of the Royal Society*, Vol. 269 of *A*, London. The Royal Society, 500–527.

Rowe, P. W. (1969). "The relation between the shear strength of sands in triaxial compression, plane strain and direct shear." *Géotechnique*, London, 19(1), 75–86.

Rowe, P. W. (1971). "Theoretical meaning and observed values of deformation parameters for soil." *Stress-strain behaviour of soils: Proceedings of the Roscoe Memorial Symposium*, R. H. G. Parry, ed., G. T. FOULIS & CO LTD, Oxfordshire, 143–194.

Rowe, P. W. and Barden, L. (1964). "Importance of free ends in triaxial testing." *Journal of the soil mechanics and foundations division*, ASCE, 90(SM1), 1–27.

Santamarina, C. and Cascate, G. (1998). "Effect of surface roughness on wave propagation parameters." *Géotechnique*, London, 48(1), 129–136.

Saussus, D. R. and Frost, D. (2000). "Simulating the membrane contact patterns of triaxial sand specimens." *International Journal for Numerical and Analytical Methods in Geomechanics*, 24, 931–946.

Scarpelli, G. and Wood, D. M. (1982). "Experimental observations of shear band patterns in direct shear tests." *Proceedings of IUTAM conference on defects and failure in granular media*, Rotterdam, Neth. A. A. Balkema, 473–484.

Schanz, T. and Vermeer, P. A. (1996). "Angles of friction and dilatancy of sand." *Géotechnique*, London, 46(1), 145–151.

Schofield, A. N. and Wroth, C. P. (1968). *Critical State Soil Mechanics.* McGraw-Hill, London.

Skinner, A. E. (1969). "A note on the influence of interparticle friction on the shearing strength of a random assembly of spherical particles." *Géotechnique*, London, 19(1), 150–157.

Stone, K. J. L. and Wood, D. M. (1992). "Effects of dilatancy and particle size observed in model tests on sand." *Soils & Foundations*, Tokyo, 32(4), 43–57.

Tatsuoka, F., Nakamura, S., Huang, C. C., and Tani, K. (1990). "Strength anisotropy and shear band direction in plane strain tests of sands." *Soils & Foundations*, Tokyo, 30(1), 35–54.

Thomas, P. A. and Bray, J. D. (1999). "Capturing nonspherical shape of granular media with disk clusters." *Journal of Geotechnical and Geoenvironmental Engineering*, ASCE, 125(3), 169–178.

Thornton, C. (2000). "Numerical simulations of deviatoric shear deformation of granular media." *Géotechnique*, London, 50(1), 43–53.

Ting, J. M., Corkum, B. T., Kauffman, C. R., and Greco, C. (1989). "Discrete numerical model for soil mechanics." *Journal of Geotechnical Engineering*, ASCE, 115(3), 379–398.

Ting, J. M., Khwaja, M., Meachum, L. R., and Rowell, J. D. (1993). "An ellipse-based discrete element model for granular materials." *International Journal for Numerical and Analytical Methods in Geomechanics*, 17, 603–623.

Ting, J. M., Meachum, L. R., and Rowell, J. D. (1995). "Effect of particle shape on the strength and deformation mechanisms of ellipse-shaped granular assemblages." *Engineering computations*, 12, 99–108.

Tombs, S. G. (1969). "Strength and deformation characteristics of rockfill," PhD thesis, University of London.

Tong, P. Y. L. (1970). "Plane strain deormation of sands," PhD thesis, University of Manchester.

Trent, B. C. and Margolin, L. G. (1992). "A numerical laboratory for granular solids." *Engineering computations*, 9, 191–197.

Vardoulakis, I. (1980). "Shear band inclination and shear modulus of sand in biaxial tests." *International Journal for Numerical and Analytical Methods in Geomechanics*, 4, 103–119.

Vardoulakis, I. and Goldscheider, M. (1981). "Biaxial apparatus for testing shear bands in soils." *Proceedings of the International Conference on Soil Mechanics and Foundation Engineering*, Vol. 1, Rotterdam, Neth. A. A. Balkema, 819–824.

Vardoulakis, I., Goldscheider, M., and Gudehus, G. (1978). "Formation of shear band in sand bodies as a bifurcation problem." *International Journal for Numerical and Analytical Methods in Geomechanics*, 2, 99–128.

Vardoulakis, I. and Graf, B. (1982). "Imperfection sensitivity of the biaxial test on sand." *Proceedings of IUTAM conference on defects and failure in granular media*, Rotterdam, Neth. A. A. Balkema, 485–491.

Vardoulakis, I. and Graf, B. (1985). "Calibration of constitutive models for granular materials using data from biaxial experiments." *Géotechnique*, London, 35(3), 299–317.

Vermeer, P. A. (1990). "The orientation of shear bands in biaial tests." *Géotechnique*, London, 40(2), 223–236.

Wroth, C. P. (1958). "Soil behaviour during shear." *Engineering*, Sept, 409–413.

Wroth, C. P. and Bassett, R. H. (1965). "A stress-strain relationship for the shearing behaviour of a sand." *Géotechnique*, London, 15(1), 32–56.